An x-ray computed tomography polymer gel dosimetry system for complex radiation therapy treatment verification

by

Holly Anne Johnston
B.Sc., University of British Columbia, 2005
M.Sc., University of Victoria, 2008

A Dissertation Submitted in Partial Fulfillment of the
Requirements for the Degree of

DOCTOR OF PHILOSOPHY

in the Department of Physics and Astronomy

An x-ray computed tomography polymer gel dosimetry system for complex radiation therapy treatment verification

by

Holly Anne Johnston
B.Sc., University of British Columbia, 2005
M.Sc., University of Victoria, 2008

Supervisory Committee

Dr. M. Hilts, Co-Supervisor
(Department of Physics and Astronomy)

Dr. A. Jirasek, Co-Supervisor
(Department of Physics and Astronomy)

Dr. D. Wells, Member
(Department of Physics and Astronomy)

Dr. A. Albu, Outside Member
(Department of Electrical and Computer Engineering)

Supervisory Committee

Dr. M. Hilts, Co-Supervisor
(Department of Physics and Astronomy)

Dr. A. Jirasek, Co-Supervisor
(Department of Physics and Astronomy)

Dr. D. Wells, Member
(Department of Physics and Astronomy)

Dr. A. Albu, Outside Member
(Department of Electrical and Computer Engineering)

ABSTRACT

X-ray computed tomography (CT) polymer gel dosimetry (PGD) is an attractive tool for three-dimensional (3D) radiation therapy (RT) treatment verification due to the availability of CT scanners in RT clinics. Nevertheless, wide-spread use of the technique has been hindered by low signal-to-noise CT images largely resulting from gel formulations with low radiation sensitivity. However, a new gel recipe with enhanced dose sensitivity was recently introduced that shows great promise for use with CT readout. This dissertation describes development of an CT PGD system for 3D verification of RT treatments using the new gel formulation. The work is divided into three studies: gel characterization, commissioning of a multislice CT scanner and investigation of a dose rate dependence observed during gel characterization.

The first component of this work examines the dosimetric properties of the new gel formulation. The response of the gel is found to be stable between 15 - 36 hours post-irradiation and excellent batch reproducibility is seen for doses between 0 - 28 Gy. A dose rate dependence is found for gels irradiated between 100 - 600 MU/min,

indicating machine dose rate must be consistent for calibration and test irradiations to avoid dosimetric error. An example clinical application is also presented using an IMRT treatment verification that demonstrates the potential of the system for use in modern RT.

The second component of this work focuses on commissioning a multislice CT scanner for CT PGD. A new slice-by-slice background subtraction technique is introduced to account for the anode heel effect. Additional investigations show recommendations for optimizing image quality in CT PGD using a single slice machine also apply to multislice scanners. In addition, the consistency of CT numbers across the multislice detector array is found to be excellent for all slice thicknesses. Further work is performed to assess the tube load characteristics of the scanner and develop a scanning protocol for imaging large gel volumes. Finally, images acquired throughout the volume of an unirradiated active gel show variations in CT data across each image on the order of 7 HU. However, these variations are not expected to greatly influence gel measurements as they are consistent throughout the gel volume.

The third component of this work examines the dose rate dependence found during gel characterization. Studies using gel vials and 1 L cylinders indicate the response of the gel does not depend on changes in mean dose rate on the order of seconds to minutes. However, the machine dose rate remains, indicating variations in dose rate on the order of milliseconds influence the response of the gel. An attempt is made to mitigate the effect by increasing the concentration of antioxidant in the gel system but results in reduced overall response. Further work is performed to determine if self-crosslinking of one of the gel components contributes to the observed machine dose rate dependence.

In summary, this dissertation has significantly advanced the field of gel dosimetry by providing a prototype CT PGD system with enhanced dose resolution for complex RT treatment verification.

Contents

List of Tables

List of Figures

List of Abbreviations

2D Two-dimensional

3DCRT Three-dimensional Conformal Radiation Therapy

3D Three-dimensional

4DCT Four-dimensional Computed Tomography

AAm Acrylamide

AM Adaptive Mean

AM Remnant Artifact Removal

BIS N,N'-methylenebisacrylamide

CMDR Constant Mean Dose Rate

CT X-ray Computed Tomography

DAQ Data Acquisition System

DNA Deoxyribonucleic Acid

DVH Dose Volume Histogram

EPID Electronic Portal Imaging Device

FOV Field of View

H Housfield Unit

IGRT Image Guided Radiation Therapy

IMAT Intensity Modulated Arc Therapy

IMRT Intensity Modulated Radiation Therapy

KERMA Kinetic Energy Released in the Medium

LINAC Linear Accelerator

MLC Multileaf Collimator

MOSFET Metal Oxide Silicon Field Effect Transistor

MRI Magnetic Resonance Imaging

MV Megavoltage

NIPAM N-isopropylacrylamide

NMR Nuclear Magnetic Resonance

OptCT Optical Computed Tomography

OSL Optically Stimulated Luminescence

PAG Polyacrylamide Gel

PET Positron Emission Tomography

PGD Polymer Gel Dosimetry

pps Pulses Per Second

QA Quality Assurance

ROI Region of Interest

RT Radiation Therapy

SBRT Stereotactic Body Radiation Therapy

SI International System of Units

SPECT Single Photon Emission Tomography

SRS Stereotactic Radiosurgery

SSD Source to Surface Distance

THPC Tetrakis (Hydroxymethyl) Phosphonium Chloride

TLD Thermoluminescent Detector

TMR Tissue Maximum Ratio

TPS Treatment Planning System

US Ultrasound

VMAT Volumetric Modulated Arc Therapy

VMDR-Off Variable Mean Dose Rate: Beam-Off Time Changes

VMDR-On Variable Mean Dose Rate: Beam-On Time Changes

Chapter 1

Introduction

It is estimated that over 500 people are diagnosed with cancer and 200 people die of cancer in Canada every day [1]. Of those who develop the disease, more than one half receive radiation therapy (RT) during the management of their illness [2–5]. Many of these patients benefit from increased life expectancy and improved quality of life, but most also experience at least some negative side-effects associated with radiation damage to healthy tissues [4]. As a result, much of the recent work to improve the accuracy and precision of RT has focused on incorporating highly advanced technology into the treatment process. While new technology can improve treatment outcome by providing three-dimensional (3D) dose distributions tailored to match the disease site, it also has the potential to introduce new and unexpected treatment errors [6]. For this reason, 3D dose verification tools are a critical component of any modern RT program. However, development of these tools has lagged behind clinical implementation of complex RT treatments, posing a significant risk to patient safety and quality of care. A promising solution to this problem is offered by polymer gel dosimetry (PGD). Gel dosimeters are radiosensitive hydrogels that record absorbed dose in 3D, with dose information quickly obtained using x-ray computed tomography (CT) imaging. The goal of this dissertation is to develop an CT polymer gel dosimetry (PGD) system for modern RT dose verification.

This chapter presents an overview of modern RT, beginning with a summary of the treatment process, description of modern treatment techniques and a discussion of treatment errors in section 1.1. The basic principles of radiation dosimetry are provided in section 1.2, followed by a summary of the dose verification tools currently available in modern RT programs in section 1.3. Section 1.4 provides an overview of the scope of this work.

1.1 Modern Radiation Therapy

Upon exposure to ionizing radiation, damage to deoxyribonucleic acid (DNA) can lead to mutation, carcinogenesis and ultimately cell death [7]. For this reason, the goal of RT is to deliver a prescribed dose of radiation to a well-defined disease volume while minimizing the dose to surrounding healthy tissues. Modern RT is continually evolving to better meet this goal by incorporating new technology into the treatment process and implementing new treatment techniques. This section provides an overview of modern RT, including a summary of the procedures used to plan and deliver a typical course of radiation, a description of new technologically advanced treatment techniques and a discussion of treatment errors.

1.1.1 Overview of the Treatment Process

Modern RT is a multi-step process that can be broadly summarized as consisting of simulation, treatment planning and treatment delivery. Figure 1.1 provides a schematic diagram illustrating the overall workflow associated with a typical RT treatment. Each stage of the treatment process is described in detail below.

Simulation

Simulation provides CT images of patient anatomy in 3D that are used to formulate a treatment plan without the patient present. Several other imaging modalities may also be used as a compliment to CT to aid in organ definition, including magnetic resonance imaging (MRI), ultrasound (US), positron emission tomography (PET), and single photon emission tomography (SPECT) [8, 9].

A modern CT simulator, illustrated in figure 1.2, typically includes a laser localization system, CT scanner and computer graphics station [10]. The laser localization system consists of three lasers that define the simulator room coordinate system, which is calibrated to match the treatment room coordinate system. At the beginning of simulation, patients are positioned on the simulator couch and radiopaque markers are affixed to where the lasers intersect their skin. The markers are visible on CT images and define patient position at simulation and during treatment planning. When imaging is complete, the markers are replaced with permanent tattoos that are used to position the patient at treatment delivery.

Following patient set-up, images are acquired using the CT scanner. A detailed

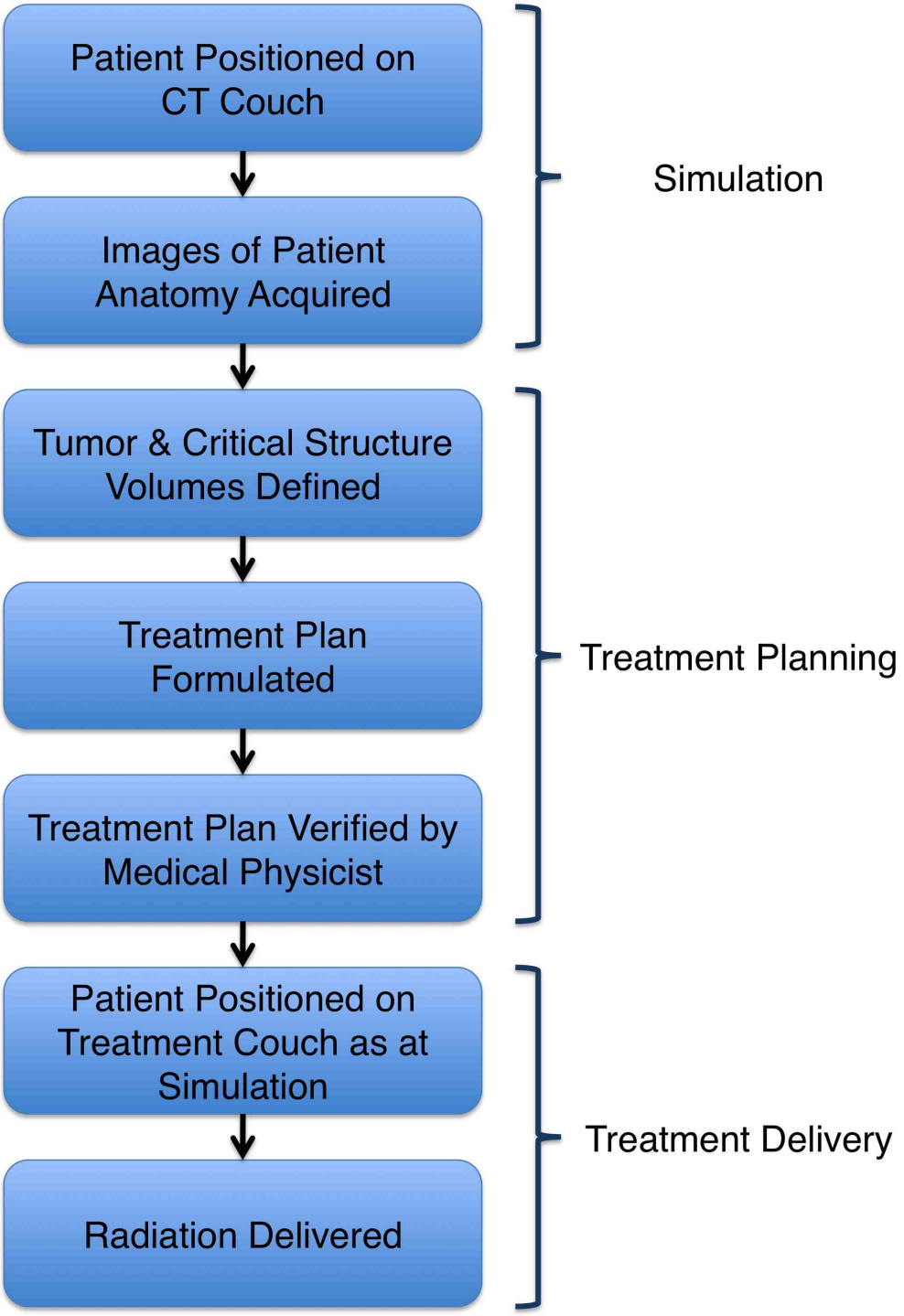

Figure 1.1: The workflow for a typical modern RT treatment, broadly consisting of simulation, treatment planning and treatment delivery.

overview of CT imaging is provided in chapter 2. Briefly, a typical modern CT scanner consists of a hollow circular gantry that houses an x-ray tube situated opposite an arc of x-ray detectors [8]. As scanning proceeds, the couch moves the patient into the gantry and the x-ray tube rotates 360° around the patient, emitting a continuous fan-beam of x-rays. As x-rays travel through the patient, the intensity of the incident and transmitted beams are measured by the detectors and sent to the computer graphics station for image processing. The resulting series of contiguous x-ray images, called "slices", illustrate patient anatomy in the transverse body plane (dividing the body into upper and lower regions) and provide 3D information about patient anatomy.

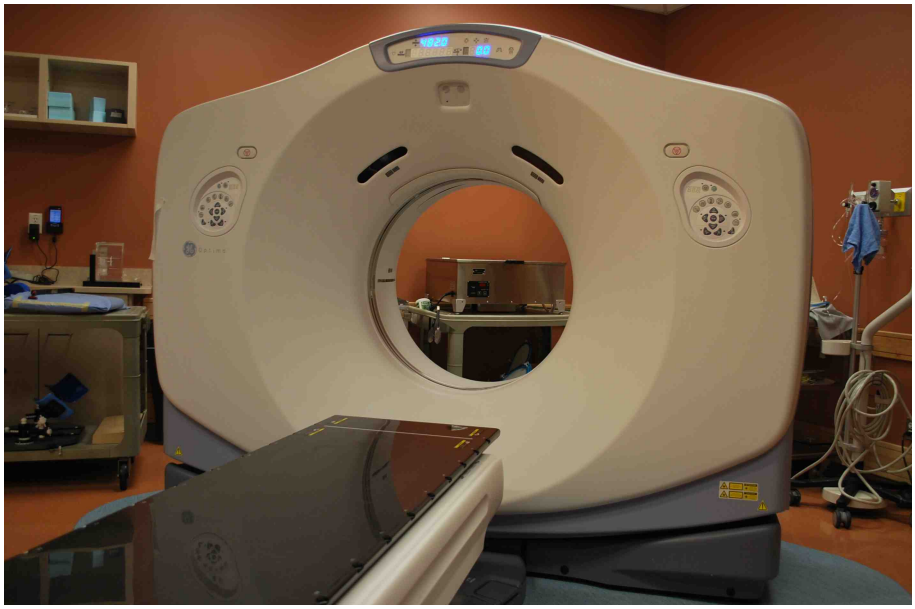

Figure 1.2: A modern CT simulator used to acquire images of anatomy in 3D for RT treatment planning. Lazers mounted on the simulator room walls to the left and right of the scanner and on the ceiling (not shown) are used for patient positioning.

Treatment Planning

Following simulation, a RT treatment plan is formulated to define how the prescribed dose of radiation will be delivered. It is developed by the radiation therapy team using sophisticated software called a treatment planning system (TPS). Modern TPSs compute the radiation dose distribution within a patient in 3D using images acquired at simulation and a complex dose calculation algorithm. Figure 1.3 shows an example of a modern RT treatment plan designed to treat head and neck cancer.

Treatment planning begins by importing CT simulation images into the TPS. Additional imaging studies conducted using MRI, PET, US, or SPECT may also be imported and registered to CT images to provide additional patient information [9]. This is followed by examination of the images by a radiation oncologist, who determines the location and extent of the disease and contours the radiation target and normal tissue volumes on each image slice. The radiation oncologist then prescribes the radiation dose required to treat the disease and also places limits on the dose that can be received by the surrounding normal tissues.

At this stage, a radiation therapist or medical physicist uses the TPS to design a radiation dose distribution that achieves, as closely as possible, the prescribed radiation doses within the patient. Several treatment parameters are adjusted, such as the number and intensity of radiation beams or the distribution of radioactive sources, until the planner is satisfied that the treatment plan provides the best possible configuration to achieve the aim of therapy. The TPS then determines the amount of radiation to be delivered by the therapy equipment to achieve the distribution. For external beam therapies delivered using a medical linear accelerator (LINAC), the amount of radiation output by the machine is measured in monitor units (MUs), where 1 MU = 1 cGy in a water phantom under LINAC calibration conditions.

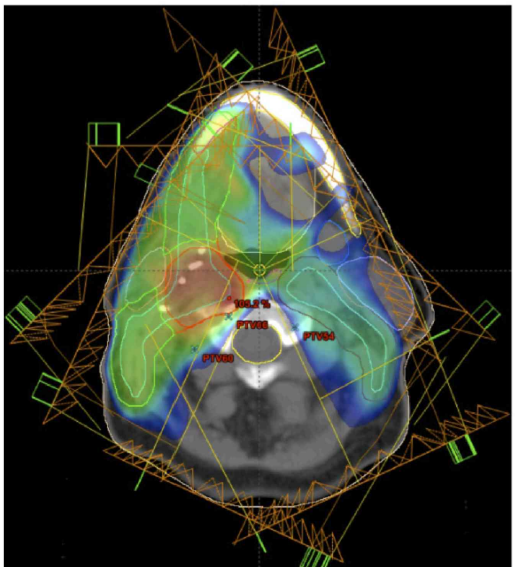

Figure 1.3: A modern RT treatment plan for a head and neck cancer patient.

Following design and optimization, the treatment plan is verified by a medical physicist, who performs an independent check that the MUs required to deliver the

treatment dose are correct and that the resulting dose distribution can be accurately delivered by the treatment equipment. The plan is then sent electronically to the treatment unit for delivery to the patient.

Treatment Delivery

Most modern RT is delivered using external radiation beams generated by a LINAC. A typical LINAC treatment room, illustrated in figure 1.4, consists of a laser localization system, treatment couch and LINAC housed in a rotating gantry. Similar to CT room laser localization, the treatment room lasers define the treatment room coordinate system. At each treatment session, patients are positioned on the LINAC couch as they were at simulation by aligning their tattoos with the treatment room lasers, and radiation is delivered.

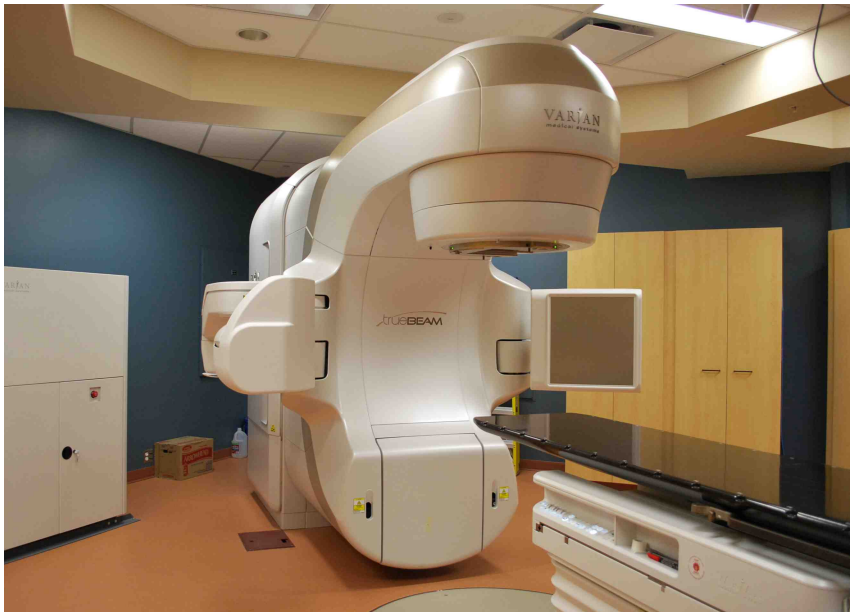

Figure 1.4: A LINAC in modern RT used to deliver external beam therapies. Similar to the CT simulator, lazers mounted on the treatment room walls to the left and right of the LINAC and on the ceiling (not visible in figure) are used for patient positioning at each day of treatment.

A detailed overview of LINAC operation is provided in chapter 4. In brief, the LINAC produces radiation by accelerating electrons to high-speeds in an accelerating microwave cavity. The electrons can themselves be used to form the treatment beam but are more commonly made to strike a tungsten target to produce megavoltage (MV) x-rays through bremsstrahlung interactions [9]. The shape and intensity of

the x-ray beam are commonly adjusted using square collimating jaws and a multileaf collimator (MLC). Figure 1.5 shows a modern MLC, composed of a large number of computer-controlled, collimating leaves that are typically 2.5 - 5.0 mm wide when projected at isocentre and can be moved independently of one another to produce a beam of any shape and intensity. The incorporation of the MLC into modern LINACs has allowed dramatic improvements in dose conformity and the development of several complex treatment techniques.

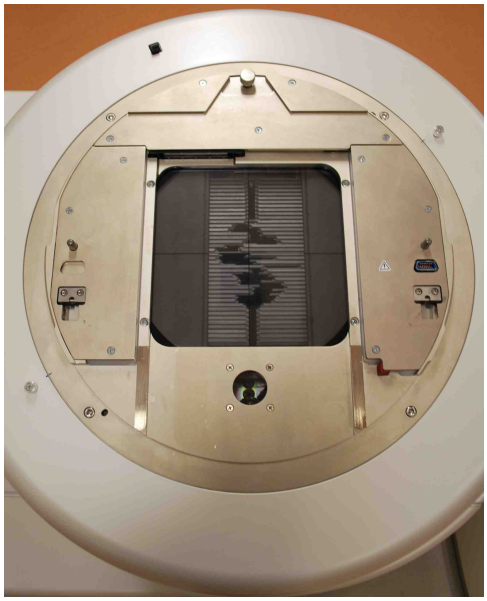

Figure 1.5: The MLC inside the LINAC treatment head used to shape the radiation beam to precisely match the radiation target. The leaves of this particular MLC model are 5.0 mm when projected at isocentre.

1.1.2 Modern Treatment Techniques

In modern RT, the LINAC administers radiation using a variety of treatment delivery techniques. Using 3D conformal RT (3DCRT), the prescribed radiation dose is divided into equal fractions that are delivered daily over the course of several weeks. At each day of treatment, multiple radiation beams are shaped using the MLC to match the contours of the radiation target and directed at the disease from different angles. This produces a 3D dose distribution that conforms as closely as possible to the shape of the treatment site, significantly sparing the surrounding normal tissues of high radiation doses [9].

For disease sites that surround or lie adjacent to critical normal structures, such as the spinal cord or lung, a more complex treatment technique called intensity modulated RT (IMRT) can be used to achieve the aim of therapy [11]. This type of treatment is similar to 3DCRT in that multiple radiation beams are directed at the target volume from different angles at each treatment session. However, for IMRT, the MLC not only shapes the field aperture, but is also used to modulate the intensity of each field as it is being delivered. In addition, advanced forms of IMRT called intensity modulated arc therapy (IMAT) [12] and volumetric modulated arc therapy (VMAT) [13], can be used to deliver an intensity-modulated treatment beam that rotates around the patient while radiation is being delivered. Each intensity modulated treatment technique produces highly conformal dose distributions with steep dose gradients between the disease site and nearby healthy tissues. This allows higher doses to be delivered to the radiation target than can be achieved using 3DCRT [14].

High radiation doses are also delivered using specialized RT methods known as stereotactic radiosurgery (SRS) and stereotactic body RT (SBRT). These techniques are specifically designed to treat exceptionally small lesions or those in close proximity to vital critical organs [9, 10]. Unlike the therapies described above, SRS and SRBT deliver the entire prescription dose in either a single treatment fraction or a small number of high dose fractions (typically no more than 5 sessions). For this reason, great care is taken to ensure the dose distribution is delivered as accurately as possible using rigorous patient immobilization throughout the RT process. Treatments typically consist of multiple, narrow beams that are delivered from several different angles and may or may not include MLC modulation. Similar to IMRT, IMAT and VMAT, this produces steep dose gradients between the target and normal tissue volumes, providing exceptional 3D conformity in the resulting dose distribution.

In conjunction with the above techniques, image guidance can be employed if the disease site is mobile within the body. For example, the prostate gland can move by up to 2 cm in one day due to filling and voiding of the nearby bladder and rectum [15]. For these treatments, classified as image guided RT (IGRT), images of the disease site are acquired at treatment planning and at each day of treatment delivery. The position of the radiation target is then determined from each image set and any displacement of the treatment volume from the time of treatment planning is corrected by shifting the patient before radiation is delivered.

In addition to external beam therapies, radiation can be administered using radioisotopes. This type of treatment is called brachytherapy and has become a routine

modern RT procedure due to its inherently conformal nature. It is typically used for well-defined disease volumes, such as the prostate gland or cervix, that can be accessed directly or through image-guidance. Brachytherapy treatments are classified based on the rate at which the radioactive source delivers dose [8]. High dose rate treatments use radioactive sources that deliver the prescribed dose within minutes for each treatment session and are temporarily inserted into the patient for a predetermined dwell-time. Low dose rate brachytherapy uses sources that deliver dose over a period of days to weeks and is typically administered as permanent seed implants [9].

1.1.3 Treatment Errors

Modern RT programs include rigorous quality assurance protocols to ensure patients receive safe and effect treatments. However, despite these efforts, errors can occur at any stage of the RT process. Many errors are considered minor and result in little or no injury to the patient [6], while others are catastrophic and lead to serious patient trauma [16] and even death.

There are many potential sources of error associated with any RT treatment. Some errors result from inadequate consideration of machines or software, such as incorrect calibration of a treatment beam or insufficient commissioning of the TPS [17, 18]. These errors typically affect large patient populations [19]. Many other errors are specific to each patient and can include misidentification of the disease volume, formulation of an unsatisfactory treatment plan or inadequate treatment documentation [17–21].

In addition to the errors already mentioned, advanced technologies common in modern RT can introduce new and unforeseen ways for treatment errors to occur [22]. This is of particular concern for treatments that deliver steep dose gradients between the target and normal tissues, as these distributions involve highly-technical planning and delivery procedures. For example, in IMRT treatments, failure to download the correct MLC leaf motions to the treatment unit can cause severe inaccuracies in delivered dose that may be harmful to the patient [17]. In addition, highly-conformal dose distributions can increase the probability of a geometric miss of the disease site [17, 18]. This can occur even if IGRT is used to track the radiation target due to errors associated with imaging devices [23]. Target localization is also critical in SRS and SBRT, as high-doses of radiation are delivered in very few treatment fractions [17]. In addition, uncertainties associated with radioactive sources and their physical

implantation pose several potential errors for brachytherapy treatments [24]. Clearly, in light of the many errors that can occur when delivering a modern RT treatment, it is necessary to verify the prescribed dose will be accurately and safely administered using dose measurement tools that can fully assess complex dose distributions.

1.2 Radiation Dosimetry

Radiation dosimetry is the measurement of absorbed dose in matter resulting from exposure to ionizing radiation, including electrons, x-ray and γ-ray photons, heavy charged particles and neutrons [25]. This section will consider only dosimetry of electrons and x-ray and γ-ray photons. In this regard, a brief overview of the basic principles of dosimetry is provided below, including a summary of the interactions of radiation with matter, radiation quantities and units and the characteristics of an ideal dosimeter.

1.2.1 Interactions of Radiation with Matter

The chain of events leading to energy deposition in a medium by radiation is different for electrons and photons. As electrons travel through a material, they produce a track along which energy is deposited through ionization, excitation and bremsstrahlung interactions. Photons, on the other hand, require a two-step process for dose deposition [25]. As a first step, the photon transfers energy to an atom in the material initiating the release of electrons in the medium through photoelectric absorption, Compton scattering or pair production (described below). Following the initial photon event, energy is transferred to the medium through excitation and ionization by the released particles [9, 26].

Ionization occurs when an incident electron collides with an atomic electron and transfers enough of its energy to remove the electron from the atom. Occasionally, the ejected electron receives sufficient energy to produce a secondary track of its own in the material and is then referred to as a δ-ray. However, if the energy transferred from the incident electron is insufficient to eject an electron from the atom, it may instead raise the atomic electron to a higher energy shell. This process is termed excitation [9, 26]. In addition to excitation and ionization, if the incident electron passes close to the nucleus of the atom, the Coulomb force of attraction between the two particles may cause deflection and deceleration of the electron from its original

path. The energy lost by the electron during its change of course is emitted by the atom as bremsstrahlung (i.e. braking) radiation, consisting of x-ray photons that can have any energy up to the initial energy of the incident electron [9]. Following their creation, bremsstrahlung photons continue to deposit energy in the medium through photoelectric absorption, Compton scattering or pair production.

The photoelectric effect, shown in figure 1.6, is a phenomenon in which a photon is completely absorbed by an atom. In this interaction, a photon (γ) collides with an atomic electron in one of the inner K, L, M, or N shells. The photon transfers its entire energy to the electron, freeing it from the atom. The ejected particle (e^-), known as a photoelectron, emerges from the atom creating a vacancy in one of the inner shells and leaving the atom in an excited state. The vacancy is then filled by an electron from a higher energy shell, followed by the release of excess energy through characteristic x-rays or Auger electrons, returning the atom to the ground state. The probability of photoelectric absorption depends on the energy (E) of the incident photons and the atomic number (Z) of the absorbing material as $\frac{Z^3}{E^3}$. It is the predominant interaction in soft tissue for photons with energies up to 50 keV and is also a significant process for photons with energies between 60 - 90 keV [9, 26].

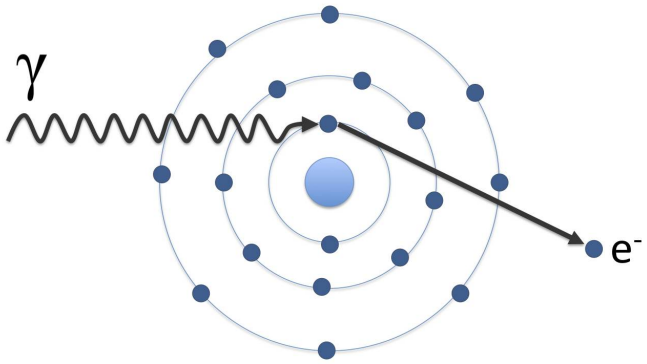

Figure 1.6: The photoelectric effect: an incident photon (γ) is absorbed by an inner-bound atomic electron, causing ejection of a photoelectron (e^-).

Compton scattering involves the interaction of a photon with an outer atomic electron considered to be "free", as the binding energy of the electron is much less than that of the incident photon. In this process, illustrated in figure 1.7, a photon collides with a free electron, transferring some of its energy to the electron and freeing it from the atom. The resulting Compton electron leaves the atom at angle θ, while the incident photon is scattered at angle ϕ. The probability of a Compton collision

is nearly independent of the atomic number of the scattering medium but depends on the energy of the incident photon as $\frac{1}{E}$. It becomes important at photons energies between 60 - 90 keV and is the only interaction that occurs for photons with energies between 200 keV - 2 MeV [9, 26].

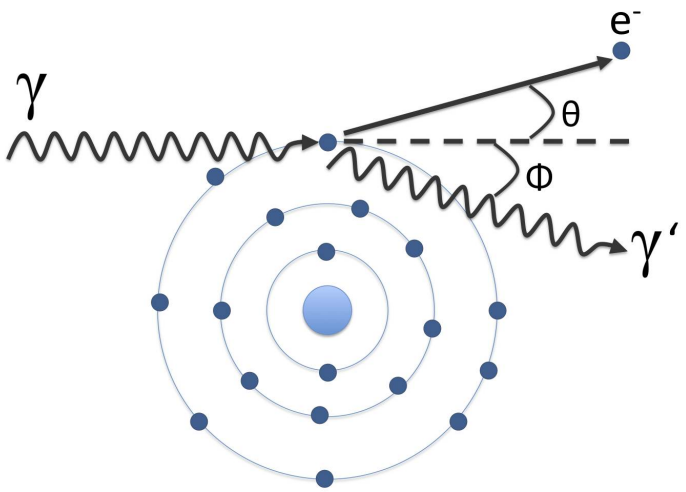

Figure 1.7: Compton scattering: an incident photon (γ) collides with an outer atomic electron and is scattered from the atom ($\gamma^{'}$) at angle ϕ. The electron emerges from the atom at angle θ.

In addition to the photoelectric effect and Compton scattering, pair production can occur for photons that pass close to the atomic nucleus. In this process, illustrated in figure 1.8, an incident photon interacts with the strong electromagnetic field of the atomic nucleus and is absorbed by the atom. The energy of the photon is then converted into an electron-positron pair. Since both the electron and positron have a rest mass of 0.511 MeV, the incident photon must have an energy $\geq$ 1.02 MeV to produce the two particles. Any additional photon energy is shared between the electron and positron (e^{+}) as kinetic energy. One particle may acquire nearly all the kinetic energy with the other receiving almost none, the two particles may share the energy equally or the kinetic energy may have any distribution between these extremes. The positron will then quickly annihilate with a free electron, producing two 0.511 MeV photons ejected at 180° degrees from one another. The probability of pair production depends on the atomic number of the absorbing material as Z, but only occurs for photons with energy $\geq$ 1.02 MeV and becomes rapidly more probable above this energy threshold [9, 26].

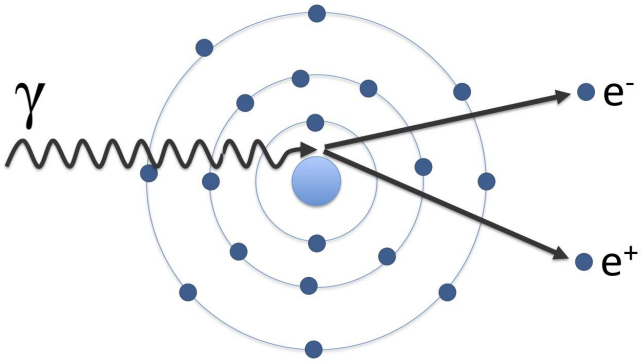

Figure 1.8: Pair production: an incident photon is absorbed by the nucleus of the atom, resulting in ejection of an electron-positron pair.

1.2.2 Radiation Quantities and Units

There are many quantities and units used to describe radiation, however, the quantity absorbed dose is the most important in RT. Absorbed dose is a measure of the energy deposited in a material by electrons and photons. The formal definition of absorbed dose, D, is given in equation 1.1, where $d\overline{E}_{ab}$ is the energy absorbed in a material of mass dm. Absorbed dose is measured in gray (Gy) in the International System of Units (SI), where 1 Gy = 1 J/kg [9, 26].

$$D = \frac{d\overline{E}_{ab}}{dm} \tag{1.1}$$

In addition to absorbed dose, the kinetic energy released in the medium (KERMA) is used to quantify the energy transferred from photons to electrons in the two-step process of photon dose deposition described in section 1.2.1. The KERMA, K, is given by equation 1.2, where $d\overline{E}_{tr}$ is the energy transferred from photons to electrons in mass dm.

$$K = \frac{d\overline{E}_{tr}}{dm} \tag{1.2}$$

Similar to absorbed dose, the SI unit for KERMA is the Gy. While KERMA represents the total energy transferred from photons to electrons through photon interactions, not all of the transferred energy is deposited in the medium, as some bremsstrahlung photons may leave the material without interacting [9, 26].

1.2.3 Characteristics of an Ideal Dosimeter

An ideal radiation dosimeter will possess several desirable characteristics, including a stable, reproducible response, invariance to changes in environmental and operating conditions, sufficient resolution for the intended application, tissue equivalence, dose integration and reusability. Many characteristics affect the overall accuracy and precision of dose measurements and must be thoroughly investigated before the dosimeter can be used in a RT clinic. Other characteristics are desired qualities that serve to increase the ease of use of the dosimeter.

The ability of a dosimeter to provide a stable response will influence the accuracy of dose measurements. Readings should be consistent over long time periods, or at least over a reasonable time-frame (e.g. minutes to hours), to ensure systematic variations in response are not observed before the necessary data are obtained. Sim-

ilarly, the dosimeter must be capable of maintaining the spatial integrity of a dose distribution for a sufficient window of time. Dose measurements should also be reproducible within experimental uncertainty when readings are repeated under identical conditions as this will determine the precision of the dosimeter.

Sensitivities to environmental and operating conditions will also impact the quality of dose readings. Each dose measurement should remain constant in response to variations in temperature, pressure and humidity. This will ensure reproducibly readings that represent the true value of the quantity being measured. Likewise, changes in radiation energy, angle of incidence and dose rate should not influence the response of the dosimeter, or at the very least, a suitable range of operating conditions must be established that provide accurate and reproducible measures of absorbed dose.

The dosimeter must also be capable of producing measurements with sufficient spatial and dosimetric resolution. Spatial resolution is determined by how finely dose measurements can be made in space, while dosimetric resolution depends on the ability of the dosimeter to distinguish different doses. For new treatment techniques that involve highly complex 3D distributions, the dosimeter should be capable of sampling dose in each dimension at many closely spaced points and detecting small differences in dose. However, not all RT dosimetry requires such stringent conditions on dosimeter resolution, for example, calibration of a LINAC is typically performed using point-dose measurements. Clearly, the resolution of the particular application will dictate the requirements on dosimeter resolution.

Finally, an ideal dosimeter will be tissue equivalent as well as dose integrating and reusable. It is highly advantageous for the response of the dosimeter to mimic that of human tissue in terms of radiation absorption and scattering properties. This allows direct measurement without the need for correction factors that adjust dose readings to obtain a measure of dose in a patient. Similarly, an integrating dosimeter provides a measure of absorbed dose for the entire treatment session, negating the need to acquire multiple measurements to adequately verify the full dose. Reusability is also desirable for RT dosimeters as many can be costly or difficult to replace, however, this is not necessary for reliable dose measurements.

1.3 Current Radiation Delivery Verification Tools

A variety of dose measurement tools are available in modern RT for commissioning and regular quality assurance (QA) of radiation delivery devices, commissioning of

new treatment processes, QA of specific patient treatment plans and *in-vivo* dosimetry for patient treatment verification. Each tool can be broadly categorized based on its ability to determine dose at a point, over a two-dimensional (2D) plane or throughout a 3D volume. This dissertation focuses on developing a 3D dosimetry system for verifying complex RT dose distributions using polymer gel dosimeters. Gel dosimeters provide a superior dose measurement tool compared to point and 2D dosimeters in cases where steep dose gradients are present, such as in IMRT or SRS treatments, as they are capable of adequately sampling the dose distribution throughout the treatment volume. This section provides an overview of the most common point, 2D and 3D tools used for dose verification in modern RT and discusses their position in the QA process.

1.3.1 Point Measurement Tools

Point verification tools include ionization chambers and solid state detectors, such as diodes and thermoluminescent detectors (TLDs). An ionization chamber typically consists of a solid cylindrical envelope housing an air-filled cavity and collector electrode. A potential difference applied between the envelope and electrode attracts ions produced from radiation disassociation of air molecules. The amount of charge collected is proportional to the dose delivered to the chamber and can be measured using an electrometer [10, 25]. Ionization chambers are best suited for point-dose measurements in regions where the dose is relatively homogenous and are most commonly used for LINAC calibration, commissioning and routine QA measurements. They should be avoided in regions of steep dose gradient where perturbations in dose measurements may result from the inherent volume-averaging effect associated with these devices [27].

Solid state detectors include diodes, diamonds, metal oxide silicon field effect transistors (MOSFETs), optically stimulated luminescence (OSL) dosimeters and TLDs. When these devices are exposed to ionizing radiation, electron-hole pairs are created in the detector material, resulting in a radiation-induced current that is proportional to the absorbed dose [9, 10]. Using diode or diamond detectors, the current is measured directly, while in MOSFETs, the current produces a measurable shift in the bias voltage of the detector system [28, 29]. In the case of OSL dosimeters and TLDs, the radiation-induced current can only be measured after the detector is exposed to light or heat, respectively. This releases electrons trapped in the detector material

as well as visible light which is converted into a measurable electric current using a photomultiplier tube [9, 10]. Solid state detectors can be found in personnel monitoring devices and are often used for *in-vivo* surface dose measurements. They are attractive tools for verifying dose at a point, but suffer from a number of inherent limitations, including dependencies on detector orientation, dose rate and radiation energy, and are therefore not suitable for complex dosimetry situations [27, 30].

1.3.2 Two-Dimensional Measurement Tools

Modern 2D dose measurement tools include film and array detectors. Traditionally, film dosimetry was performed using radiographic film but is now more commonly performed using radiochromic film. Radiochromic film is insensitive to optical photons [24] and develops on its own using a solid-state polymerization process [31], making it an attractive 2D dosimeter. It is typically used for acquiring beam profiles during commissioning and regular QA of radiation delivery devices. In some RT clinics, film is still used for routine QA of complex treatments, such as IMRT, but is quickly being replaced by pseudo-3D dose measuring tools. In addition, care must be taken with radiochromic film due to the inherent directional dependence of its response, which can lead to large variations in dose measurements, even for homogenous radiation fields [24].

Array detectors, which have gained popularity in recent years, measure dose over a 2D plane using hundreds of diode detectors or ionization chambers arranged in a square pattern [27]. These detector systems are convenient and efficient and are typically used for QA of IMRT treatments. However, the inherent low spatial resolution of array detectors (on the order of 1 cm) limit their use to routine QA for IMRT treatments that have been previously commissioned by a more reliable technique [27]. In addition, array dose verification systems retain many of the disadvantages associated with diode and ionization chamber point detectors summarized above and are only capable of verifying single external radiation beams [27].

1.3.3 Three-Dimensional Measurement Tools

While point and 2D dose measurement tools play an important role in many RT applications, such as LINAC calibration and commissioning, 3D dose measurement tools are necessary to fully assess treatments containing complex dose distributions with steep dose gradients. These types of treatments have become increasingly more

common in modern RT due to use of new treatment machines and techniques and require a truly 3D dosimetry system as part of their QA program. To date, methods for approximating 3D dose distributions based on 2D measurements have emerged, however, radiochromic plastics and polymer gel dosimeters (figure 1.9) remain the only truly 3D dose measurement tools available.

One option for measuring dose in 3D is to arrange multiple 2D dosimeters at different locations throughout a 3D volume. In the past, multiple sheets of film or 2D array detectors were stacked to acquire 3D data. More recently, a commercial dosimetry system called ArcCheck was introduced that uses an array of diodes arranged in a helical pattern to sample the dose in a 3D volume [32]. ArcCheck shows great promise for use in routine treatment QA, but similar to the array detectors described above, suffers from inherently low spatial resolution. This will likely restrict ArcCheck to verification of distributions already commissioned by another technique.

Another option for acquiring 3D dose measurements involves using the electronic portal imaging device (EPID) mounted on the LINAC opposite the treatment beam. Images of the 2D fluence pattern delivered by the LINAC for a given treatment field are recorded by the EPID and used in conjunction with a sophisticated dose calculation algorithm to reconstruct the 3D dose distribution [33]. This procedure is typically used for IMRT QA, including pre-treatment verification with or without a phantom [34] and *in-vivo* dose measurements during patient treatment [35]. While EPID-based verification is gaining ground in many RT clinics, measurements are made for each treatment field individually and inaccuracies in the composite dose distribution resulting from all treatment fields may be missed [27]. In addition, for pre-treatment QA, this technique often requires the treatment plan be transformed to deliver the dose distribution to a simpler target geometry than the patient [36].

To date, only one radiochromic plastic dosimeter, called Presage, is available for 3D verification of modern RT treatments. Presage is composed of a clear polyurethane matrix containing a leuco-dye that changes colour upon exposure to radiation [37, 38]. This colour change produces an increase in optical density that is a function of absorbed radiation dose. Typically, dose information is extracted from the Presage phantom using optical computed tomography (OptCT) [37–42]. Presage dosimeters show great promise for complex dose verification but are only available from one supplier and require dosimetric correction factors to account for their lack of radiological tissue equivalence [38].

Polymer gel dosimeters are a truly 3D radiation verification tool, capable of pro-

viding dose readings with a high degree of spatial and dosimetric resolution. They are tissue-equivalent hydrogels composed of radiosensitive monomers infused in a gelatin matrix that polymerize as a function of absorbed radiation dose. Figure 1.9 shows a 1 L gel exposed to ionizing radiation at the top and bottom of the container (white regions). The recorded dose information can be extracted from the gel using MRI, OptCT, CT, or US to produce high resolution, 3D maps of the dose distribution [43]. Overall, polymer gels offer a superior tool for measuring dose in 3D, but require a more involved procedure for obtaining dose readings than other dosimetry systems such as the EPID or ArcCheck. For this reason, PGD is best suited for commissioning of new treatment techniques and evaluating end-to-end processes to ensure accurate patient localization and dose delivery. A detailed summary of PGD is provided in chapter 3.

Figure 1.9: A polymer gel dosimeter exposed to ionizing radiation at the top and bottom of the container (white regions). Gel dosimeters are truly 3D radiation measurement tools that show great promise for complex treatment verification.

1.4 Dissertation Scope

The goal of this dissertation is to develop a PGD system for verification of complex RT dose distributions using a new polymer gel formulation. The new gel recipe is optimized for use with CT readout and shows great promise for 3D dosimetry [44]. Development of the system is carried out in three stages: characterization of

the essential dosimetric properties of the new gel formulation, commissioning of a multislice CT scanner for fast and reliable imaging of 3D gel volumes and investigation of a dose rate dependence found during gel characterization. Each stage of system development is introduced below.

The first stage of this work characterizes the essential dosimetric properties of the new gel formulation, including its temporal and spatial stability, batch reproducibility and dose rate dependence. This is a critical step for any dosimetry system to ensure accurate and reliable dose measurements are obtained under a variety of operating conditions. Overall, the gel exhibits favourable dosimetric properties for 3D dosimetry. However, a dose rate dependence is found for the gel when irradiated with machine dose rates between 100 - 600 MU/min.

The second part of this work focuses on commissioning a new multislice CT scanner for CT PGD. Studies are performed to determine the optimal imaging parameters and scanning procedures necessary to acquire consistently high quality images of a 3D dose distribution throughout a gel volume. The resulting protocol is then used to characterize the image quality and density distribution of a gel dosimeter before exposure to ionizing radiation. This provides a baseline measure of image noise and uniformity for the new gel formulation as well as information on the consistency of image quality throughout an active gel volume.

The final stage of this work examines the dose rate dependence of the new gel formulation found during gel characterization. Initial investigations focus on evaluating the dependence of gel response on different types of dose rate beyond machine dose rate. Further work is performed to try to mitigate the dose rate effect by altering the chemical composition of the gel as well as determine the cause of the observed dose rate dependence.

Prior to the results for each stage of this dissertation, detailed overviews of CT imaging and PGD are provided in chapter 2 and chapter 3, respectively. The methods and materials common to each study are then provided in chapter 4. Conclusions drawn from this work as well as a summary of future directions for further investigations are given in chapter 8.

Chapter 2

X-ray Computed Tomography

X-ray computed tomography (CT) is a medical imaging technique that uses x-ray attenuation information to generate contiguous 2D images of patient anatomy. Images are reconstructed from x-ray transmission measurements collected using an x-ray tube and array of x-ray detectors. A single transmission measurement made by one detector is called a projection and provides attenuation information along the ray through the patient joining the x-ray source and detector. In a typical modern CT scan, over 1000 projections are acquired at different angles to reconstruct each 2D image [45]. Together, these images provide a 3D representation of the internal anatomy of the patient and are invaluable for many clinical applications, from osteoporosis screening to cancer diagnosis. This chapter provides a general overview of CT imaging, beginning with a brief history of scanner development and summary of the technique in section 2.1. Modern CT scanners are described in section 2.2, followed by an overview of image reconstruction in section 2.3. Section 2.4 provides details on image noise and artifacts.

2.1 Introduction

2.1.1 History

The development of modern CT imaging dates back as early as 1957 when Allan M. Cormack began developing a prototype CT scanner for determining x-ray attenuation coefficients in the body. Ten years later, Sir Godfrey Hounsfield independently designed and built the first clinical CT scanner, which became available for patient imaging in the early 1970s. Since that time, several CT scanner designs have emerged,

each offering improvements over previous scanner generations [46, 47].

Figure 2.1a provides a schematic diagram illustrating a first generation CT scanner. These systems, developed by Hounsfield, used a rotate-translate geometry and consisted of a pencil x-ray beam and two x-ray detectors. Each detector measured x-rays transmitted through the patient for a given image slice. As the system translated across the field of view (FOV), a series of parallel projections were acquired through the patient. The entire system was then rotated by 1° and the x-ray tube and detector system were again translated across the FOV. This process was repeated until 180° of projection data were collected [45] for each image slice, which required approximately 5 minutes due to the inherent motion of the x-ray source and detector system [46].

The narrow pencil beam employed by first generation scanners is optimal for preventing scattered photons from reaching the detectors, but the time required to obtain sufficient data can lead to significant image artifacts caused by patient motion. For this reason, second generation scanners were quickly developed to reduce the overall scanning time by using a narrow fan-beam of x-rays and a linear array of 30 x-ray detectors [45]. Figure 2.1b shows a second generation system, which utilized a rotate-translate geometry similar to first generation scanners, but was capable of acquiring data for a given slice in less than 20 seconds. This was an important advancement for body imaging as many patients can hold their breath for the duration of scanning, leading to a dramatic reduction in motion artifacts [46].

By the mid-1970s, third generation CT scanners, shown in figure 2.1c, were developed in response to the continuing need for rapid scanning [45, 48]. They employ a rotate-rotate geometry in which an x-ray tube is fixed to a rotating gantry opposite an arc of x-ray detectors. Both the x-ray tube and detectors rotate around the patient on a hollow circular gantry. During rotation, the x-ray tube emits a continuous beam of x-rays wide enough to image the entire patient (typically about 60° [45]), while the detectors acquire x-ray intensity measurements from several different angles. Transmission of power and data is achieved through slip ring technology, eliminating the need for lengthy cables. Third generation CT scanners with slip ring technology dramatically reduced scan time by eliminating the linear translation required by earlier scanners and avoiding the extra time required to wind and unwind cables.

Although the use of a rotating system represents a major step forward in CT imaging, the original third generation scanners were highly susceptible to ring artifacts caused by changes in the gain of each detector. In these systems, two different

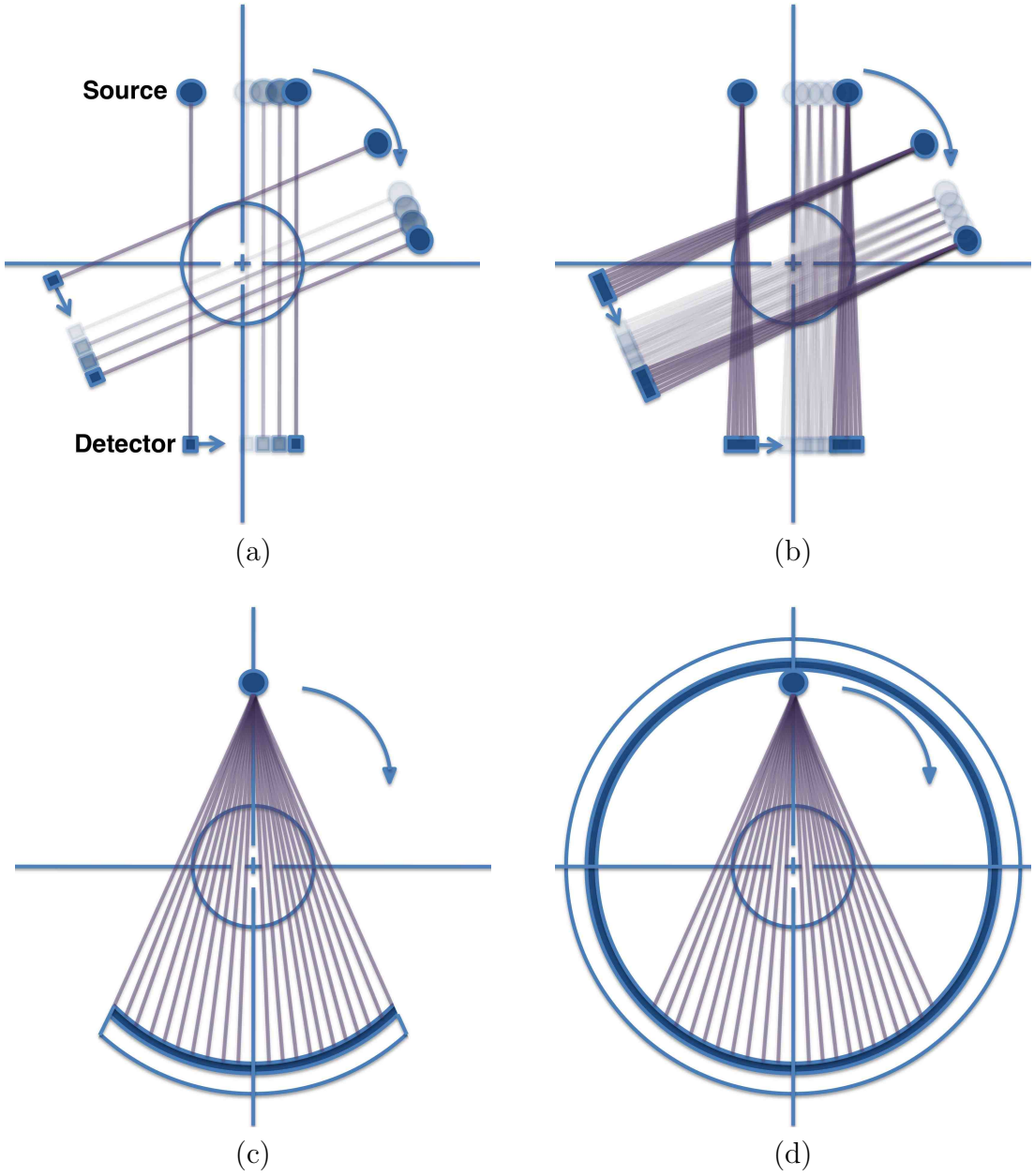

Figure 2.1: (a) First generation CT scanners used a pencil beam and translate-rotate geometry for image data acquisition. (b) Second generation systems acquired image data using translation and rotation of a narrow fan-beam of x-rays. (c) Third generation CT scanners use an x-ray tube and arc of detectors that rotate around the patient to collect projection measurements. (d) Fourth generation scanners use an x-ray tube that rotates within an entire ring of x-ray detectors to produce patient images.

detector elements determine the incident and transmitted x-ray intensity for a given projection measurement. Any drift in the response of either element can cause rings to appear in the final CT image. Fourth generation CT scanners, shown in figure 2.1d, were designed to overcome this problem using an entire ring of stationary detectors, allowing both measurements to be made by the same detector element. While eliminating issues associated with detector drift, fourth generation scanners require a large number of detectors, making them more expensive than third generation systems. High cost combined with significant advancements in ring artifact prevention and removal have meant fourth generation scanners will largely be phased out of clinical use [45, 46].

In addition to the scanner generations described above, recent advancement of third generation scanners has further reduced scan time in CT imaging. Helical scanning, introduced in the early 1990s [49], dramatically improves scan time by translating the patient through the gantry while the x-ray beam is turned on. This is in contrast to traditional axial CT imaging, where the patient is translated between acquisition of data for each image slice. Further improvements to scan time were also made with the introduction of multislice CT scanning [50]. Using a cone-beam of x-rays and adjoining rows of detector elements, multislice scanning allows whole sections of patient anatomy to be imaged simultaneously. Images can be acquired in axial mode or helical mode for even faster scanning.

Advancements in CT technology through the 2000s lead to the development of four-dimensional CT (4DCT), facilitating visualization of patient anatomy over time [51]. This type of scanning has largely benefit from cine mode acquisition, where projection data are continuously collected at a given slice position for a fixed period of time. Images are then reconstructed for a series of consecutive time points and viewed sequentially as a movie to illustrate movement of patient anatomy. This type of scanning is particularly important for abdominal and lung imaging for RT treatment planning, as motion can distort the shape of tumours and critical structures in CT images [52].

2.1.2 Overview of CT Imaging Technique

Modern CT imaging is performed using a third generation scanner capable of acquiring images of patient anatomy in less than a few seconds [45, 47]. The system consists of several components that work together to produce the final set of images. These

include a patient couch, rotating gantry, x-ray tube and detectors, high-voltage generator, data acquisition system (DAQ), image processor and computer control console. Figure 2.2 provides a schematic diagram illustrating the major components of a CT scanner and their relationships to one another [46].

During a typical CT exam, a technologist positions the patient on the CT couch such that the long axis of the patient is parallel to the z-axis of the CT room coordinate system [45] and images are acquired in the xy-plane. Each image is an axial slice through the patient. Following patient positioning, the technologist proceeds to the computer control console to prescribe appropriate imaging parameters. These parameters usually include the scan mode, x-ray tube current and voltage, slice thickness, gantry rotation speed, image reconstruction kernel and the start and end locations of the scan [46]. As many parameters affect the quality of CT images, a protocol consisting of predefined parameter values for a given anatomical site will often be used to achieve optimal image quality. A detailed summary of CT imaging parameters and their influence on image quality is given in section 2.2.3.

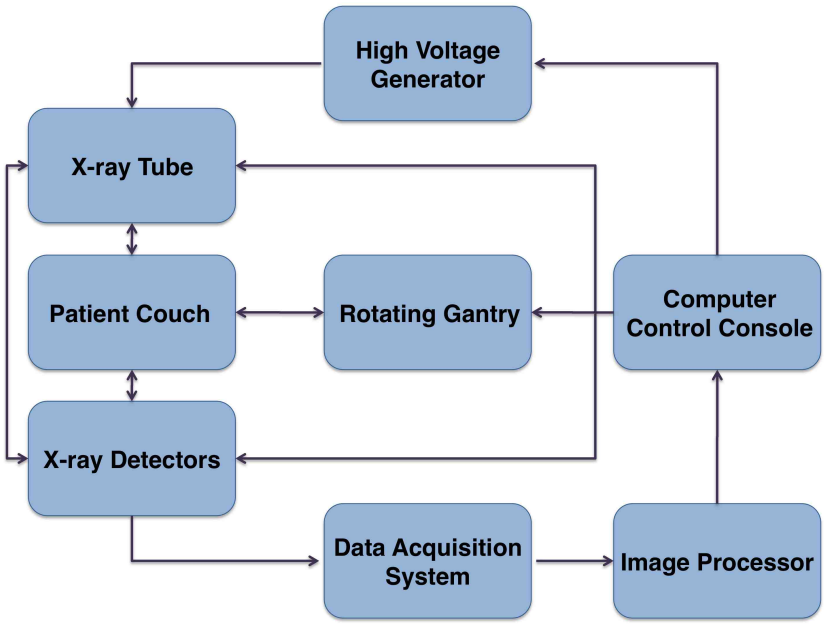

Figure 2.2: The components of a modern CT system and their relationships to one another.

Following selection of scanning parameters, the technologist initiates the scan, causing the computer control console to send a series of commands to the other system components. First, the gantry is instructed to begin and maintain rotation at

the prescribed speed. It may take several seconds for the gantry to achieve a stable rotation as it weighs over several hundred kilograms [46]. The patient couch is then instructed to move to the scan start position and translate the patient through the gantry during the scan. Depending on the scan mode selected, the couch will move the patient at regular intervals between image acquisition (axial and cine mode) or continuously translate the patient through the gantry while the x-ray beam is turned on (helical mode). At the same time, the high-voltage generator receives commands to bring the x-ray tube current and voltage to the prescribed values and maintain it at those levels for the duration of the exam [46].

As the scan proceeds, the couch moves the patient through the gantry while the x-ray tube emits a continuous beam of kilovoltage x-rays. In early third generation scanners, a fan beam is used with a single row of x-ray detectors, while more recent scanner models employ a cone beam and multiple detector rows. Using either configuration, as the beam passes through the patient, the detectors measure the intensity of the incident and transmitted photons while the DAQ samples the output from each detector at a uniform rate [46]. Up to 4000 projection measurements can be made for a given image slice [45]. The analog detector signals are then converted to digital signals and transferred to the image processor for image reconstruction using filtered backprojection. Many modern scanners offer iterative reconstruction techniques as an optional feature but filtered backprojection, described in section 2.3.2, is still the most widely using image reconstruction method [45]. Once the data are processed, images are sent to the control console for viewing by the technologist, who examines the scan to determine if the images cover the required anatomical area.

2.2 Modern Computed Tomography Scanners

This section provides a detailed description of third generation CT scanners. Section 2.2.1 describes the operation and performance of the major components of third generation systems. Modes of CT image acquisition are presented in section 2.2.2, followed by a discussion on CT imaging parameters and their affect on image quality in section 2.2.3.

2.2.1 Major Components

An overview of how the major components of a third generation CT system work together to produce patient images was provided in section 2.1.2. While each component is essential for the operation of the scanner, the x-ray tube and detectors are the most important system elements as they produce and measure the x-ray photons required for the scan [46]. These components are described in more detail below.

Figure 2.3 provides a schematic diagram of a typical x-ray tube, consisting of an anode situated opposite a cathode in an evacuated metal envelope. The anode is a metal target, typically composed of a tungsten-rhenium alloy brazed onto a graphite body [45, 46]. The cathode is also composed of tungsten and consists of a filament connected to a circuit that heats the filament through electrical resistance. This causes electrons to leave the filament surface through the process of thermionic emission at a rate determined by the filament current and temperature [45]. When a potential difference is applied between the anode and cathode, the electrons accelerate across the evacuated chamber and strike the anode. This produces bremsstrahlung photons with a spectrum of energies as well as characteristic x-rays at discrete energy levels that depend on the target composition [9, 26, 45]. The resulting x-ray beam then passes through the output port which contains a filter to remove low energy photons and reduce dose to the patient [45].

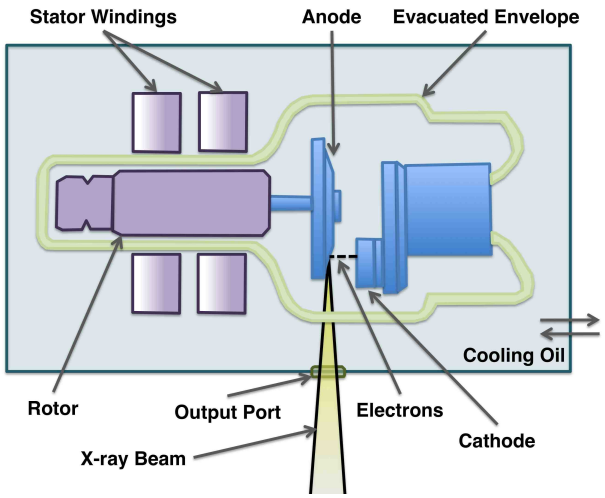

Figure 2.3: A typical x-ray tube consisting of an anode situated opposite a cathode in an evacuated metal envelope. Electrons boiled off the cathode accelerate across the envelope and strike the anode to produce kilovoltage x-rays [45].

In addition to x-ray photons, a substantial amount of heat is produced in the anode as a result of electron bombardment. The target can reach temperatures up to 2700°C at the impact point of the electrons [46], which can melt the anode and damage the surrounding components of the x-ray tube. To prevent the target from overheating, the anode is rotated using a rotor and stator windings. This distributes the heat produced by electron bombardment over a larger area of the target. The entire x-ray tube is also submerged in an oil bath to allow heat to radiate away from the system into the cooling reservoir. Nevertheless, imaging protocols that place excessive load on the x-ray tube, by requiring high photon intensity or a long exposure time, can produce enough heat to damage the system. For this reason, modern CT scanners are equipped with a computer algorithm that estimates the amount of heat that will be produced during a scan for a given set of imaging parameters. If the x-ray tube is at risk of heat damage, the algorithm will recommend a reduced technique or cooling period before the scan can be initiated [46].

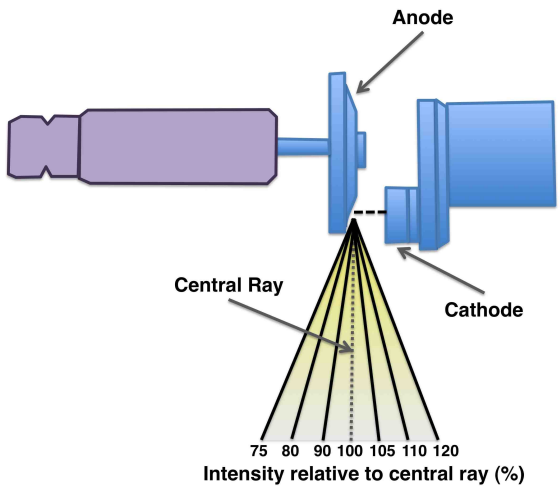

Figure 2.4: X-rays generated at different depths in the anode of an x-ray tube experience different amounts of attenuation as they pass through the anode material. The resulting x-ray beam exhibits a dramatic variation in intensity known as the heel effect.

Another issue associated with the x-ray tube is the anode heel effect, a phenomenon in which the x-ray spectrum and intensity vary across the photon beam [46]. Since x-rays are generated at different depths in the target material, they suffer different amounts of attenuation as they pass through the anode [9]. As a result, x-rays toward the anode end of the tube have a higher average energy than those emitted toward the cathode end. A non-linear reduction in photon intensity is also

observed along the anode-cathode axis of the x-ray field [46]. Figure 2.4 illustrates the reduction in photon intensity relative to the centre of the x-ray beam, where variations of up to 45% can be observed between the anode and cathode end of the tube. However, no significant variation in photon intensity is observed in the plane of the image [53]. For this reason, the x-ray tube in most CT scanners is oriented such that the anode-cathode axis is parallel to the z-axis of the scanner. This eliminates issues associated with the heel effect for single slice scanners, where the coverage along the patient in the z-direction is relatively small [46], but may influence image quality in multislice scanners where greater regions of the patient are imaged using a cone-beam of x-rays. The heel effect may also become more prominent with prolonged use of the x-ray tube [53].

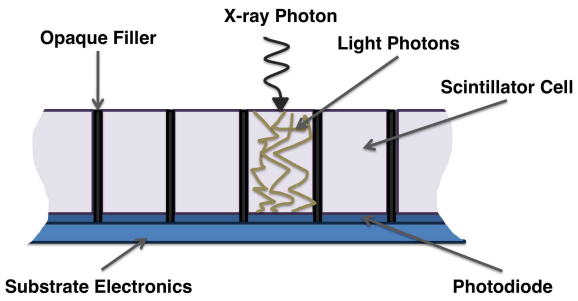

Figure 2.5: A typical CT detector composed of individual scintillating blocks connected to photodiodes and layered on substrate electronics. X-ray photons interact with each scintillator block to produce visible light that is measured by the photodiodes and used to determine the intensity of the incident x-ray beam [45].

The x-ray detector system is equally important to the x-ray tube for acquisition of patient data in CT imaging. Modern CT scanners use a solid state detector similar to that shown in figure 2.5. Individual detector cells made of a scintillating ceramic material, such as cadmium tungstate ($CdWO_4$) or gadolinium oxysulfide (Gd_2O_2S), are coupled to photodiodes and layered on substrate electronics. An opaque filler is inserted between adjacent elements to reduce detector crosstalk. Under typical operation, x-ray photons incident on the detector undergo photoelectric interactions in the ceramic material, producing electrons that go on to excite the atoms in the scintillator. As the atoms return to the ground state, they release characteristic photons in the visible or ultraviolet spectrum, that travel to the photodiodes and produce electrical signals. The current produced in the diodes is directly proportional to the intensity of light photons and by extension the intensity of the x-ray beam

[45, 46]. Intensity measurements are made using one row of 13 - 16 mm wide detector cells in single slice scanners, while a 2D matrix of 0.625 - 1.25 mm detector elements is employed in multislice scanners [45]. A schematic diagram illustrating the detector configurations for single and multislice scanners is provided in figure 2.6.

Several factors influence the performance of solid state detectors in CT imaging. The efficiency of the detector depends on the thickness and composition of each scintillator block as well as the thickness of collimator plates, or septa, placed above the detector elements to reject scattered radiation. As the thickness and linear attenuation coefficient of the scintillator elements increase, more photons are intercepted and absorbed by the detector, increasing the efficiency of the system. However, impurities in the scintillator material can reduce efficiency by preventing excited electrons from returning to the ground state and causing an overlap in measured signals. Similarly, while thicker septa are more effective at attenuating scattered radiation, they may reduce detector efficiency by preventing primary photons from reaching the scintillator blocks. In addition to detector efficiency, image artifacts may result from variations in the channel-to-channel gain of each detector element, caused by radiation damage or changes in the ambient temperature of each detector element [45, 46]. Image artifacts are described in detail in section 2.4.2.

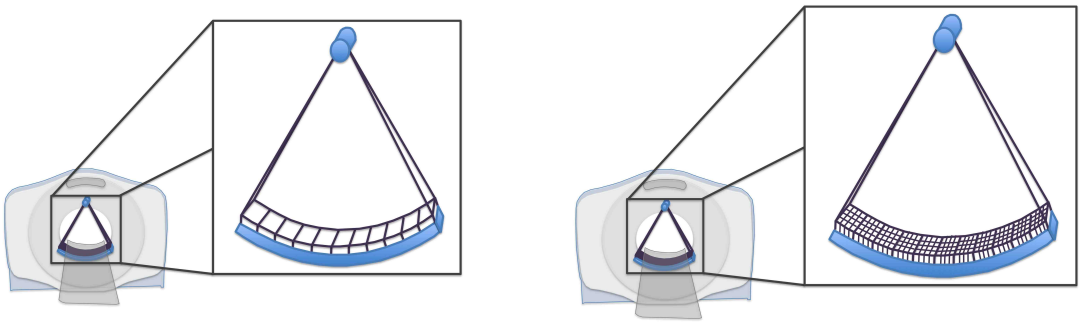

(a) (b)

Figure 2.6: Schematic diagram illustrating the detector configurations used in (a) single and (b) multislice CT scanners [45].

2.2.2 Modes of Acquisition

Modern CT scanners are capable of acquiring patient images using a number of different acquisition modes, including axial, helical, cine, cardiac, and perfusion mode.

However, most CT scans used for RT treatment planning are acquired using axial, helical or cine mode. Figure 2.7 provides a schematic diagram illustrating each CT scan mode commonly used in RT imaging.

Axial mode, shown in figure 2.7a, is a basic step-and-shoot CT imaging technique, where the patient advances into the gantry at regular intervals and x-ray intensity measurements are acquired while the couch is stationary. The patient is advanced into the gantry to the scan start position and the x-ray tube emits a continuous fan or cone beam of x-rays for one 360° rotation around the patient. At this stage, the x-ray beam returns to its inactive state while the patient moves further into the gantry. Using a single slice scanner, the interval the couch advances depends on the inter-slice spacing, while for multislice scanners, the couch travels a distance equal to the width of the detector array. With the patient at the next couch position, another 360° of projection data are acquired. This sequence of patient translation and data collection is repeated until the prescribed anatomical area is covered [45, 46].

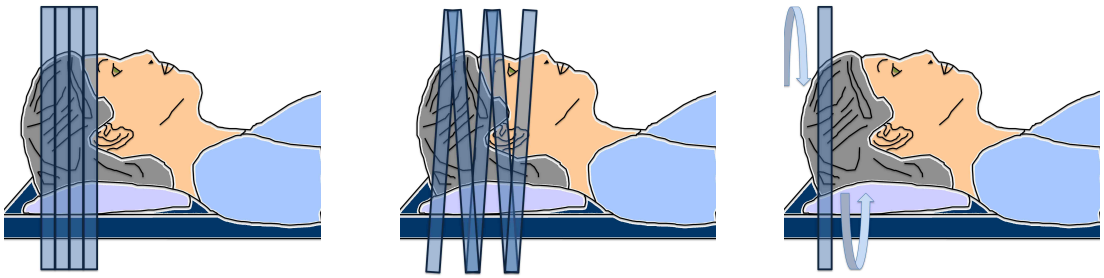

(a) Axial Mode (b) Helical Mode (c) Cine Mode

Figure 2.7: The modes of acquisition commonly available on modern CT systems, including (a) axial mode, (b) helical mode and (c) cine mode.

While axial mode provides CT images of sufficient quality, it is associated with low scan time efficiency due to the time required to start and stop the scan while the couch translates through the gantry [46]. Helical scanning, shown in 2.7b, overcomes this limitation by moving the patient through the gantry at a constant speed while the x-ray tube and detectors continuously collect x-ray intensity measurements. The raw data are interpolated during image reconstruction to produce a set of contiguous planar images of patient anatomy. The effectiveness of data interpolation is highly influenced by the scan pitch or advancement of the patient couch per rotation of the gantry relative to the thickness of the x-ray beam. The formal definition of pitch, p, is given in equation 2.1 where s is the distance the couch travels per gantry rotation

and d is the x-ray beam width.

$$p = \frac{s}{d} \tag{2.1}$$

Most modern CT scanners allow a pitch between 0.75 - 1.5 for helical scans. A pitch less than one results in the x-ray tube tracing a tightly wound helix which can lead to overscanning and unnecessary dose to the patient. A pitch greater than one corresponds to a loosely wound helix and is more typical in CT exams, while a pitch of one corresponds to contiguous axial imaging [45, 46].

In addition to axial and helical mode, most modern CT scanners are also capable of acquiring images using cine mode. This technique, illustrated in figure 2.7c, is similar to axial mode in that images are acquired at a given couch position and the x-ray beam is turned off while the patient translates through the gantry. However, cine mode allows x-ray intensity measurements to be made over several 360° gantry rotations at each couch location. This produces a series of projection measurements that can be used to reconstruct a set of sequential images showing patient anatomy over time [52, 54–56]. The number of images acquired at each couch position, N, is given in equation 2.2, where T_D is the time spent at one couch location, T_R is the gantry rotation period and Δt is the time between consecutive image reconstructions [52].

$$N = (\frac{T_D - T_R}{\Delta t}) + 1 \tag{2.2}$$

For example, given a gantry rotation period of $T_R = 1$ s and data acquisition duration of $T_D = 4$ seconds, if images are reconstructed every Δt = 0.2 s, a total of $N = 16$ images will be produced at each couch position. This allows visualization of changes in anatomy over time and is of particular importance for 4DCT, an imaging technique used in RT planning of lung and abdominal cancer treatments [52, 54–56].

2.2.3 Imaging Parameters

Modern CT scanners are equipped with several protocols containing predefined imaging parameters for each type of scan and anatomical site. These parameters typically include the x-ray tube voltage and current, gantry rotation time, slice thickness, FOV and image reconstruction kernel. Each parameter influences the resulting image quality and patient dose and can be adjusted in the protocol to suite the needs of the scan. However, while increasing the value of a given parameter (e.g. tube current) may improve image quality, it also exposes the patient to a higher radiation dose. As

such, a trade-off exists between image quality and patient dose that must be observed for most scanning parameters. A description of each CT imaging parameter and its impact on image quality and dose is given below.

X-ray Tube Voltage

The x-ray tube voltage is the potential difference applied between the anode and cathode of the x-ray tube. It is commonly referred to as the kV and typically varies between 80 - 140 kV on modern CT scanners [45]. The tube voltage setting determines the peak voltage applied across the x-ray tube, resulting in photons with a spectrum of energies up to a maximum value equal to the parameter chosen. For this reason, the tube voltage is also commonly referred to as the kVp. Tube voltage is an important parameter for determining the resulting intensity and energy of the x-ray beam. As the potential difference across the tube increases, the intensity of the x-ray beam increases, resulting in a greater number of photons penetrating the patient and reaching the x-ray detectors. This improves image quality by reducing image noise but introduces additional dose to the patient [9, 45]. The average energy of the x-ray beam also increases with increasing tube voltage. However, this can have a negative impact on image quality by changing the absorption characteristics of different anatomical structures, leading to a reduction in image contrast [26]. Increasing x-ray tube voltage also places greater load on the scanner as electrons strike the anode with greater energy, which results in greater heat production during scanning.

X-ray Tube Current

The tube current, or mA, is the number of electrons flowing from the cathode to the anode per unit time [45] and depends on the cathode filament operating conditions. An increase in filament current or temperature increases the number of electrons boiled off the cathode, resulting in an increase in tube current [46]. Similar to the x-ray tube voltage, an increase in tube current increases the intensity of the x-ray beam [9, 45], which reduces image noise but exposes the patient to a higher dose. A higher mA value also places more load on the x-ray tube, as a greater number of electrons strike the anode per unit time, leading to more heat generation. The range of currents available on a typical modern CT scanner fall between 10 - 800 mA, with most procedures employing a tube current between 80 - 140 mA.

Gantry Rotation Time

The gantry rotation time is the length of time required for the gantry to make one complete 360° revolution and varies between 0.5 - 4 s for a typical modern CT scanner, with most scans using a 1 s setting. A longer rotation time corresponds to a greater period of x-ray intensity measurements and greater number of x-ray photons interrogating the patient. Similar to the x-ray tube voltage and current, this results in a reduction in image noise but it also increases the dose to the patient and places greater load on the scanner. The tube rotational time is typically given with the tube current as mAs, where for example, 200 mAs corresponds to a current of 200 mA and gantry rotation period of 1 second.

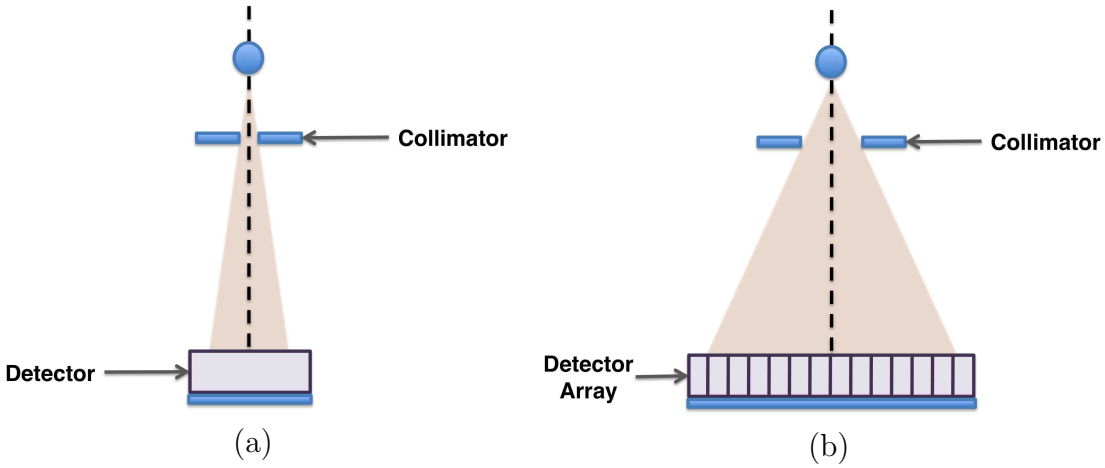

Figure 2.8: (a) Single slice CT scanners adjust slice thickness using the x-ray beam collimator. (b) Using a multislice scanner, slice thickness is determined by the number of detectors used during the exam and the collimator adjusts the x-ray beam width to correspond to the active area of the detector array [45].

Slice Thickness

In addition to the x-ray tube and gantry imaging parameters, the slice thickness is also an important technique factor in CT imaging. Slice thickness determines the width of patient anatomy parallel to the z-axis of the scanner that is compressed into each 2D image. Figure 2.8 illustrates how slice thickness is adjusted on single and multislice scanners. Using a single slice scanner, slice thickness is determined by the width of the x-ray beam which is adjusted using the beam collimator. These systems typically allow a slice thickness between 1 - 10 mm, with imaging for most RT

treatment planning utilizing 3 mm slice thickness. In multislice scanners, the detector configuration determines the thickness of each image slice and the collimator adjusts the x-ray beam to correspond to the active area of the detectors. The detectors can be used individually or can be binned to produce thicker slices. As a result, a large range of slice thicknesses are available on multislice scanners and typically range from 0.625 - 10 mm [45], with most RT planning images acquired using between 2.5 - 5 mm slice thickness. Regardless of how slice thickness is adjusted, thinner slices provide better spatial resolution in the z-direction of the scan than thicker image slices, but are reconstructed using fewer detected x-ray photons. If all other imaging parameters are kept fixed, this results in thinner image slices having greater image noise. The x-ray tube voltage and current can be increased to improve image quality, but must be done so with strict attention to the associated increase in patient dose [45].

Field of View

Similar to slice thickness, the FOV controls how much anatomy is imaged in the *xy*-plane and is determined based on the diameter of patient tissue that must be present in each image. It is typically chosen from a set of discrete values available on the scanner [8] and controls the pixel dimensions of the resulting images. For a given image matrix, as the FOV increases, the dimensions of each pixel increase, resulting in a larger number of x-ray photons contributing to the reconstructed image at the given pixel location [45]. This improves image quality by reducing noise but also reduces the spatial resolution of the image. If multiple tissues are represented in a single pixel, they may not be distinguished from one another if a large FOV is used because x-ray intensity values are averaged for each pixel. This is similar to partial volume averaging, discussed in section 2.4.2.

Reconstruction Algorithm

The imaging parameters described so far control the components of the scanner responsible for x-ray intensity measurements. In contrast, the reconstruction kernel determines how x-ray intensity measurements are filtered during image reconstruction. Several standard filters exist on most CT scanners with each filter designed to provide optimal image quality for a particular anatomical site. For example, the *SOFT* reconstruction kernel is specifically designed for imaging of soft tissue such as the prostate gland or breast, while the *BONE* kernel provides optimal image quality

for viewing bone and cartilage. Section 2.3.2 below provides further details on the process of filtered backprojection and the commonly available reconstruction filters.

2.3 Image Reconstruction

Computed tomography image reconstruction is a multistep process involving complex mathematical manipulation of x-ray intensity measurements. This section provides details on each major step of CT image reconstruction. Section 2.3.1 outlines the initial processing of intensity data while section 2.3.2 describes how each image is generated using filtered backprojection. Details about the display of the final processed images are provided in section 2.3.3.

2.3.1 Initial Processing

The raw x-ray intensity measurements acquired during a CT scan undergo several initial processing steps before image reconstruction. First, each measurement is normalized using detector calibration data obtained from air scans collected during quality assurance of the system. This corrects for inhomogeneities in measured x-ray intensity across the detectors caused by differences in photodiode or amplifier gain. In some scanners, a correction algorithm will then be applied to account for dead detector elements by interpolating the intensity values from surrounding cells. This is typically followed by application of a scatter correction algorithm, and in some cases, adaptive noise filtration to reduce noise in specific areas of each image [45].

Following normalization and correction of raw data, intensity measurements are converted into projections that provide x-ray attenuation information along the beam path. For a uniform object, the intensity of transmitted x-rays, I_t, is related to the intensity of the incident beam, I_0, by equation 2.3:

$$I_t = I_0 e^{-(\mu x)} \tag{2.3}$$

where μ and x are the linear attenuation coefficient and thickness of the object the beam travels through, respectively [10, 45]. If the object is heterogeneous, as is the case for the human body, the x-ray beam must pass through several different materials, each with its own linear attenuation coefficient, μ_i, before reaching the detectors. In this situation, each slab of patient anatomy is divided into n square

elements of equal thickness x along the path of the x-ray beam and the attenuation equation becomes:

$$I_t = I_0 e^{-(\mu_1 x + \mu_2 x + \cdots + \mu_n x)} \tag{2.4}$$

By rearranging equation 2.4 and taking the natural logarithm of both sides, a projection, p, is defined using equation 2.5.

$$p = ln(\frac{I_0}{I_t}) = (\mu_1 + \mu_2 + \cdots + \mu_n)x \tag{2.5}$$

Individual attenuation coefficients for each element are determined from the multitude of projections acquired for each slice using filtered backprojection [10].

2.3.2 Filtered Backprojection

Filtered backprojection is the most commonly used image reconstruction algorithm in CT imaging. It is a mathematical procedure designed to simulate the image acquisition process in reverse. Beginning with an empty pixel matrix, each projection measurement is filtered and then smeared or backprojected onto the matrix to produce the final image. Filtered backprojection is computationally intense and is typically performed using Fourier analysis.

To illustrate the backprojection process, consider the simplified situation illustrated in figure 2.9. Here, the object of interest is a point and multiple projection measurements have been acquired through the object from various orientations. As indicated above, each projection represents the sum of linear attenuation coefficients along the ray through the object joining the x-ray source and detector. By backprojecting a given projection measurement, the value of the summed attenuation coefficients is assigned to each element in the image matrix along the original beam path. As this procedure is repeated for each projection, the object becomes visible in the resulting image [45, 46].

If the projection data are not filtered before backprojection is performed, the reconstructed image will contain a characteristic $\frac{1}{r}$ blurring that can distort the representation of the true object. Filtered backprojection corrects this blurring and reduces image noise by filtering each projection measurement before it is smeared onto the image matrix. Filtering is conducted by convolving projection data with a convolution kernel, often referred to in CT imaging as a reconstruction kernel. In the

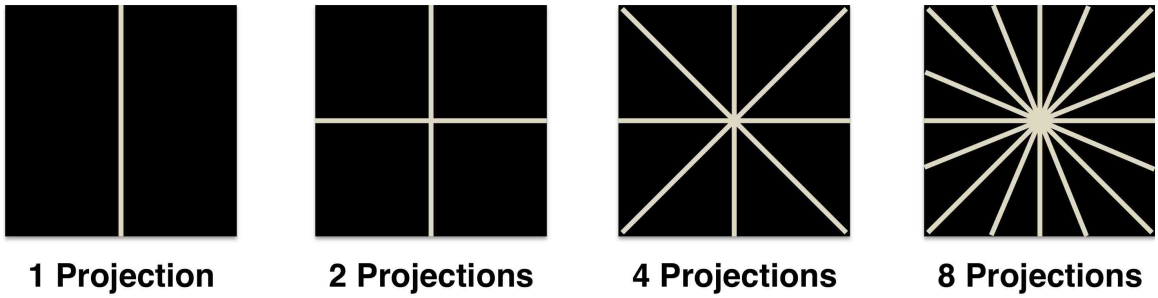

Figure 2.9: Formation of the image of a point using an increasing number of projections.

spatial domain, the filtered projection, *p'(x)*, is obtained using equation 2.6:

$$p'(x) = p(x) \otimes k(x) \tag{2.6}$$

where *p(x)* is the original projection and *k(x)* is the reconstruction kernel. However, it is much faster to perform the filtering step in the spatial frequency domain. This is accomplished using Fourier transforms to convert equation 2.6 into a simple expression involving multiplication by the reconstruction kernel instead of convolution. Equation 2.7 provides an expression for performing the filtering operation in the frequency domain, where FT and FT^{-1} are the forward and inverse Fourier transforms, respectively.

$$p'(x) = FT^{-1}\{FT[p(x) \times k(x)]\} \tag{2.7}$$

All modern CT scanners perform filtering in the frequency domain using one of several available reconstruction kernels. The choice of the reconstruction filter has a large impact on the extent of image blurring and amount of noise present in the resulting image, with each filter designed to provide optimal image quality for a particular application. For this reason, it is common to find reconstruction kernels named after the application for which they were designed. For example, the *SOFT* reconstruction kernel blurs image noise to reduce its visualization while the *BONE* filter reduces blurring in order to visualize edges and small details in the image at the expense of greater image noise [45, 57].

2.3.3 Image Display

Following image reconstruction, high-precision pixel data for each image slice are converted into integer CT numbers to facilitate image display. Each CT number, N_{CT}, is defined relative to the linear attenuation coefficient of water, μ_{water}, using equation 2.8:

$$N_{CT} = 1000\frac{\mu(x,y) - \mu_{water}}{\mu_{water}} \tag{2.8}$$

where $\mu(x,y)$ is the filtered linear attenuation coefficient backprojected onto the pixel located at (x,y) in the image matrix [58]. The CT number assigned to each pixel is expressed in Housfield units (H) in honour of Sir Godfrey Hounsfield who was an early pioneer in the development of clinical CT imaging (see section 2.1.1). Table 2.1 summarizes CT numbers for various materials found within the body which range from approximately -1000 H for air to over 3000 H for dense bone [45, 58].

Tissue	N_{CT} (H)
Air	-1000
Lung	-300
Fat	-20 to -100
Water	0
Muscle	44 to 59
Liver	50 to 80
Soft bone	1000
Dense bone	3000

Table 2.1: CT numbers for common materials found within the body [45, 58].

After applying equation 2.8, each CT number is assigned a shade of grey so that images can be displayed on a computer monitor. A typical CT image is reconstructed using a 512 x 512 pixel matrix [45] with each pixel capable of displaying 256 shades of grey [58]. Since the CT numbers in an image slice may vary by more than a few thousand Hounsfield units, it is common to restrict the range of CT numbers displayed by selecting an appropriate window width and level. The window width defines the range of CT numbers displayed for a given image with the middle value designated by the window level. For a CT image displayed this way, the tissue with the highest CT number (or a CT number above that displayed) will appear white, the material with the lowest CT number (or below the lowest value) will appear black

and all tissues in between will be displayed in various shades of grey [58]. An example of a typical CT image showing the male pelvic anatomy is illustrated in figure 2.10.

Figure 2.10: An example of a typical CT image of the male pelvic anatomy.

2.4 Noise and Artifacts

Given optimized window and level settings, the ability to discern different structures in a CT image largely depends on the noise present in the image as well the presence and strength of image artifacts. This section presents details on noise in CT imaging and provides a summary of the different image artifacts that can appear in CT images.

2.4.1 Noise

Noise in CT imaging can be defined as unwanted variation in the CT numbers or pixel values of an image. These fluctuations usually appear as graininess and result in a reduction in image clarity. Typically, the imaging parameters for a given CT scan are adjusted to minimize image noise. However as discussed in section 2.2.3, there is a trade-off between image quality and patient dose that must be observed when adjusting these parameters.

There are three main factors that contribute to image noise in a typical CT system. The first is quantum noise, also called photon or shot noise, which results from the statistical nature of electromagnetic radiation. It is determined by the number of x-ray photons that contribute to the formation of the image. As the number of photons increases, the noise in the image decreases [45]. The number of photons associated with a given scan will depend on the imaging protocol and the efficiency of the detector system. While the detector efficiency is fixed for a given scanner

design, many scanning parameters can be adjusted to increase the number of photons contributing to the image and reduce image noise. These typically include the x-ray tube current and voltage, gantry rotation speed and slice thickness [46, 57].

The remaining sources of image noise result from the physical limitations of the CT system and methods used for image processing. As indicated in section 2.1.2, the CT scanner consists of a number of components that work together to collect x-ray attenuation information. Many of these components, including the detector photodiodes and DAQ, are electrical devices which contribute electronic noise to the resulting image. Unlike for the case of quantum noise, nothing can be done to reduce electronic noise for a given system design. Noise is also present as a result of scattered radiation that penetrates the collimating plates, or septa, separating adjacent detectors. Similar to the electronic noise sources, the septa cannot be adjusted to reduce noise before a scan is initiated. In addition to the physical components of the scanner, the image generation process can also contribute to noise in an image. As discussed in section 2.3.2, the reconstruction kernel has a large impact on image noise and can be chosen to optimize image quality for a particular application. Other image processing parameters, including the FOV and size of the image matrix, are also responsible for image noise and can also be adjusted to a certain extent to improve visualization of the final images [46].

2.4.2 Artefacts

A CT image artifact is defined as any object or feature displayed in an image that does not accurately represent the anatomy being scanned. Image artifacts may occur for many different reasons ranging from suboptimal scanner design to patient motion and can appear as dark bands, streaks or rings [46, 57]. Typical artifacts in CT imaging include beam hardening artifacts, streaking artifacts, ring artifacts and partial volume artifacts.

Beam hardening refers to the preferential absorption of low energy photons as an x-ray beam passes through a material causing the average energy of the beam to become progressively greater (i.e. harder). It is more pronounced for x-rays passing through a given thickness of bone compared to the same thickness of tissue because bone is a more attenuating material due to its higher density and atomic number. Beam hardening causes cupping artifacts as well as dark streaks and bands in CT images. Cupping artifacts result when x-rays pass though a structure that is thicker

at its centre and become harder than rays passing though the edges. This occurs because the beam travels through a greater amount of material at the centre of the structure and can produce a non-uniform intensity distribution that resembles a cup inside the image. In addition, beam hardening can lead to dark streaks and bands appearing between dense structures. This is caused by greater beam hardening for projections acquired at angles where x-rays must pass through both structures compared to the beam hardening that occurs as photons pass through one structure [45, 46]. Beam hardening effects can be accounted for using correction algorithms, but their persistence in CT images can lead to misdiagnosis of patient anatomy as they often resemble pathological structures [46].

Streaking artifacts are intense bright or dark lines extending across an image and are typically caused by inconsistent projection measurements. Inconsistencies can occur for many different reasons, including abrupt changes between projections, mechanical malfunction of the scanner or issues related to the data collection process such as patient motion. One of the most common reasons for streaking artifacts is the presence of high-density implants in the patient like fillings or pacemakers. These objects attenuate the x-ray beam to such an extent that some projections in a given image slice may be missing transmission data, leading to inconsistencies between projections for a given structure. When this occurs, the backprojection algorithm is no longer capable of accurate reconstruction using the available data set and lines appear in the final image. Streaking artifacts do not typically lead to a misdiagnosis of patient anatomy but can become amplified in the presence of patient motion, leading to images that are no longer reliable for visualization of internal anatomy [45, 46, 57].

In addition to beam hardening and streaking artifacts, ring and partial volume artifacts can also obscure information in a CT image. As described in the above sections, ring artifacts are produced in third generation CT scanners as a result of discrepancies between neighbouring detectors caused by drift in detector gain or temperature. Ring artifacts can appear as either full or partial rings in the resulting images but do not typically interfere with patient diagnosis due to their dissimilar appearance to patient anatomy and pathology [46]. Similarly, the impact of partial volume artifacts on patient diagnosis has been substantially reduced in recent years [45]. Partial volume artifacts occur when the slice thickness chosen for a CT exam is large enough that multiple tissues are present within the slice along the z-axis of the scan. As the intensity measurements for a given image are combined in the slice thickness dimension, this can lead to certain features of the anatomy or pathology

being missed in the exam. However, as modern CT scanners are capable of acquiring images with sub-millimeter slice thickness, partial volume artifacts have been largely eliminated in recent years [45].

Chapter 3

Polymer Gel Dosimetry

This chapter provides a overview of polymer gel dosimetry (PGD), beginning with a brief history of the field and a summary of the general methodology in section 3.1. Section 3.2 presents polymer gel chemistry and includes an overview of the reaction mechanisms responsible for polymer formation as well as details on the properties of the polymer formed. This is followed in section 3.3 by an overview of the imaging modalities used in PGD to extract dose information and a discussion on how the performance of dose measurement is assessed in section 3.4. Section 3.5 summarizes studies presenting clinical applications of PGD for RT dosimetry.

3.1 Introduction

3.1.1 History

The inception of gel dosimetry can be traced back to 1950 when Day and Stein showed gels containing dyes, such as methylene blue, change colour upon exposure to ionizing radiation [59]. In 1957, radiation beams were visualized in a chloral hydrate agar gel containing methyl red and depth dose data were recorded using spectrophotometry as well as pH and electrical conductivity measurements [60]. Around the same time, it was suggested that polymer systems containing solid polymethylmethacrylate could be used for radiation dosimetry [61] and by the early 1960s studies reported radiation induced polymerization in liquids [62] and the use of polyacrylamide for gamma dosimetry [63].

Several years later, Gore *et al.* showed radiation induced changes in Fricke or ferrous sulphate solutions [64] could be measured using nuclear magnetic resonance

(NMR) imaging [65], marking the beginning of modern gel dosimetry. Further work by Appleby *et al.* [66] led to the development of the Fricke gel dosimeter, consisting of a ferrous sulphate solution infused in a gelatin matrix, that could be used to obtain 3D dose information using MRI readout [66]. However, it was soon discovered that Fricke gel dosimeters were not capable of maintaining a spatially stable dose distribution due to ion diffusion [67] and the diffusion persisted in the presence of chelating agents [68].

The discovery of ion diffusion in the Fricke system led to the development of a new gel dosimeter in the early 1990s based on the radiation induced polymerization of monomer molecules. The original recipe consisted of acrylamide (AAm) and N,N'-methylenebisacrylamide (BIS) monomers infused in an agarose matrix [69] that formed a crosslinked polymer network upon exposure to ionizing radiation. Similar to the Fricke dosimeter, dose information was extracted from the gel using MRI. The new recipe did not display the diffusion problems associated with the Fricke gel, however, oxygen inhibition of the polymerization reactions required this formulation be fabricated in a nitrogen filled glove-box and maintained in an oxygen-free environment. The recipe was subsequently refined in 1994 by replacing agarose with gelatin [70] and patented under the acronym BANG (i.e. BIS, AAm, Nitrogen and Gelatin) but is commonly referred to as polyacrylamide or PAG gel in the gel dosimetry literature.

From the mid 1990s to the mid 2000s, studies were undertaken to better understand the chemical processes associated with polymer gels [71–76], new gel formulations were designed with alternative monomers for use with MRI [77, 78] and several clinical applications were investigated [43]. Alternative imaging modalities were also introduced for dose readout, including OptCT [79–83], CT [84], US [85] and Raman spectroscopy [86]. Alongside these developments, a key advancement was reported by Fong *et al.*, who designed a new type of gel dosimeter that could be fabricated in the presence of oxygen [87]. By incorporating an antioxidant into the new formulation, dissolved oxygen was prevented from inhibiting the radiation induced polymerization reactions. Further work to compare a number of different antioxidants revealed that tetrakis (hydroxymethyl) phosphonium chloride (THPC) provided the most efficient oxygen scavenging for gels made under normal atmospheric conditions [75]. This new class of polymer gels became known as *normoxic* gels, while older recipes that require an oxygen-free environment are now referred to as *hypoxic* or *anoxic* gels.

In the last decade, authors have continued to investigate clinical applications of PGD [43] and study the fundamental chemistry of polymer gels [88–94]. At the same time, new gel formulations have emerged that consist of less-toxic monomers [95], such

as the N-isopropylacrylamide (NIPAM) monomer used in the present work, as well as radiochromic dosimeters. As mentioned in section 1.3.3, the first radiochromic plastic dosimeter, known as Presage, changes colour when exposed to ionizing radiation, making it ideal for OptCT readout [37–42]. More recently, micelle gels, consisting of a leuco-dye embedded in micelles and emulsified in gelatin [96, 97], were introduced into PGD along with genipin gels, made of genipin, gelatin and water [98]. Similar to Presage, these new gels change colour when irradiated and dose information is extracted using OptCT. Both micelle and genipin gels show promise for 3D dosimetry, however, recent work indicates fine-tuning of the micelle formulation is necessary before use in clinical applications [99].

3.1.2 Overview of PGD Technique

Modern PGD studies are carried out with normoxic gels following a procedure that is common to each gel formulation and dose readout technique. This process, illustrated in figure 3.1, consists of four main steps, namely, fabrication, irradiation, imaging and data processing. During fabrication, radiosensitive monomers are dissolved in a gelatin solution that is subsequently infused with an antioxidant such as THPC. As mentioned above, this prevents oxygen inhibition of the polymerization reactions and allows gel fabrication to proceed on the bench-top.

Following fabrication, the completed gel solution is poured into oxygen-impermeable vessels. Traditionally, the gel is divided between calibration and test irradiation containers, but the gel can also be transferred to a single vessel used for both irradiations. Once poured, the gel is left to set in a temperature-controlled environment until solid. If two separate vessels are employed, it is recommended they be the same size to avoid discrepancies in dose response resulting from differences in the cooling rate of each gel during storage [88] and heat produced during and after irradiation [76, 89, 92].

Once the gel has solidified, the radiation is delivered, and the gel is left for a predetermined amount of time to allow the polymerization reactions to come to completion. Because the amount of polymer formed depends on the rate of polymerization, which in turn depends on the temperature of the gel, a consistent temperature must be maintained during and after irradiation to ensure accurate dose measurements [89].

Following stabilization of polymerization, dose information is extracted from the gel using one of several imaging techniques. The most common imaging modalities used are MRI, OptCT, and CT and are described in detail in section 3.3. Once the

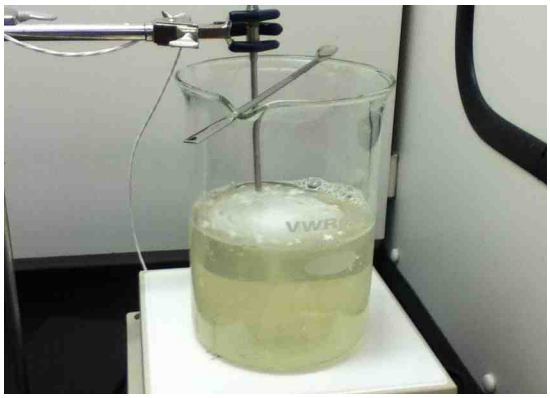

(a)

(b)

(c)

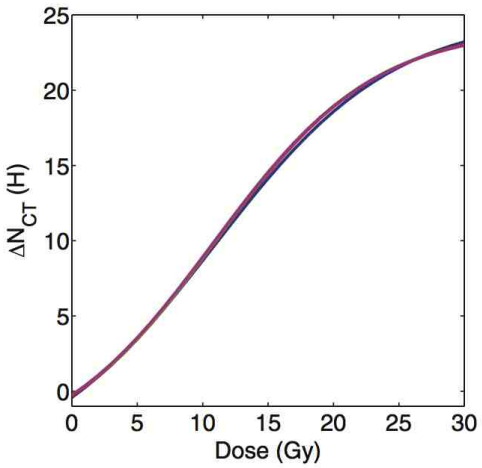

(d)

Figure 3.1: The PGD process, consisting of (a) fabrication, (b) irradiation, (c) imaging and (d) data processing.

images are obtained, the data is processed. Images of the calibration irradiation are compared to the known dose distribution (typically provided by the TPS) to construct a calibration or dose response curve, which is subsequently used to convert the test irradiation into a 3D map of the treatment dose distribution.

3.2 Polymer Gel Chemistry

This section provides a detailed overview of polymer gel chemistry. Section 3.2.1 describes the chemical reactions responsible for the initiation, propagation and termination of polymer molecules. This is followed by a description of the resulting formed polymer is section 3.2.2.

3.2.1 Reaction Mechansims

When polymer gels are exposed to ionizing radiation, water molecules in the gel undergo radiolysis [43] to produce highly-reactive primary radicals (R•) according to equation 3.1.

$$H_20 \longrightarrow 2R\bullet \tag{3.1}$$

Primary radicals initiate polymerization by reacting with monomer molecules (M) to produce monomer radicals ($M\bullet$), as described in equation 3.2.

$$R\bullet + M \longrightarrow M\bullet \tag{3.2}$$

This is followed by addition of successive monomer molecules through chain propagation, described in equation 3.3, to produce polymer chains. Each addition creates a new radical molecule that is larger by one monomer unit [100].

$$M\bullet + M \longrightarrow M_{n+1}\bullet \tag{3.3}$$

Additional propagation reactions can result if a crosslinking monomer, most commonly BIS, is included in the gel formulation. These molecules contain two vinyl groups (i.e. two $CH = CH_2$ molecular bonds) that can partake in propagation of polymerization. One vinyl group participates in chain propagation according to equation 3.3, while the other becomes a pendant vinyl group that can form a crosslink joining one polymer chain to another. Alternatively, the pendant group can form

a loop with the radical generated during chain propagation via primary cyclization [43, 101], resulting in fewer pendant vinyl groups available for crosslinking and a less dense polymer. However, if the vinyl group that participated in chain propagation has been rendered neutral by a termination reaction (see below), the remaining pendant group can react with a primary radical to initiate further polymerization reactions [43] as described in equation 3.4.

$$R\bullet + M_n \longrightarrow M_n\bullet \tag{3.4}$$

Polymer molecules continue to grow until the polymer radical is terminated through chain transfer reactions or bimolecular termination. Chain transfer occurs when a polymer molecule transfers its radical centre to another molecule according to equation 3.5, rendering it neutral and incapable of further growth.

$$M_m\bullet + M_n \longrightarrow M_m + M_n\bullet \tag{3.5}$$

The radical centre may be transferred to another monomer molecule, resulting in possible further polymerization, or to a gelatin molecule. As propagation reactions between gelatin and additional monomer molecules occur slowly [43], chain transfer to gelatin is assumed to terminate polymer growth [101]. During bimolecular termination, two radicals combine to render both neutral molecules. This occurs through combination, disproportionation, or recombination with primary radicals [43], according to equations 3.6 - 3.8, respectively.

$$M_m\bullet + M_n\bullet \longrightarrow M_{m+n} \tag{3.6}$$

$$M_m\bullet + M_n\bullet \longrightarrow M_m + M_n \tag{3.7}$$

$$R\bullet + M_n\bullet \longrightarrow M_n \tag{3.8}$$

In addition to chain transfer reactions and bimolecular termination, peroxide radicals can form if oxygen is present in the gel and quickly lead to termination of both primary radicals as well as growing polymer chains [43]. For this reason, oxygen inhibition is an important consideration in PGD.

3.2.2 Properties of the Formed Polymer

The properties of the polymer formed in a gel dosimeter, including the amount and architecture of the polymer, will depend on the monomers used in the gel formulation and their relative concentrations. In most PGD studies, the resulting polymer is constructed from a non-crosslinking or linear monomer, such as acrylamide, and the crosslinking monomer BIS. The relative concentrations of these components are traditionally described using the total fraction of monomer (%T) and fraction of monomer that is crosslinker (%C) in the gel system. Equations 3.9 and 3.10 define %T and %C, respectively:

$$\%T = (\frac{m_l + m_c}{m_T})100\% \tag{3.9}$$

$$\%C = (\frac{m_c}{m_c + m_l})100\% \tag{3.10}$$

where m_l is the initial mass of the linear monomer, m_c is the initial mass of the crosslinking monomer, and m_T is the total mass of the gel. For a given radiation dose, increasing %T while keeping %C fixed typically increases the polymerization rate as more monomer is available to react in the gel system. This leads to an increase in the amount of linear polymer formed per unit dose and an increase in dose sensitivity of the gel [102, 103]. Similarly, increasing %C while keeping %T constant results in an increase in gel radiation sensitivity up to the solubility limit of BIS at room temperature, followed by a decrease in sensitivity beyond the BIS solubility threshold [103]. The structure of the resulting polymer is also affected by varying %T and %C [72]. For a given radiation dose, polymers composed solely of non-crosslinking monomers (i.e. 0 %C) form linear polymer chains with no crosslinks. As the fraction of crosslinker in the gel increases, the polymer structure progresses from linear chains to an ordered network. When the polymer consists solely of crosslinking monomer, a highy-crosslinked network results, consisting of several knots and beads [72].

3.3 Imaging Modalities

A number of imaging modalities have been investigated for use in PGD studies, including MRI, OptCT, CT, US and Raman spectroscopy. However, MRI, OptCT and CT are the most commonly used readout techniques and have also remained active areas of study in the PGD literature. An overview of the properties that can be probed by MRI, OptCT and CT for dose readout in PGD is provided below.

3.3.1 Magnetic Resonance Imaging

Traditionally, MRI has been the most widely used imaging modality for dose read-out in PGD. Using this technique, differences between the relaxation rate ($R_2 = \frac{1}{T_2}$) of protons in the radiation-induced polymer and remaining unreacted gel components provide contrast in MR images [43, 69, 104]. To understand the mechanisms responsible for image constrast, the gel can be assumed to consist of 3 proton pools: the mobile pool, containing protons from water and unreacted monomers, the polymer pool, and the gelatin pool [105]. In the regime of fast exchange, the different proton pools are characterized by different relaxation rates. Initially, all the monomer and water molecules exist in the mobile pool as their mobility is relatively high and their magnetization vectors return to equilibrium slowly (i.e. they have a long T_2 and small R_2). After exposure to radiation, these molecules are incorporated into polymer molecules and the polymer pool increases. Polymer molecules are far less mobile than monomer and water molecules and have a short T_2, or by extension, large R_2. The increase in R_2 is proportional to the amount of polymer formed, which depends on the absorbed radiation dose [43, 104].

In a typical PGD study using MRI, a collection of T_2-weighted images are used to generate quantitative maps of R_2 using one of several available imaging protocols [43, 69, 104]. While many protocols have been investigated, including single and multiple spin-echo sequences [104], turbo imaging [106] and magnetization transfer [107], spin-echo sequences are common in MRI PGD studies as they are readily available on all MRI scanners [108]. Using a spin-echo protocol, an initial pulse excites the spins in each proton pool and images are acquired at different echo times after excitation as the spins return to their equilibrium state. The pixel intensity for each voxel is then plotted as a function of the echo time. For single spin-echo imaging, R_2 for a given voxel can be determined from the slope of the intensity vs. time curve, while for multiple spin-echo imaging, R_2 for a given voxel is determined by fitting an exponential decay curve to the signal vs. time data [43, 104, 108].

While MRI provides a non-invasive dose readout method for PGD, this technique suffers from several inherent limitations, including susceptibility to imaging artifacts and a pronounced sensitivity to gel temperature [108]. These limitations, together with the limited accessibility and cost associated with MRI scanners, has shifted the focus of PGD research to other imaging modalities [108].

3.3.2 Optical Computed Tomography

An attractive alternative to MRI and CT, OptCT is an inexpensive method of dose read-out that has the potential for many clinical applications [43, 79, 81]. It is based on the change in visible opacity produced in the gel upon exposure to radiation (see figure 1.9) [43, 79]. Prior to dose delivery, the gel is virtually transparent to optical photons [43]. However, following irradiation, polymer molecules in the gel cause optical photons to scatter, resulting in reduced transmission through the gel at the location of the polymer. The reduction in light transmission is proportional to the amount of polymer formed, which is in turn proportional to the absorbed radiation dose [43, 79].

In a typical PGD study using OptCT, several optical projections are obtained using either a laser scanned across the gel and a photodiode detector [43, 79, 81, 109–112] or a parallel or cone beam light source and a pixelated area detector [113–118]. Using either configuration, the intensity of transmitted light photons, I_t, is related to the intensity of the incident beam, I_0, using Beer's law [43, 113]:

$$I_t = I_0 e^{-\mu_{opt} x} \tag{3.11}$$

where μ_{opt} and x are the optical attenuation coefficient and thickness of the object the beam travels through, respectively. The μ_{opt} is a quantity analogous to the x-ray linear attenuation coefficient, μ, described in section 2.3.1 and is determined for each pixel in the resulting images using filtered back-projection [43, 113].

Since its initial introduction into PGD, OptCT has been investigated by several authors [43, 113] and shows great promise for 3D dosimetry, with two systems already available commercially. However, as already mentioned, optical contrast in polymer gels is mainly produced from scattered light [43, 80], making OptCT prone to image noise and several imaging artefacts, particularly from reflection and refraction of light at the dosimeter walls [43]. For this reason, OptCT may be better suited for read-out with absorbing dosimeters, such as Presage (described in section 1.3.3), where these types of artifacts can be avoided [40].

3.3.3 X-Ray Computed Tomography

In addition to MRI and OptCT, dose information can be extracted from polymer gels using CT [84]. This technique is based on the mass density changes that occur in

the gel when exposed to radiation [102, 119, 120]. As the radiation dose increases, more monomer is converted to polymer, resulting in an increase in gel density at the location of dose deposition. The change in gel density, $\Delta\rho_{gel}$, can be understood using the model developed by Hilts *et al.* described in equation 3.12:

$$\Delta\rho_{gel} = \%T_{0Gy}(1 - f_m)\Delta\rho_{polymer} \tag{3.12}$$

where $\%T_{0Gy}$ is the total fraction of monomer in unirradiated gel, f_m is the monomer fraction remaining after exposure to a given dose and $\Delta\rho_{polymer}$ is the density change that results per weight fraction of monomer converted to polymer [102]. The result of the density change produced by polymer formation is an increase in the linear attenuation coefficient of the gel [121]. Since a CT image can be considered a map of linear attenuation coefficients, expressed as N_{CT} (equation 2.8), measuring the difference in N_{CT} between irradiated and unirradiated (ΔN_{CT}) gel provides a measure of the absorbed radiation dose [121].

For many polymer gel formulations, the magnitude of the radiation-induced density change is small (e.g. $\frac{1mg}{cm^3}$ per Gy [119]), resulting in a ΔN_{CT} on the order of 1 H/Gy [43]. For this reason, gel images acquired for a typical PGD study using CT must be highly optimized for low noise to obtain useful dose information. This is achieved using a carefully designed CT scanning protocol and image post-processing techniques. An ideal scanning protocol includes imaging parameters, such as the pixel dimension, slice thickness, and x-ray tube current and voltage, that minimize the noise in the resulting gel images [122]. Typically, upwards of 25 images are acquired using the protocol at each slice location in the irradiated gel and also in an inactive *blank* gel. This procedure allows further reduction in image noise through image averaging and the removal of image artifacts using background subtraction [84]. Following these initial post-processing techniques, image noise is further reduced by applying image filters [123–126] and the ΔN_{CT} between irradiated and unirradiated gel is computed.

As mentioned above, while CT provides an easy to use tool for extracting dose information that is readily available in virtually every RT clinic, the low radiation sensitivity (i.e. small density change) of the technique has prevented wide-spread adoption of CT for PGD. However, recent investigations into new PGD formulations [44, 127–129] have resulted in the introduction of a new PGD recipe with enhanced radiation sensitivity [44]. This formulation shows great promise for use in CT PGD

[130] and is focus of the present work.

3.4 Performance of Dose Measurement

The performance of a PGD system is evaluated by assessing the accuracy and precision with which it is capable of measuring dose. Many factors can affect the accuracy and precision associated with polymer gel dose measurements and their influence on the resulting performance of the PGD system must be considered. This section discusses accuracy and precision in PGD in section 3.4.1 and provides details on the factors that can affect performance in section 3.4.2.

3.4.1 Accuracy & Precision

Accuracy in PGD can be defined as the degree of conformity of a gel dose map to the true dose distribution and must be evaluated in terms of dose and space [131]. This introduces challenges in determining the overall accuracy of a PGD study as no gold standard 3D dosimeter exists to provide measures of the actual radiation delivered. In addition, as with all radiation treatments, the spatial and dosimetric dimensions are interrelated and it is theoretically impossible to extract both dosimetric and spatial errors [43, 131]. For this reason, spatial and dosimetric accuracy are typically assessed by comparing PGD measurements to those obtained by another well-characterized dosimetry system, such as an ionization chamber or film.

Precision in PGD can be defined as the ability of a polymer gel and its associated readout technique to generate dose maps that can be consistently reproduced within a given tolerance or level of uncertainty [88]. Similar to accuracy in PGD, assessing the overall precision of a polymer gel system presents challenges as this would require the reproducibility of multiple 3D dosimetry experiments to be determined. Unfortunately, the extensive number of dose distributions associated with even a single treatment site in RT render such a reproducibility study unfeasible [43, 88]. For this reason, a metric known as the dose resolution was introduced by Baldock *et al.* [132] to assess the overall dosimetric precision of a given PGD system. The dose resolution, D^p_Δ, is defined as the minimum difference in dose that can be detected within a given level of confidence, p, using equation 3.13:

$$D^p_\Delta = k_p\sqrt{2}\sigma_D \tag{3.13}$$

where k_p is the coverage factor for confidence interval p and σ_D is the uncertainty in dose measurement. For a 95% confidence interval, $k_{95\%} = 1.96$ and $D_\Delta^{95\%} = 2.77\sigma_D$ for the PGD system being evaluated [132]. The σ_D is computed using the slope of the dose response curve of the gel system (commonly referred to as the dose sensitivity) and the noise in the resulting images. For example, using CT PGD, D_Δ^p is computed using equation 3.14:

$$D_\Delta^p = k_p\sqrt{2}(\frac{\delta N_{CT}}{\delta D})^{-1}\sigma_{N_{CT}} \tag{3.14}$$

where $\frac{\delta N_{CT}}{\delta D}$ is the slope of the dose response and $\sigma_{N_{CT}}$ is the noise measured in CT images of the gel [123].

3.4.2 Factors Affecting Performance

Several factors can affect the performance of a PGD system by influencing the spatial and dosimetric accuracy and precision of the resulting dose measurements. For this reason, these factors must be carefully considered or accounted for when performing a PGD study to ensure reliable dose measurements. Table 3.1 summarizes the factors affecting performance at each stage of the PGD process [43, 131, 133].

During fabrication, the gel recipe itself will determine the dose sensitivity of the gel and influence the overall dosimetric precision achievable. However, for all compositions, variations in the concentrations of the chemical components of the gel can lead to differences in dose response between calibration and test phantoms or between studies using different batches of gel. These differences impact both the precision and accuracy associated with a PGD study. Similarly, variations in temperature, during both manufacture and storage, can cause differences in dose response that affect accuracy and precision. Temperature variations can lead to an inconsistent dose response throughout a single dosimeter or between different batches of gel, while differences in temperature between calibration and test phantoms can introduce systematic errors in the resulting 3D dose maps. The gel may also experience volumetric contraction as it becomes solid, leading to physical deformation of the dosimeter and inaccurate dose readings [43, 131]. Fortunately, most of these errors can be accounted for by using a consistent fabrication procedure between studies, using the same batch of gel for both the calibration and test phantoms and maintaining a consistent temperature history between the phantoms after manufacture. It is important to note keeping phantom temperatures consistent may prove difficult if the phantoms are different dimensions [88].

	Spatial and Dosimetric Accuracy and Precision
Fabrication	Variations in chemical concentrations
	Variations in fabrication temperature
	Differences between calibration and test phantoms
	Volumetric contraction during gelling
	Dose sensitivity of the gel formulation
Irradiation	Chemical and spatial instabilities
	Variations in irradiation temperature
	Volumetric contraction during polymerization
	Stochastic variations in delivered dose
	Errors in calibration phantom positioning
	Errors in test phantom positioning
	Dose rate, energy or temperature dependent response
	Tissue equivalence
	Recipient wall effects
Imaging	Temperature during scanning
	Imaging artifacts
	Stochastic noise
	Voxel dimensions

Table 3.1: Factors influencing the spatial and dosimetric accuracy and precision of PGD measurements.

Several factors are also present during irradiation of a gel dosimeter that can affect the overall performance of a PGD system. Incorrect positioning of either the calibration or test phantoms can result in inaccurate dose readings and a lack of reproducibility between studies. Similarly, stochastic variations in the dose produced by a radiation delivery device can decrease the overall precision of a PGD system. Additionally, a gel response that is dependent on dose rate or energy can introduce variations in dose response that lead to inaccurate dose readings, while temperature dependencies can lead to challenges in maintaining a high degree of both accuracy and precision [43, 131]. Temperature is especially important when calibration and test phantoms have different dimensions, as the heat released during polymerization will differ for phantoms of different size, leading to errors in dose measurement [89].

Following radiation delivery, if the gel is not allowed enough time for the polymerization reactions to stabilize, inconsistent dose readings between calibration and test phantoms may result, while for some gels, if polymerization continues for too long, monomer diffusion can lead to a decrease in the spatial integrity of the dose distribution. A volumetric contraction of the gel due to polymer formation may also lead to a decrease in the spatial accuracy of the system. Further performance issues may occur if the gel does not possess a tissue equivalent response or if recipient wall effects are present, where traces of oxygen adhere to or leak through the wall of the gel container and interrupt polymer formation [43, 131]. This highlights the importance of storing polymer gels in oxygen impermeable containers even if they contain THPC, as additional oxygen may exhaust the scavenging abilities of the antioxidant.

In addition to the factors present during fabrication and irradiation, a number of considerations must be made during imaging of a gel dosimeter to ensure a high level of performance for the system. Depending on the imaging modality employed, the temperature of the gel may influence the properties that can be probed to provide image contrast. Temperature differences within a single gel or between calibration and test phantoms may lead to inconsistent measurements and erroneous dose readings. This is particularly important in MRI imaging as temperature fluctuations in the gel can alter the value of the proton spin relaxation rates measured. In addition to temperature, the size of the voxels (pixel dimensions and slice thickness) chosen for a given study will determine the spatial resolution of the resulting images and impact the overall precision that can be achieved by the PGD system. Further factors present during imaging include stochastic image noise, which can impact the reproducibility of the PGD system, and image artifacts, which can lead to incorrect dose measurements.

3.5 Applications

Polymer gel dosimeters are an attractive dose verification tool for many clinical applications due to their ability to measure absorbed dose in 3D. However, the time required to perform a PGD study and the cost associated with each experiment is large compared to other dosimetry techniques. For this reason, PGD is considered to be best suited for benchmarking the performance of new treatment techniques and evaluating end-to-end processes to ensure correct patient positioning and dose delivery. Nevertheless, a large number of studies have reported on the use of prototype PGD systems for a variety of clinical applications [43]. Most reports focus on validating the performance of a PGD system for use with a particular application as opposed to using the system to verify a specific patient treatment.

For the majority of work examining PGD for clinical applications, MRI has been used to extract dose information from irradiated gels. Early investigations used PAG dosimeters with MRI to examine dose distributions for 3DCRT [134, 135] and IMRT [136, 137] and illustrated the potential of PGD for modern RT treatments. However, it was soon discovered that PGD experiments performed with PAG and MRI can suffer from large dose inaccuracies attributed to oxygen contamination, MRI artifacts [135] and chemical instabilities [71]. Despite these challenges, further work was performed using anoxic gels and MRI to examine a vast number of clinical applications with varying degrees of success, including 3DCRT [138, 139], IMRT [140–142], IMAT [143–145], SRS [146–153] and brachytherapy [154, 155]. More recent studies using MRI with normoxic gels for IMRT [156], IGRT [157] and VMAT [158] illustrate this new class of gels show promise for use with MRI for complex RT treatment verification. Nevertheless, work to determine ways to improve PGD using MRI continues to be an active area of research in the PGD literature [159].

With the introduction of new dose read-out techniques, it is possible that PGD will become a common verification tool for complex RT treatments in the near future. Recent work using normoxic gels with OptCT read-out illustrate these systems can be used to evaluate IMRT distributions [160] and small field dosimetry [161]. In addition, early investigations using CT PGD exhibit the potential of this technique for SRS verification [162] as well as diagnostic dosimetry [163]. Moreover, a significant development was recently made using CT and the new gel formulation investigated in this dissertation for head and neck IMRT treatment verification. This work is described in chapter 5. For details on additional studies that report on the use of

polymer gels for RT applications, the reader is referred to a recent review article on PGD [43] and the proceedings of the IC3DDose conferences.

Chapter 4

Materials & Methods

This chapter describes the general materials and methods used throughout this work. The fabrication procedure used to manufacture and store gel dosimeters is summarized in section 4.1. Section 4.2 provides a description of the head and neck phantom used to position 1 L gels during CT imaging and radiation delivery. Further details on the equipment and procedures used to irradiate and image polymer gels are provided in sections 4.3 and 4.4, respectively. The final part of this chapter provides a summary of the image processing and data analysis techniques employed throughout this work in section 4.5. Experimental procedures specific to each individual study are described in the results and discussion provided in chapters 5 - 7.

4.1 Gel Fabrication

4.1.1 Manufacture

All polymer gels contained, by weight, 75.5% deionized water, 5% gelatin (Sigma-Aldrich Canada, Oakville, ON), 15% NIPAM (TCI America, Portland, OR), 4.5% BIS (Sigma-Aldrich) and 5 mM THPC (Sigma-Aldrich) as an antioxidant unless otherwise noted. Each gel was manufactured under normal atmospheric conditions using a procedure consistent to all experiments. To begin the fabrication process, the deionized water and dry chemicals were measured using a high-precision scale (Denver Instrument, Denver, CO). The deionized water was then poured into a beaker that was used to house the gel solution throughout the manufacturing procedure and transferred to a laboratory mixer (Torrey Pines Scientific, San Marcos, CA) in the fume hood. The mixer is equipped with a hot plate and thermometer that main-

tains the gel temperature at each user-defined value as well as an integrated magnetic stirrer for continuous stirring of the gel solution. After being placed on the mixer, the water was stirred continuously as the gelatin was added to the beaker and the solution was heated to a temperature of 40°C. Once the gelatin had fully dissolved, the solution was cooled to 34°C and the NIPAM was added. The solution was held at 34°C and stirred continuously until the NIPAM had dissolved. At this stage, the BIS was added and the solution was continuously stirred until the BIS had fully dissolved before lowering the temperature of the solution to 30°C. The THPC was then added using either a syringe or micropipette (Gilson, Middleton, WI & Wheaton Scientific, Millville, NJ) and stirred for at least one minute before transferring the solution to the chosen recipient vessel [44]. When utilized, additional blank gels were manufactured with the same procedure using 5% gelatin, 0.5% NIPAM and 0.5% BIS (no THPC). Small amounts of NIPAM and BIS are added to these gels to prevent mould growth.

(a) (b)

Figure 4.1: (a) The 20 mL scintillation vials and their associated acrylic pots used to house completed gel solutions for all gel vial studies. (b) High-density polyethylene terephthalate jars used to house polymer gels for all 1 L gel studies.

4.1.2 Storage

For all experiments, the completed gel solution was transferred to 20 mL liquid scintillation vials (Wheaton) or poured into transparent 1 L jars (Modus Medical Devices, London, ON). The scintillation vials are cylindrical tubes with 1 mm thick walls composed of polyethylene plastic. This material is permeable to oxygen which may lead to inhibition of the polymerization reactions if the oxygen scavenging ability of

the THPC in the gel is exhausted. For this reason, each vial was individually sealed in a pot with 2.5 cm thick acrylic walls to prevent oxygen from contaminating the gel [102]. The 1L jars are also cylindrical tubes composed of $\sim$ 1 mm thick, high-density polyethylene terephthalate walls that are highly oxygen impermeable and do not require an additional oxygen barrier. Figure 4.1 illustrates the gel vials and their associated acrylic pots as well as the jars used to house 1L gels.

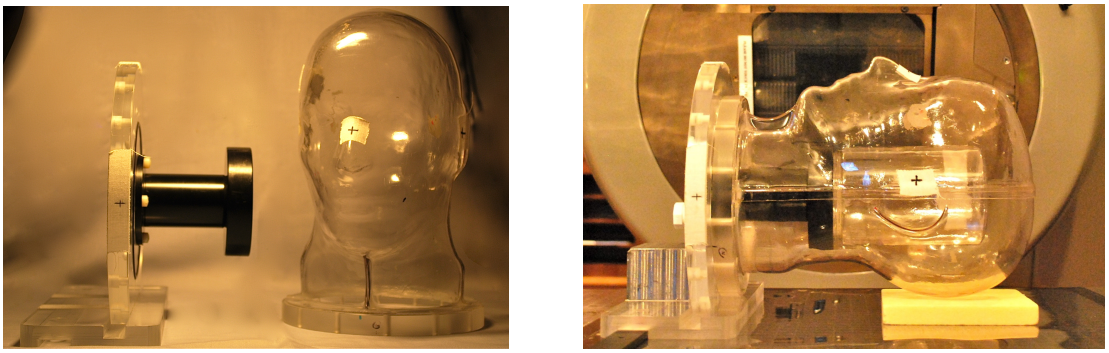

(a) (b)

Figure 4.2: The head and neck phantom used to irradiate and image all 1 L gels. (a) The phantom consists of a removable perspex head that can be fastened to an acrylic base plate and a support arm to secure a 1L cylinder within the phantom. (b) The phantom at the treatment unit with the head in place and filled with water. *Reproduced with permission* [130].

After transferring the gel solution to the chosen recipient, all gels were wrapped in aluminum foil to prevent photo-initiated polymerization and refrigerated until solid. As mentioned in section 3.1.2, the cooling rate of polymer gels can affect their resulting dose response, and as such, efforts were made to cool each gel at a uniform rate. For the gel vials, the acrylic pots were used to reduce the temperature gradient between the air in the refrigerator and the gel inside each vial. For the 1L gels, a water bath was used to mediate temperature gradients. Gel vials were refrigerated in their acrylic pots for at least one hour until solid while all 1 L gels were refrigerated in a water bath for at least 6 hours until solid.

4.2 Head and Neck Phantom

A customized head and neck phantom, illustrated in figure 4.2, was used for irradiation and imaging of all 1 L gels used in this work [130]. The phantom is designed to provide

low CT image noise and artefacts as well as accurate and reproducible localization throughout the 3D dosimetry process. It consists of a removable, 1 mm thick perspex head that can be fastened to an acrylic base plate using plastic screws and a precision machined support arm that secures the 1 L cylinder within the phantom. Once screwed in place, the phantom head is water tight and the phantom can be filled with water for irradiation. The phantom is also designed to allow removal of the head while accurately maintaining gel position, a feature required to optimally reduce image noise during CT read-out [164]. Finally, the phantom can be reproducibly positioned on the CT and treatment unit couches to within 1.5 mm using a locking bar or clinical mask immobilization system [164, 165]. For all 1 L experiments in this work, the phantom was secured to the CT and LINAC couches using a locking bar and positioned with respect to the room coordinate system by aligning crosshairs marked on the top and side of the phantom with the room lasers.

4.3 Gel Irradiation

4.3.1 Linear Accelerators

All gels were irradiated using photons generated by a Varian Clinac 21EX or Truebeam LINAC (Varian Medical Systems, Palo Alto, CA). Figure 4.3 provides a schematic diagram illustrating the main components of a typical LINAC, including a modulator cabinet, microwave power source, electron gun, accelerating waveguide, bending magnet assembly and treatment head housing the x-ray target and beam collimation and filtering devices. Under normal operation, the modulator cabinet delivers a high voltage pulse to the electron gun and microwave power source simultaneously. This triggers the electron gun to emit pulses of electrons at the same instant the microwave power source produces pulses of microwaves, which both enter the accelerating waveguide at the same instant. The waveguide consists of an evacuated copper tube divided into sections by copper disks. As the microwaves propagate though the waveguide, they transfer energy to the electrons, causing the electrons to accelerate to high speeds. The resulting narrow pencil beam of electrons then exits the waveguide and is directed to the treatment head by the bending magnet assembly [9, 166].

The electron beam enters the treatment head and strikes the x-ray target, producing x-ray photons through bremsstrahlung production. The resulting x-ray beam then passes through the fixed primary collimator and continues to the beam filter-

ing carousel. In the Clinac 21 EX machine, the carrousel contains a flattening filter, usually composed of a lead [9], that creates a uniform beam intensity across the treatment field. The Truebeam LINAC model represents a major design upgrade from the Clinac series in that it is capable of delivering both flattening filtered and flattening filter-free x-ray beams. However, for all irradiations in this work, the Truebeam was operated with the flattening filter in place, making the two machines virtually interchangeable. After being filtered, the beam passes through a pair of monitor ion chambers that provide dose information to the LINAC control console and the adjustable secondary collimators that provide rectangular field shaping. At this stage, the beam can be used for treatment but is often collimated further using the MLC, described in section 1.1.1, before reaching the patient [9, 166].

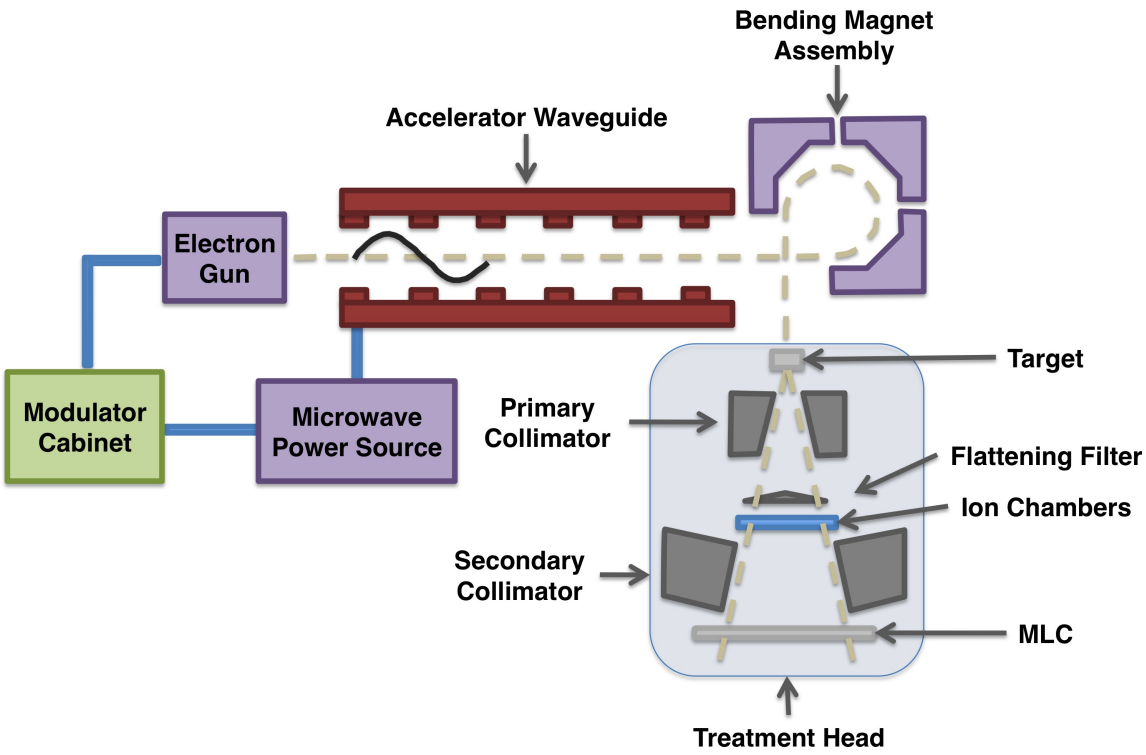

Figure 4.3: Schematic diagram illustrating the main components of a typical LINAC, including a modulator cabinet, microwave power source, electron gun, accelerating waveguide, bending magnet assembly and treatment head housing the x-ray target and beam collimation and filtering devices.

4.3.2 Irradiation Techniques

All polymer gels used in this work were irradiated with 6 MV photons at a machine dose rate of 400 MU/min unless otherwise noted. For the gel vial studies, each vial was irradiated individually within its acrylic pot using the phantom illustrated in figure 4.4 [102]. The phantom consists of a 20 x 20 x 20 cm^3 acrylic cube with a precision machined cylindrical cavity for inserting each gel within its acrylic pot at its centre. The design ensures no air gaps exist between the walls of the pot and cavity and places the centre of each vial at 10 cm depth within the phantom for beam entry at 90° angles. Reproducible positioning is achieved at CT planning and radiation delivery using lines engraved on the top and side walls of the phantom. Further details on the protocols used to irradiate vials in the acrylic cube are provided in the experimental details sections of the results and discussion chapters.

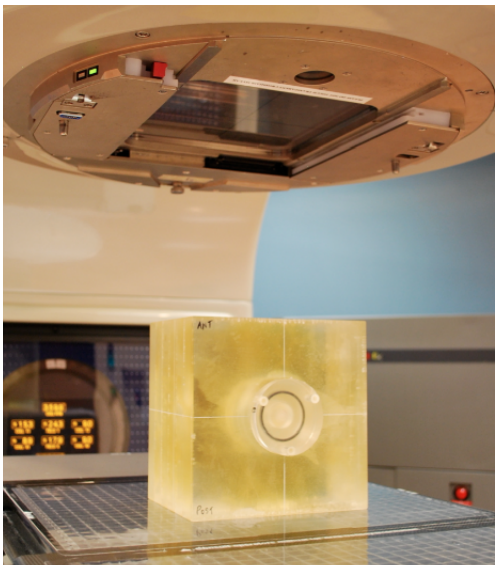

Figure 4.4: The acrylic cube used to irradiate gel vials positioned at the treatment unit. An acrylic pot housing a gel vial is inserted at the centre of the phantom.

For the 1 L gel experiments, the head and neck phantom described in section 4.2 was used to position gels at planning CT and radiation delivery using a locking bar. A simple treatment plan, consisting of three intersecting 3 x 3 cm^2 fields, was used to irradiate all 1 L gels unless otherwise indicated [130]. The plan was designed using the Eclipse treatment planning system (Varian) running version 10.0 of the analytical anisotropic algorithm and a planning CT scan of a blank gel secured in the head and neck phantom with the head in place and filled with water. Figure 4.5a shows the

beam arrangement used for the plan, which was designed to produce a full range of doses that could be accurately predicted by the TPS and used to generate dose response curves. The maximum prescription dose was 26 Gy unless otherwise noted, resulting in the planned dose distribution illustrated in figure 4.5b. The expected accuracy of the dose calculation for this simple plan is better than 2% based on the TPS commissioning data. Additional details on the irradiation procedures specific to each 1 L gel experiment are provided in the following results and discussion chapters.

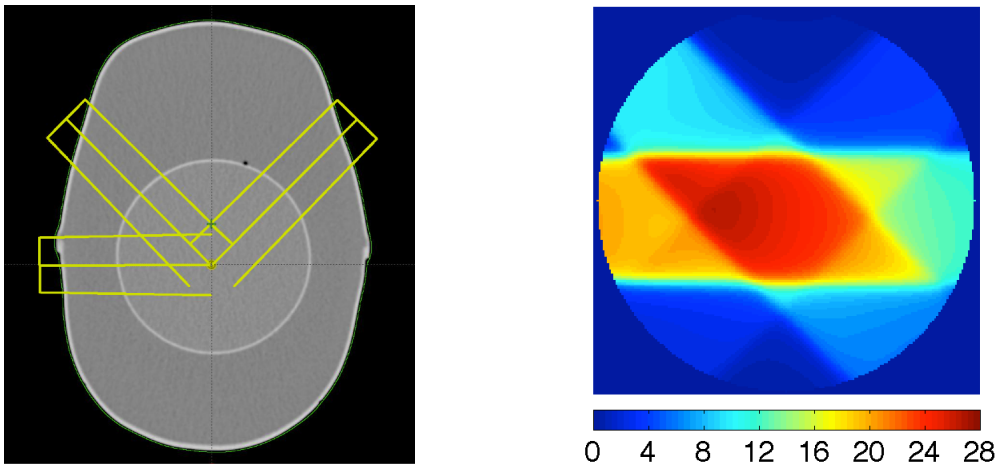

(a) (b)

Figure 4.5: (a) Beam arrangement and (b) TPS computed dose distribution (colour bar in Gy) used to irradiate 1 L gels to produce dose response curves. *Reproduced with permission* [130].

4.4 Gel Imaging

4.4.1 Computed Tomography Scanners

All gel imaging was performed using GE HiSpeed FX/i and Optima CT580 CT scanners (GE Medical Systems, Milwaukee, WI). Both machines are 3rd generation CT systems (described in section 2.2) that employ a rotate-rotate geometry in which an x-ray tube is fixed to a rotating gantry opposite an arc of x-ray detectors. The x-ray tubes in both scanners contain a rotating anode composed of a tungsten-rhenium focal track on a molybdenum alloy substrate that is backed by graphite. Each scanner is also equipped with over 800 HiLight x-ray detectors. HiLight is a proprietary solid

Parameter	HiSpeed Fx/i	Optima CT580
Tube voltage (kV)	80, 120, 140	80, 100, 120, 140
Tube current (mA)	60, 80, 100, 130, 150, 200, 250, 300	10 - 800 in 5 mA increments
Gantry rotation time (s)	0.7, 1, 1.5, 2, 3	0.5, 0.6, 0.7, 0.8, 0.9, 1, 2, 3, 4
Slice thickness (mm)	1, 2, 3, 5, 7, 10	0.625, 1.25, 2.5, 3.75, 5, 7.5, 10
Field of view (cm^2)	18 x 18, 25 x 25, 50 x 50	25 x 25, 50 x 50
Reconstruction Algorithm	Soft, Standard, Standard Plus, Detail, Chest, Bone, Edge	Soft, Standard, Lung, Chest, Detail, Bone, Edge, Edge Plus

Table 4.1: Imaging parameters available in axial acquisition mode on the HiSpeed Fx/i and Optima CT580 CT scanners used throughout this work.

state scintillator material developed by GE specifically for CT imaging and offers 99% photon absorption efficiency.

The HiSpeed Fx/i machine is a single slice CT system equipped with one row of 20 mm wide detector elements along the z-axis of the scanner (see figure 2.6a). It is capable of acquiring up to 10 mm of patient data in a single slice at each couch position and slice thickness is adjusted using the x-ray beam collimator. A significant technological upgrade from the HiSpeed design, the Optima CT580 is a multislice machine that can image up to 20 mm of patient anatomy at each couch location using 24 rows of detector elements in the z-plane of the scanner (see figure 2.6b). The inner 16 rows are 0.625 mm wide while the outer 4 rows located on either side of the detector are 1.25 mm wide along the z-plane. Unlike the HiSpeed Fx/i, slice thickness is determined by the detector configuration and the collimator adjusts the x-ray beam to correspond to the active area of the detectors. The signals from each row can be used individually or combined to adjust the slice thickness for up to 16 image slices. For example, the inner 16 rows can be used to produce 16 images with 0.625 mm thickness or combined to produce 8 images with 1.25 mm slice thickness.

4.4.2 Imaging Techniques

All CT imaging was performed using custom-built phantoms designed for low CT image noise and artefacts. The phantoms served to support each vial or 1L cylinder within the scanner bore and allowed reproducible positioning of each sample with respect to the CT room coordinate system. Following phantom positioning, a scanner warmup sequence was performed for all scanning sessions to minimize variations in

x-ray tube temperature resulting from increasing tube load [84]. Images were then acquired using axial mode of acquisition unless otherwise indicated. A scanning protocol was defined from the available imaging parameters on each scanner summarized in table 4.1. Additional background images were also collected using the same imaging protocol to enable a background subtraction to be performed during data processing.

For all vial experiments, CT images were acquired using the custom-built phantom shown in figure 4.6a. The phantom consists of a styrofoam block with 10 cylindrical cavities, or cradles, hollowed out for inserting the vials and positioning them symmetrically in a circle within the scanner bore. The design has been shown to provide superior noise reduction in CT images over water equivalent plastic or acrylic phantoms [122]. For each experiment, the phantom was placed on the CT couch and cross-hairs marked on the lateral and coronal walls of the phantom were aligned to the CT room lasers. Images were then acquired through the centre of the vials using an imaging protocol and procedure specific to each vial study. These details can be found in the results and discussion chapters that follow. Procedures used to reduce image noise and remove imaging artefacts are provided below.

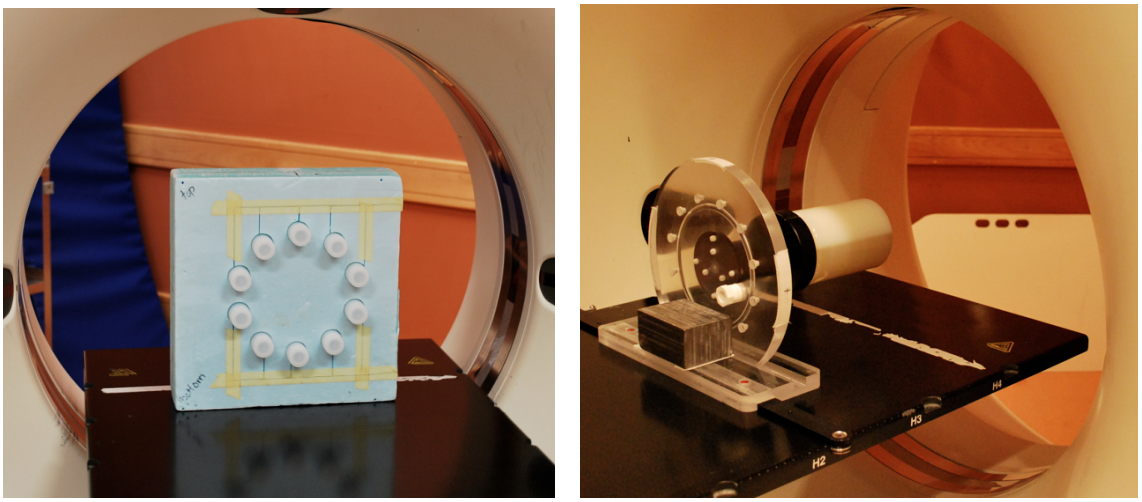

(a) (b)

Figure 4.6: (a) The custom built styrofoam phantom used to image all gel vials. (b) The head and neck phantom at CT imaging. The head is removed to minimizes image noise and artifacts in the resulting gel images.

Imaging of all 1 L cylinders was performed using the head and neck phantom described in section 4.2. The phantom was secured to the CT couch using a locking bar and positioned as at planning CT by aligning the phantom crosshairs with the CT

room lasers. Images of the gel were then acquired with the head removed as shown in figure 4.6b. Preliminary experiments indicate this procedure minimizes image noise and artifacts during gel CT readout [164]. The imaging parameters chosen for each gel study were selected to produce low image noise while avoiding excessive tube load and CT dose that can result from using a high number of image averages [167]. Details on the parameters specific to each study are reported in the experimental details sections of the following results and discussion chapters.

4.5 Treatment of Data

4.5.1 Image Processing

For all experiments in this work, image processing was performed using version R2010b of Matlab (The Mathworks, Natick, MA) and made use of the functions available in the image processing toolbox. Each stage of imaging processing is illustrated in figure 4.7 using the 3-field calibration dose distribution. A single, unprocessed, image through the isocentre of the distribution is shown in figure 4.7a. Processing began by averaging the images at each slice position for all CT scans to reduce the overall image noise [84, 122]. The averaged background images were then subtracted from the averaged gel or test images to remove image artifacts [84]. An averaged, background subtracted image through the isocentre of the calibration distribution is shown in figure 4.7b. This was followed by image filtering using an adaptive mean (AM) filter to further reduce stochastic noise present in gel CT images after image averaging. The AM filter adapts its response to local noise statistics and provides improved signal preservation over a standard mean filter [123]. For each image pixel, g(x,y), the AM filter computes the mean, m_L, and variance, σ_L^2, of the surrounding pixel values in an m-by-n neighbourhood as well as the overall noise, σ_N^2, in the image. It then adjusts the value of the pixel in question using the ratio of the local variance to the overall image variance using equation 4.1:

$$f(x,y) = g(x,y) - \frac{\sigma_N^2}{\sigma_L^2}[g(x,y) - m_L] \tag{4.1}$$

where f(x,y) is the new, filtered pixel value. For all gels in this work, the AM filter was applied once using a 3 x 3 pixel neighbourhood. Note that less AM filtering is used than is recommended in previous gel CT work [124] due to the introduction of

a second filtering step described below.

Following AM filtering, images were filtered a second time using a new remnant artifact removal (RAR) technique [126]. The RAR filter is designed to remove ring and streak artefacts that remain after AM filtering as well as structured noise due to inherent gel density fluctuations. For a given 2D window (or span) chosen by the operator, the filter applies a user-defined n^{th} degree polynomial fit to the pixel values within the window boundaries. All pixels with values above the fit result are assumed to be signal and are assigned the value of the polynomial at the particular pixel location. The process is then repeated for a user-specified number of iterations. For all studies in this work, RAR parameters were chosen based on recommendations given by Jirasek *et al.* [126] and are provided in each experimental details section of the results and discussion chapters. Figure 4.7c shows the isocentre slice of the calibration distribution filtered using the AM filter (as described above) and the RAR filter using a span = 7, degree = 3 and 2 iterations.

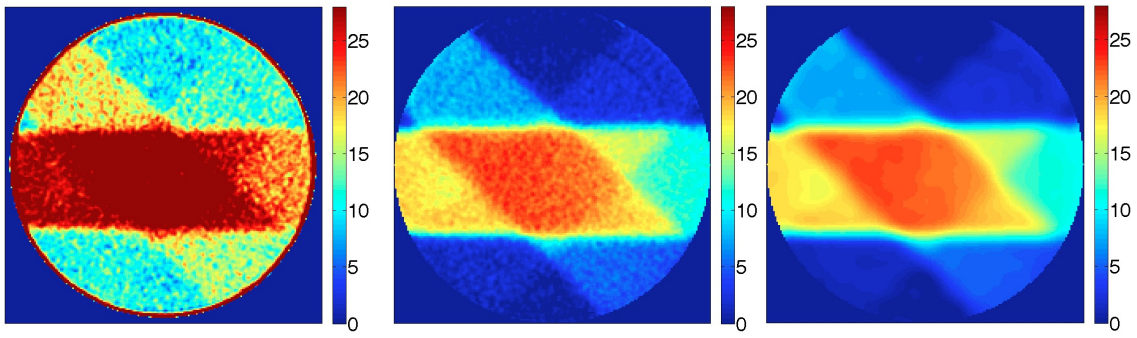

(a) (b) (c)

Figure 4.7: Each stage of image processing illustrated using a single CT slice acquired through the isocentre of the calibration distribution: (a) one unprocessed CT image, (b) an averaged, background subtracted image and (c) the averaged, background subtracted image filtered using both AM and RAR filtering techniques (see text for parameters).

4.5.2 Data Analysis

Data analysis for all experiments was performed using Matlab (version R2010b). The functions available in the statistics toolbox were employed for each data set. For the gel vial studies, the processed images were analyzed by extracting the mean and standard deviation of N_{CT} within a circular region of interest (ROI) for each

irradiated gel vial as well as an unirradiated gel included in each scan. The ΔN_{CT} was then determined by computing the difference in mean N_{CT} between the blank and irradiated gels. Further details on the data analysis procedures used for the vial studies are given in the experimental details sections of chapters 5 - 7.

For the 1 L gel experiments, dose response curves were generated using a new pixel-by-pixel calibration technique [130] unless otherwise noted. As its name suggests, this calibration method compares gel CT images to TPS calculated dose maps on a pixel-by-pixel basis to generate a full non-linear ΔN_{CT} to dose calibration curve. The process begins by applying a circular mask to each processed CT image that includes all pixels in the gel region of the image but excludes all pixels outside the gel by assigning them a value of zero. The corresponding treatment plan dose image is then resampled from a 176 x 244 image matrix with 1 mm^2 pixels to a 512 x 512 image matrix with 0.49 mm^2 pixels to match the dimensions of the CT image. This is followed by registration of the CT and treatment plan images using DICOM coordinates. Additional adjustments to the position of the treatment plan image (typically 1 - 2 pixels) are made by visually comparing treatment plan isodoses overlain on the gel CT image.

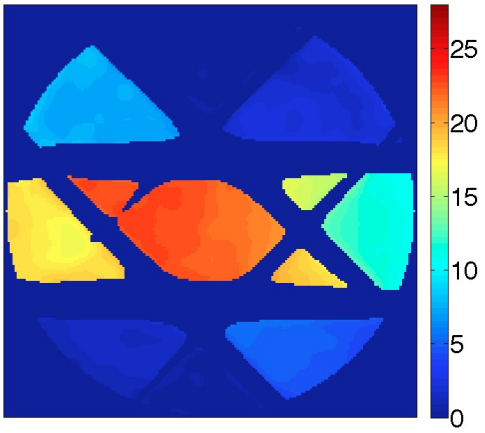

Figure 4.8: A processed CT image of the 3-field calibration dose distribution (i.e. figure 4.7c) with a 0.2 gradient threshold mask applied (colour bar shows ΔN_{CT} in HU).

With the CT and treatment plan images registered, the gradient across the treatment plan image is computed and a gradient threshold is applied to exclude pixels in high dose gradient regions in both the CT and treatment plan data sets. Removing steep dose gradients further minimizes any effect of mis-localization of the measured

and planned dose distributions by removing the regions where mismatch would produce large errors. Figure 4.8 illustrates a processed CT image of the 3-field calibration dose distribution with a 0.2 gradient threshold mask applied. The dark blue regions are the high gradient regions excluded from calibration curve construction (36% of pixels excluded). Controlled testing of the gradient threshold procedure indicates dose response curves are consistent for thresholds between 0.1 (more data removed) and 0.5 (less data removed) [130].

Following application of the gradient threshold, the pixel values in the CT and corresponding treatment plan images are paired for all pixels not excluded by the gradient removal procedure and N_{CT} are binned to 1 Gy. Initial testing shows the resulting calibration curve is independent of the degree of data binning for bin sizes up to and including 1 Gy [130]. ΔN_{CT} are then calculated by subtracting the N_{CT} corresponding to the minimum dose in the treatment plan (1 Gy for most studies) from the entire set of N_{CT} values.

Finally, a dose response curve is generated by plotting ΔN_{CT} as a function of dose and fitting the data to the empirical model described in equation 4.2:

$$\Delta N_{CT}(D) = \alpha + \beta \tanh(\gamma D - \phi) \tag{4.2}$$

where D is the dose in Gy and α, β, γ and ϕ are parameters estimated from the dose response data. Further analyses for each 1 L gel study are described in the experimental details sections of the results and discussion chapters that follow.

Chapter 5

Results & Discussion I: Characterization of the Essential Dosimetric Properties of a New Polymer Gel Dosimeter

5.1 Introduction

This chapter presents studies designed to characterize the fundamental dosimetric properties of a new polymer gel formulation optimized for CT readout. An intensity-modulated radiation therapy (IMRT) treatment validation is also presented to provide an example of a clinical application of the new gel dosimeter. The work presented forms a large portion of a recent article published in the international journal *Physics in Medicine and Biology* [130]. The gel characterization experiments were performed independently while the IMRT treatment validation is a collaborative contribution to the work. Details on the procedures used for each experiment are provided in section 5.2 while section 5.3 summarizes the results of each study and discusses their significance. Concluding remarks are given in section 5.4.

For many polymer gel dosimeters, the magnitude of the density change produced by exposure to ionizing radiation is small, resulting in low signal-to-noise CT images and poor dose resolution for CT PGD systems. For this reason, work in CT PGD has largely focused on improving the dose sensitivity of polymer gels by identifying new dose-sensitive monomers [95, 168] and finding methods to increase the concentration

of BIS in the gel system [44, 127–129]. Recently, a significant improvement was made using isopropanol as a cosolvent to increase the concentration of BIS in the gel formulation [129]. It was further found that comparable radiation sensitivity could be obtained by increasing the amount of BIS in the gel using large amounts of NIPAM as a cosolvent [44]. This new gel formulation, described in section 4.1.1, shows great promise for the development of a new CT PGD system with enhanced dose resolution and is the focus of this work.

Before the new formulation can be incorporated into a clinical RT dosimetry system, its dosimetric properties must be examined to ensure reliable dose measurements. These properties include the length of time required for the polymerization reaction to stabilize, or temporal stability, the extent to which the gel response changes in space over time, or spatial stability, the batch reproducibility of the gel, tissue equivalence and the dependence of gel response on radiation energy, dose rate, and temperature during irradiation and imaging. In this chapter, experiments are conducted to examine the temporal and spatial stability of the gel as well as its batch reproducibility and dose rate dependence. The tissue equivalence of the new formulation was not evaluated explicitly as it was confirmed by a separate group using Monte Carlo modelling studies [169]. Temperature dependencies are not investigated as gel temperature was carefully controlled throughout each experiment and recent work suggests radiation induced temperature increases in NIPAM gels do not affect their dose response [92]. Similarly, energy dependence was not examined as all irradiations were performed using 6MV photon beams.

In addition to the gel characterization studies, an IMRT treatment verification is presented as an example of a clinical application of the new gel dosimeter. With research focused on technique development, there have been very few reports on clinical applications of CT PGD in the literature [162, 170, 171]. The work presented by Audet *et al.* [162] is the most complete and although this study illustrated the early promise of CT PGD, it also highlighted the dose resolution limitations of the technique. The example IMRT treatment validation presented here illustrates the enhanced potential for clinical application offered by the next generation CT PGD system introduced in this work.

5.2 Experimental Details

All polymer gels in this work were fabricated as described in section 4.1.1. Each gel was irradiated with 6 MV photons using a Varian Clinac 21EX linear accelerator, between 6 and 8 h after fabrication (unless otherwise indicated). Gels were maintained at a consistent temperature during and after irradiation to ensure reproducible reaction kinetics across all experiments [76]. A machine dose rate of 400 MU/min was used for each experiment unless otherwise noted. All treatment planning was performed using the Eclipse treatment planning system running version 10.0 of the analytical anisotropic algorithm. Further details for each study are provided below.

5.2.1 Treatment Planning & Irradiation

Gel Characterization

For the temporal stability study, the gel solution was divided between 10 scintillation vials that were irradiated individually within their cylindrical pots using the acrylic phantom described in section 4.3.2. The irradiation was based on a simple treatment plan designed using a planning CT scan of the phantom with a blank gel inserted at its centre and the CadPlan TPS (Varian) [122]. The plan consisted of two parallel opposed, 10 x 10 cm^2 fields, used to deliver a uniform dose of 10 Gy to each gel vial.

For the remaining studies, the completed gel solutions were transferred to 1 L cylinders and irradiated using the head and neck phantom described in section 4.2. The 1L gel used to investigate spatial stability was positioned at planning CT and radiation delivery using the phantom with the head removed. A treatment plan was designed using the planning CT scan to deliver a uniform dose of 10 Gy to half the gel container. The plan consisted of two parallel opposed 20 x 8 cm^2 wedged fields, oriented such that the axis of each field was perpendicular to the axis of the 1 L cylinder. The beam arrangement and resulting computed dose distribution at isocentre for the plan are illustrated in figures 5.1a and c, respectively.

All gels used to investigate batch reproducibility and dose rate were irradiated with the 3-field treatment plan described in section 4.3.2. A schematic diagram illustrating the regions of each 1 L gel that were irradiated for these studies is provided in figure 5.2. For the local intra-batch investigation, the plan was delivered to one batch of gel at the bottom of the 1 L cylinder, while for the global intra-batch study, the plan was delivered to a second batch of gel at both ends of the cylinder. For the inter-batch

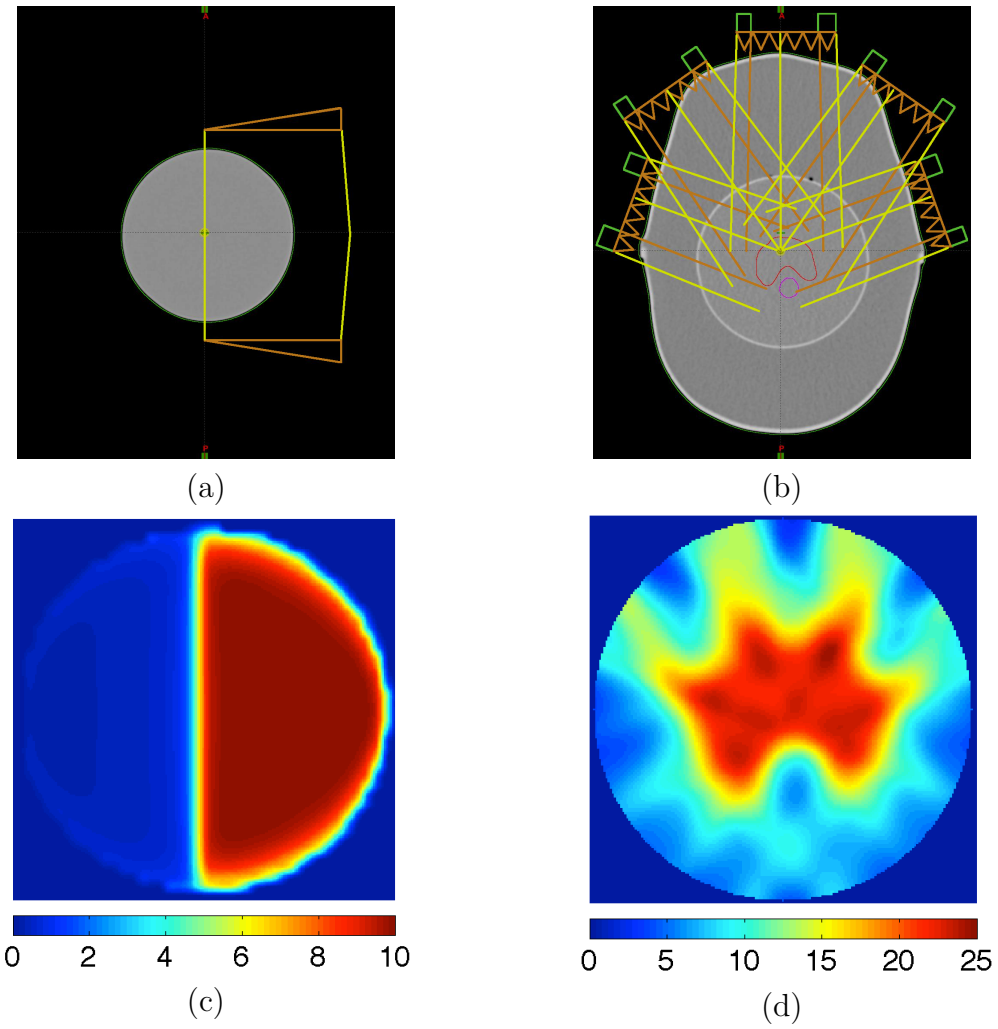

Figure 5.1: Treatment plan beam arrangements and calculated dose distributions at isocentre (colourbar in Gy) for the spatial stability study ((a) and (c)) and IMRT treatment validation ((b) and (d)). *Reproduced with permission* [130].

study, the plan was delivered to identical regions of 3 gel cylinders, each fabricated on a different day. For the dose rate study, the 3-field plan was delivered to two regions of gel, as was done for the global intra-batch study (figure 5.2b), at 600MU/min and 100MU/min, respectively. In cases where two separate dose distributions were delivered to a single gel, the irradiations were spaced at least 6.5 cm apart to minimize scattered radiation between neighbouring distributions.

IMRT Treatment Validation

For the IMRT treatment validation, both calibration and test irradiations were delivered to the same gel dosimeter. This streamlined the PGD process and ensured calibration and treatment irradiations were performed on phantoms of the same size to avoid any discrepancies in dose response due container size [89]. Treatment isocentres were separated by over 6.5 cm in the superior-inferior direction to minimize the scattered dose ($< 3\%$) between the two distribution. This allowed images of the central region of the gel to be used for background subtraction, and facilitated calibration, test irradiation and background images to all be obtained from a single dosimeter. For treatment, the gel was positioned on the LINAC couch as for at planning CT and moves from set-up position to treatment isocentres were made as defined in the treatment plans. The calibration irradiation consisted of the 3-field treatment plan described in section 4.3.2. The beam arrangement for the IMRT treatment plan is illustrated in figure 5.1b. The plan consisted of five fields spread over anterior gantry angles and was designed to treat a concave target, the inferior half of which is wrapped around an avoidance structure. Figure 5.1d shows the planned dose distribution at the isocentre slice. The plan prescription dose was 22 Gy, with a maximum dose of 24.8 Gy (112.5%). A dynamic MLC technique was used for IMRT delivery.

5.2.2 Computed Tomography Imaging

All gel imaging was performed using the HiSpeed FX/i single-slice CT scanner described in section 4.4.1. The scanning parameters used for each study are summarized in table 5.1 and were selected to produce low image noise while avoiding excessive tube load and CT dose that can result from using a high number of image averages [167]. For a detailed discussion on image parameter selection for CT PGD using a single slice CT scanner, the reader is referred to Hilts *et al.* [122]. For all scanning sessions, a scanner warm-up series was performed prior to image acquisition to min-

Parameter	Value
Tube voltage	120 kV
Tube current	200 mA
Slice thickness	3, 5, 10 mm
Field of view	25×25 cm^2
Reconstruction matrix	512×512
Pixel size	0.49×0.49 mm^2
Reconstruction algorithm	SOFT, STANDARD
Number of image averages	16, 25, 32

Table 5.1: Scanning parameters used for CT PGD read-out for the gel characterization and IMRT treatment validation experiments. Parameters specific to each experiment are detailed in the text. *Reproduced with permission* [130].

imize variations in x-ray tube temperature resulting from increasing tube load [84]. Most scan parameters were consistent for all experiments, with the exception of slice thickness, number of image averages and reconstruction algorithm, which were varied based on the needs of individual experiments. Further details particular to each study are summarized below.

Gel Characterization

Gel vials used to investigate temporal stability were imaged one at a time between 3 - 45 hours post-irradiation using the styrofoam phantom described in section 4.4.2. At the beginning of each scan, the gel vial was removed from its cylindrical pot and placed in the top cradle of the phantom. The remaining cradles were filled with blank gels. Sixteen images were then acquired through the centre of each vial using 10 mm slice thickness and an additional 16 images were acquired with the phantom filled with blank gels for background subtraction.

For the spatial stability study, batch reproducibility and dose rate investigations, gels were positioned at CT readout using the head and neck phantom as described in section 4.4.2. The gel used to examine spatial stability was imaged at four locations along the length of the cylinder between 15 - 47 hours after irradiation. Thirty-two images were acquired for each scan using 5 mm slice thickness and consecutive scans were separated by 3.0 cm to avoid CT dose between neighbouring acquisitions [163]. An additional set of 32 images were acquired at the same locations along the length of a blank gel for background subtraction.

For the batch reproducibility and dose rate experiments, 25 images were acquired

(a) (b) (c)

Figure 5.2: Regions of irradiated gel (shaded blue) and the corresponding CT imaging locations (solid black lines) for the (a) local intra-batch reproducibility study, (b) global intra-batch and dose rate studies and (c) inter-batch reproducibility study.

using 3 mm slice thickness at the locations shown in figure 5.2 (solid black lines). The local intra-batch gel was scanned at three locations within the irradiated region: at the centre of the distribution and at ± 3 mm from the central image. For the remaining batch reproducibility studies and dose rate investigation, images were acquired through the centre of each dose distribution. An additional set of 25 images were acquired for background subtraction at central locations within each 1 L dosimeter that received less than 3% scattered dose from neighbouring irradiations.

IMRT Treatment Validation

For the IMRT treatment validation, images of the calibration, background and test irradiation regions of the 1L gel were collected during the same scanning session using identical scan parameters. Images of the 3-field irradiation were used for gel calibration. Imaging was performed 20 hours after irradiation to ensure the gel response had stabilized (see section 5.3.1). The head and neck phantom was positioned on the CT couch as described in section 4.4.2. Twenty-five images were acquired using 3 mm slice thickness at each scan location to ensure adequate sampling of superiorinferior variations in dose for the IMRT plan. A higher number of images were acquired than in the work of Hilts *et al.* [164] to compensate for the increase in image noise expected to occur with a reduced slice thickness. The total approximate scan time was 45 min.

5.2.3 Image Processing and Data Analysis

Image processing for all studies was performed using the procedures described in section 4.5.1. Image averaging and background subtraction were performed for all CT data sets to reduce image noise and remove image artefacts, respectively. The resulting images were then filtered using an AM filter (3 x 3, n = 1) for further removal of stochastic noise. Further filtering was performed using the RAR filter with parameters chosen based on recommendations given by Jirasek *et al.* [126]. Further details specific to each study are given below.

Gel Characterization

For the temporal stability study, CT images were RAR filtered using a span = 4, degree = 3 and 2 iterations. The mean and standard deviation of N_{CT} within a circular 10 pixel radius ROI were then computed for each irradiated gel as well as an adjacent blank gel included in each scan. The ΔN_{CT} was then determined by

computing the difference in mean N_{CT} between the irradiated vial and the blank gel. The time required for post-irradiation polymerization to stabilize was determined by plotting ΔN_{CT} as a function of the time, Δt, between irradiation and imaging. The data were summarized using the set of parameters a, b and c of the model function shown in equation 5.1 below. This function was found, empirically, to describe the measured data:

$$\Delta N_{CT}(t) = a - be^{\frac{\Delta t}{c}}. \tag{5.1}$$

The function was used to compute the error, $\varepsilon_{\Delta N_{CT}}$, between ΔN_{CT} observed at the beginning and end of a hypothetical scan session conducted before stabilization of polymerization. Each hypothetical error was then plotted as a function of post-irradiation scan start time for scan durations of 5 - 60 minutes. A dose response function (equation 4.2), representative of the gels investigated in this work, was then used to convert ΔN_{CT} into dose to assess the dosimetric error, ε_D, associated with imaging gels before stabilization of polymerization.

The CT images for the spatial stability study were RAR filtered using a span = 2, degree = 1 and 1 iteration. The resulting processed images were analyzed by extracting N_{CT} profiles through the diameter of the 1 L gel cylinder for each scan. The mean and standard deviation of N_{CT} were then computed over the width of each profile and plotted as a function of distance in the image. The ΔN_{CT} was computed by subtracting the mean N_{CT} in the tail region of each profile (note this also served to align the profiles at 0H). Dose profiles were then constructed analogously to the temporal stability study by applying an empirical dose response fit function (equation 4.2) to ΔN_{CT} profiles.

For the batch reproducibility and dose rate studies, CT images were RAR filtered using span = 7, degree = 3 and 2 iterations. Dose response curves were then constructed using the procedure outlined in section 4.5.2.

IMRT Treatment Validation

Following image averaging, background subtraction and AM filtering, gel CT images of the calibration and IMRT irradiations were RAR filtered using a span = 5, degree = 3 and 2 iterations. A calibration curve was constructed using the processed image of the 3-field distribution and the new pixel-by-pixel calibration technique described in section 4.5.2. The partial derivative $\partial(\Delta N_{CT})/\partial \mathrm{D}$ was computed from the calibration function to determine the dose resolution of the system using a 1σ confidence interval

as described in section 3.13. The Eclipse dose file for the IMRT distribution was then resampled from a 176 x 244 image matrix with 1 mm^2 pixels to a 512 x 512 image matrix with 0.49 mm^2 pixels to match the dimensions of the CT images. This was followed by registration of each TPS dose map with the corresponding IMRT gel CT image using DICOM coordinates (this is possible since every effort is made to ensure the gel position at time of planning CT and read-out CT are identical). At this stage, the calibration curve was used to convert CT number to dose for each IMRT CT image. The measured and planned IMRT doses were then compared using dose profiles, isodose plots and dose volume histograms (DVHs). Examination of TPS computed and gel measured isodose lines allowed fine-tuning of image registration by manually shifting one distribution relative to the other by up to a few pixels in each direction to provide the best possible match. Further analyses were performed to compute 2D and 3D gamma distributions. The gamma index is a metric introduced by Low *et al.* [172] and is computed on a pixel-by-pixel basis using equations 5.2 and 5.3:

$$\gamma(\bar{r}_m) = min\{\Gamma(\bar{r}_m, \bar{r}_c)\}\forall\{\bar{r}_c\} \tag{5.2}$$

$$\Gamma(\bar{r}_m, \bar{r}_c) = \sqrt{\frac{|\bar{r}_c - \bar{r}_m|^2}{\Delta d_M^2} + \frac{(D_c - D_m)^2}{\Delta D_M^2}} \tag{5.3}$$

where D_m is the dose at point $\bar{r}_m$ in the gel dose map, D_c is the dose at point $\bar{r}_c$ in the TPS dose distribution, Δd_M is the acceptance criteria for spatial position (i.e. the acceptable *distance to agreement* between $\bar{r}_m$ and $\bar{r}_c$) and ΔD_M is the acceptance criteria for dose. Pixels with a $\gamma(\bar{r}_m) \leq 1$ indicate acceptable agreement is achieved between the gel and TPS while pixels with a $\gamma(\bar{r}_m) > 1$ represent areas where unacceptable agreement is present.

5.3 Results & Discussion

5.3.1 Temporal Stability

The evolution of post-irradiation polymerization for gel vials irradiated to 10 Gy is illustrated in figure 5.3. Error bars represent the standard deviation of ΔN_{CT} computed at the centre of each vial. It is readily seen that a rapid initial increase in ΔN_{CT} occurs between 0 - 15 hours after irradiation. Beyond 15 hours post-irradiation,

ΔN_{CT} agree within experimental error (with the exception of the 45 hour point), indicating the polymerization reaction has stabilized.

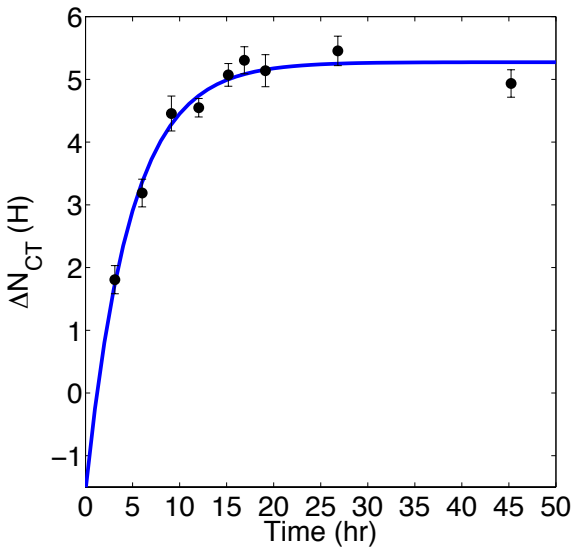

Figure 5.3: The ΔN_{CT} measured at post-irradiation times between 3 - 45 hours for gel vials irradiated to 10 Gy. Error bars represent the standard deviation of ΔN_{CT} at the centre of each vial. The data are fit to a mono-exponential saturation function.

Figure 5.4 shows the estimated impact associated with imaging a gel before polymerization stabilizes on (a) ΔN_{CT} and (b) dose for scan sessions of 5 - 60 minutes duration. As expected, $\varepsilon_{\Delta N_{CT}}$ and ε_D decrease as the time between irradiation and imaging increases and as scan duration decreases for all post-irradiation scan start times. The largest errors occur when gels are scanned immediately after irradiation for long scan periods. The ΔN_{CT} measured at the beginning and end of a 60 minute scanning session performed immediately after irradiation can differ by more than 1.2 H, producing a dose difference of approximately 2.5 Gy. However, scanning sessions kept under 10 minutes show $\varepsilon_{\Delta N_{CT}}$ of less than 0.3 H, resulting in ε_D of less than 0.5 Gy, regardless of scan start time.

Based on the results of figure 5.3, it is recommended that at least 15 hours is allowed between irradiation and imaging for the new gel recipe. However, it may be possible to image gels before this time if scan duration is kept short. Figure 5.4 suggests scanning sessions kept under 10 minutes result in dose errors < 0.5 Gy, regardless of scan start time. For this reason, it may be feasible to image gels before stabilization of polymerization if enough polymer has formed at the time of scanning to produce adequate image contrast. This would be an attractive augmentation to the

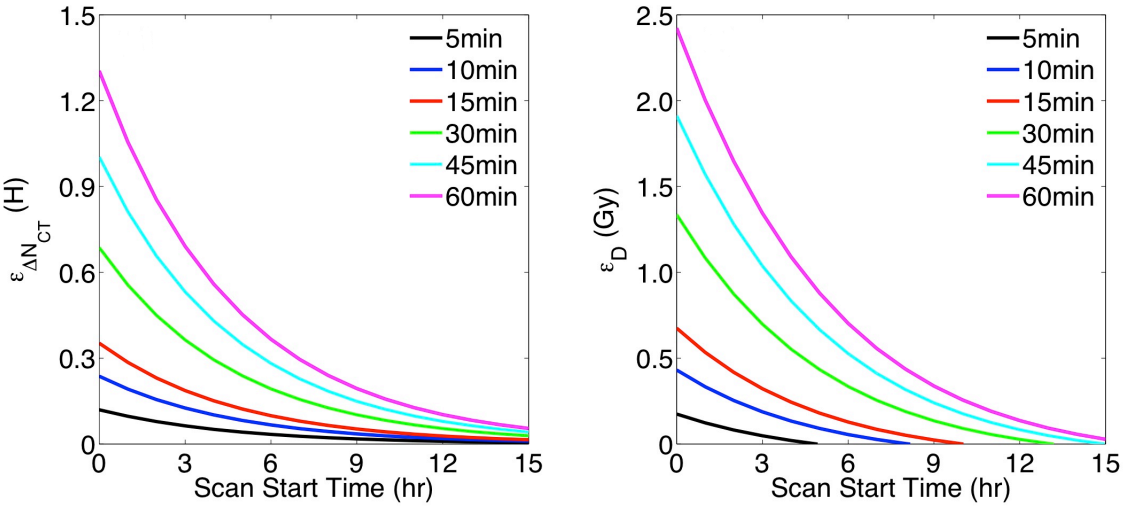

(a) (b)

Figure 5.4: Estimated impact of imaging a gel before polymerization stabilizes on (a) ΔN_{CT} and (b) derived dose for imaging sessions between 5 - 60 minutes in length. Each curve represents the difference between measurements acquired at the beginning and end of a scan session (as given in the legend) for a given scan start time post-irradiation.

process of PGD as it would significantly reduce the overall time required to perform a gel dosimetry experiment [43], making it a more feasible clinical tool.

Previous temporal stability investigations for other gel formulations reveal post-irradiation polymerization is highly dependent on gel composition [173], with stabilization time varying between 10 - 30 hours [71, 74, 174–176]. Similar variability is observed for NIPAM gels. In a recent study, it was found that the polymerization reaction for a 6%T, 50%C NIPAM gel occurs 24 hours post-irradiation using nuclear magnetic resonance relaxometry [95] while the same gel investigated by another group showed stabilization occurs 5 hours after irradiation using an optical read-out technique [177]. Additional studies report polymerization stabilizes 24 hours after irradiation for both a 7.5%T, 33%C NIPAM gel imaged using CT [178] and a 5.5%T and 45%C NIPAM gel imaged using OptCT [179]. It is believed these differences may be due to the different gel properties probed by the imaging modalities used in each study, or alternatively, the differences in crosslinker concentration used in each investigation [180].

5.3.2 Spatial Stability

Processed CT images of the 1 L gel that received 10 Gy to half its volume are illustrated in figure 5.5 for scans acquired between 15 - 47 hours post-irradiation. Corresponding profiles of (a) ΔN_{CT} and (b) dose extracted along the diameter of the 1 L gel are shown in figure 5.6. Error bars represent the standard deviation of ΔN_{CT} computed over the width of each profile. While the profiles agree within experimental error for scans acquired 15 - 36 hours post-irradiation, a small overshoot is observed for each profile acquired 47 hours after irradiation (see figure 5.6 insets). It was determined that this overshoot results in a maximum difference of 5% between dose profiles. The overshoot found here for the new gel is much smaller than that observed for PAG [173, 181] and normoxic methacrylic acid (nMAG) gels [173, 182], and is comparable to the overshoot observed for normoxic polyacrylamide (nPAG) gels [173].

The cause of the overshoot in gel response is presently unknown. The overshoot observed in PAGs is attributed to migration of unreacted monomer from regions of unirradiated gel into irradiated areas. Following migration, these *fresh* monomers go on to react with long-lived polymer molecules, resulting in an increase in the amount of polymer formed in the irradiated region [181, 183]. It is possible that a

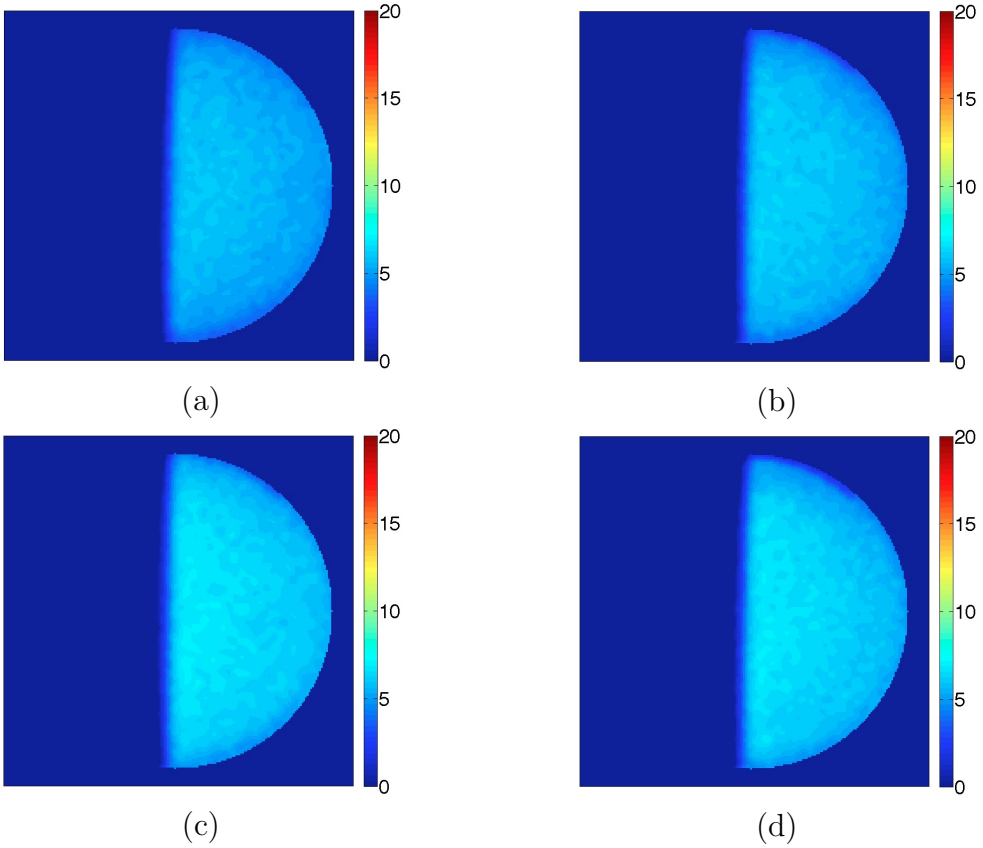

Figure 5.5: Processed CT images of the 1 L gel used to examine spatial stability acquired at (a) 15, (b) 25, (c) 36 and (d) 47 hours post-irradiation.

similar phenomenon is responsible for the loss of spatial stability observed for the new gel formulation, however, further investigation is required to determine the exact mechanism causing the overshoot. Nevertheless, in light of the overshoot found, an upper limit on the time between irradiation and imaging of 36 hours is recommended for the new gel formulation.

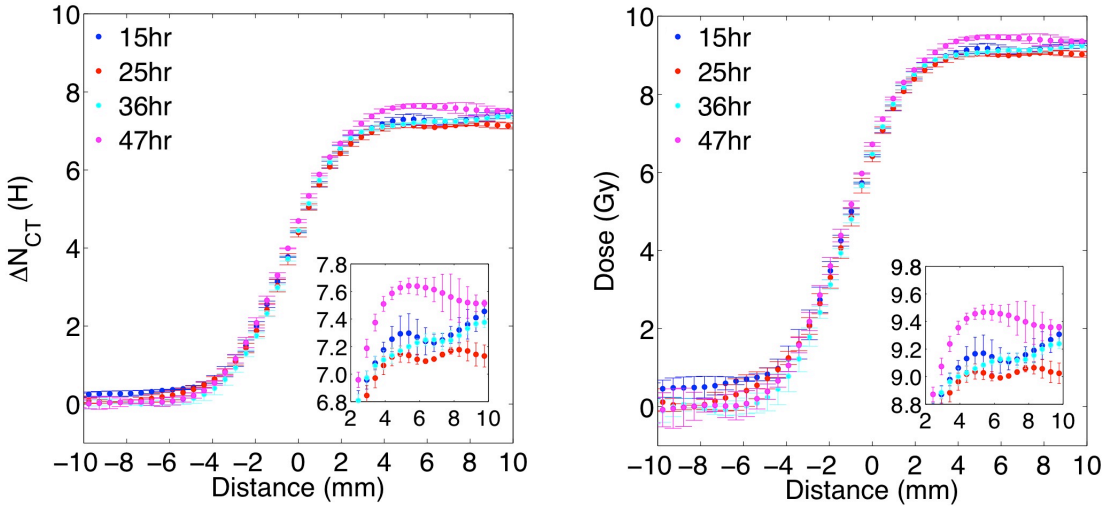

(a) (b)

Figure 5.6: Profiles of (a) ΔN_{CT} and (b) dose along the diameter of a 1 L gel cylinder irradiated to 10 Gy over half its volume. Profiles were extracted from images acquired between 15 - 47 hours post-irradiation.

5.3.3 Batch Reproducibility

The measured dose response for the local intra-batch (slices 1 - 3), global intra-batch (regions 1 - 2), and inter-batch (batches 1 - 3) studies are illustrated in figure 5.7a with the average fit function as a reference, while figure 5.7b shows the differences (ΔN_{CT}^{Diff}) between the measured dose response and average fit for each study. The error bars associated with each curve represent the standard deviation of estimated ΔN_{CT} values. For each investigation, it is readily seen that excellent dose response reproducibility is achieved over the entire dose range studied. Table 5.2 summarizes the fit parameters computed for each investigation, along with their corresponding 95% confidence intervals. The fit parameters for each study agree within the estimated range of values, again indicating the batch reproducibility for the new gel formulation is excellent.

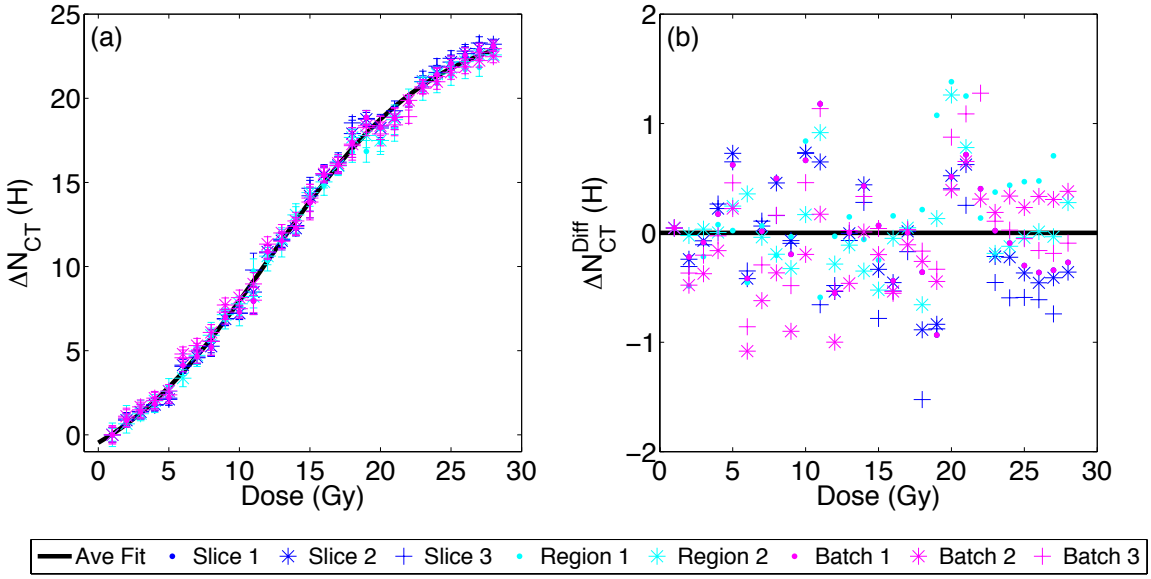

Figure 5.7: (a) Measured dose-response curves for the local intra-batch (slices 1 - 3), global intra-batch (regions 1 - 2), and inter-batch (batches 1 - 3) investigations with the average fit function (equation 4.2) included as a reference. (b) The differences between the measured dose response and average fit function for each study.

The remarkable intra-batch reproducibility found in this study, not only within a single region of gel but throughout a 1 L volume, indicate both calibration and test irradiations can be delivered to the same gel during clinical dosimetry experiments. This is a highly attractive feature for the new gel formulation, as the potential for dose inaccuracies due to discrepancies between calibration and test gels [173] is removed. Similarly, the excellent inter-batch reproducibility indicates the new gel is robust and insensitive to small variations in the PGD process. This suggests that certain components of the PGD process, such as irradiation and imaging of the dosimeter, may be delegated to other RT team members, facilitating the routine use of PGD in the clinical environment.

		α	β	γ	ϕ
Local Intra-batch	Slice 1	10.8 (10.1, 11.5)	14.0 (12.4, 15.5)	0.09 (0.07, 0.10)	1.1 (0.9, 1.3)
	Slice 2	10.9 (10.2, 11.5)	13.9 (12.5, 15.2)	0.09 (0.08, 0.10)	1.1 (0.9, 1.3)
	Slice 3	10.8 (10.1, 11.6)	14.0 (12.4, 15.7)	0.09 (0.07, 0.11)	1.1 (0.9, 1.3)
Global Intra-batch	Region 1	10.0 (9.2, 10.8)	14.2 (12.3, 16.0)	0.08 (0.07, 0.10)	0.9 (0.7, 1.2)
	Region 2	10.3 (9.5, 11.0)	14.2 (12.6, 15.8)	0.08 (0.07, 0.10)	1.0 (0.8, 1.2)
Inter-batch	Batch 1	10.8 (10.1, 11.5)	14.0 (12.4, 15.5)	0.09 (0.07, 0.10)	1.1 (0.9, 1.3)
	Batch 2	9.9 (9.2, 10.6)	14.3 (12.9, 15.7)	0.08 (0.07, 0.09)	0.9 (0.7, 1.1)
	Batch 3	10.4 (9.4, 11.4)	14.7 (12.4, 17.0)	0.08 (0.06, 0.09)	0.9 (0.7, 1.2)

Table 5.2: Fit parameters α, β, γ and ϕ (see equation 4.2) and corresponding 95% confidence intervals computed from the measured dose response for the local intra-batch (slices 1 - 3), global intra-batch (regions 1 - 2), and inter-batch (batches 1 - 3) investigations.

5.3.4 Dose Rate Dependence

Figure 5.8 shows the measured dose response for gels irradiated at machine dose rates of 100 MU/min and 600 MU/min. A dose response curve from the batch-reproducibility study generated for a 400 MU/min is included for comparison purposes. It is clear from figure 5.8 that the dose response changes as a function of dose rate and the magnitude of the dependence changes as a function of dose. For doses less than 5 Gy, the dose response curves agree within experimental error for all dose rates. Between 5 - 20 Gy, the slope of the dose response decreases as dose rate increases, and beyond 20 Gy, the dose response begins to saturate as changes in slope begin to stabilize.

The observed dose rate dependence found for the new gel formulation indicates that significant dosimetric error could occur in a clinical application if the machine dose rate is not consistent between calibration and test irradiations. As such, caution

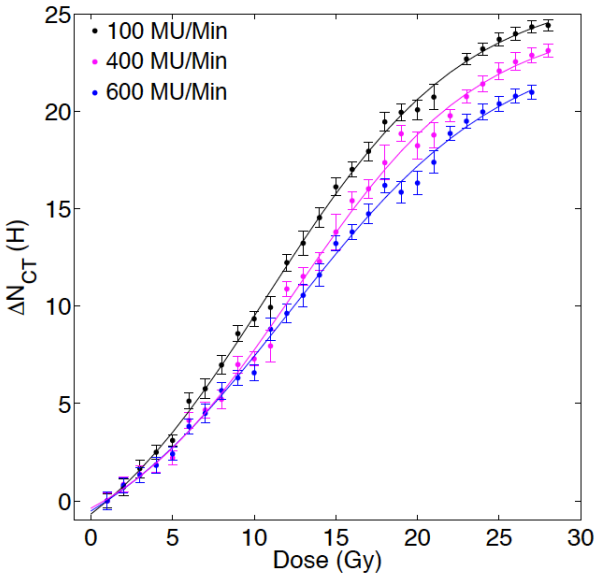

Figure 5.8: The measured dose response for gels irradiated at machine dose rates of 100 MU/min, 400 MU/min and 600 MU/min.

must be exercised with respect to machine dose rate for any clinical application of the new gel formulation. The implications for variations in other types of dose rate are examined in chapter 7. A separate study that examined a 7.5%T, 33%C NIPAM gel also found a significant dose rate dependence [178], further indicating caution must be used when irradiating the new gel using different machine dose rates. However, a recent study that examined a 6%T, 50%C NIPAM gel formulation reports small variations in dose rate do not significantly affect the dose response of the gel [95]. This suggests it is possible that an upper limit exists below which fluctuations in dose rate will pose minimal impact on dose measurements for certain NIPAM gel recipes.

Work examining older gel formulations show little to no dose rate dependence for PAG and nPAG gels, but a significant dose rate dependence for nMAG gels [173]. As dose rate increases, the slope of nMAG dose response curve decreases. It is interesting to note, a similar behaviour is observed when nMAG gels are irradiated with sequential beams. In that case, as the dose per beam increases, the slope of the dose-response curve decreases [184].

The variations in dose rate dependence observed for different gel formulations can be attributed to the dominant radical chain termination processes present in each gel system. In PAG and nPAG gels, termination is dominated by chain-transfer to gelatin, which involves one radical centre. As chain propagation also involves one radical, the rate of each reaction is proportional to radical concentration. Therefore, changes in radical concentration, or by extension, dose rate, do not influence the amount of polymer formed. In contrast, in nMAG gels, termination is dominated by bimolecular termination. As two radicals are eliminated in these reactions, the rate of termination is proportional to the square of the radical concentration. This results in more termination reactions as radical concentration (or dose rate) increases, and less polymer formation at higher dose rates [101, 184].

It is possible that the dominant termination process in the new gel is bimolecular termination caused by self-cross-linking of NIPAM linear chains. Work in the field of responsive hydrogel particles indicates formation of a cross-linked NIPAM network can occur in the absence of BIS crosslinker [185]. The reaction involves chain transfer to polymer molecules followed by monomer addition, and finally, termination by coupling as the cross-linked network forms [186]. This reaction increases the number of bimolecular coupling terminations in the gel system, and may lead to a shift in the dominant termination mechanism. However, further study is required to determine the mechanism responsible for the dose rate dependence observed for the new gel.

5.3.5 IMRT Treatment Validation

Figure 5.9 shows isodose lines computed by the TPS overlaid on gel measured doses that are binned to the corresponding isodose levels in the (a) axial, (b) sagittal and (c) coronal planes (isocentre slices shown). It is readily seen that while small deviations exist, the isodose lines computed by the TPS agree well with the gel measured doses in each plane. A 2D gamma distribution comparing planned and measured doses at isocentre (3%, 3 mm) is shown in figure 5.10a and further illustrates the excellent agreement obtained between the TPS and the new CT PGD system. A nearly complete 2D gamma pass rate of 99.3% is obtained for the isocentre slice and the 3D gamma pass rate for the entire irradiated volume is 93.4%. The lower 3D gamma pass rate compared to the isocentre slice is due to poorer agreement of off-axis slices. It is possible this lack of agreement is due to variations in N_{CT} associated with increasing x-ray tube load that can occur when a large number of images are acquired on a single slice CT scanner. Similarly, figure 5.10b shows the whole volume DVH for the gel measured data agrees well with the DVH predicted by the TPS but indicates consistently higher volumes for mid-range doses. Neverthless, the agreement observed in the profile comparisons shown in figure 5.11 illustrate the exceptional ability of the new CT PGD system to record the type of spatial variation seen in complex dose distributions such as those delivered with IMRT. The high spatial resolution of the technique is highlighted in the accurate representation of the steep dose gradients around the critical structure and at the edges of the high dose region. In addition, the dose resolution computed for the system was excellent, ranging from 0.09 - 0.2 Gy for doses between 0 - 20 Gy and 0.2 - 0.4 Gy for doses between 21 - 28 Gy.

The IMRT treatment verification performed using the prototype CT PGD system introduced here shows a significant improvement over previous clinical applications found in the literature [162, 170, 171]. This is readily seen by the reduction in image noise and the subsequent ability to resolve low isodose levels in the IMRT dose distribution as illustrated by figure 5.9. Moreover, this second generation CT PGD system can achieve dose resolutions of better than 0.5 Gy when the full dose response is utilized and high spatial sampling ($<$0.5 x 0.5 mm^2) that provides excellent resolution for spatial details. However, the high dose requirement and possible effects of varying dose rate on dose response are limitations for the system. These limitations were accounted for in the current test IMRT irradiation by setting the prescription dose to 22 Gy, which minimized dose rate effects by ensuring that the machine dose

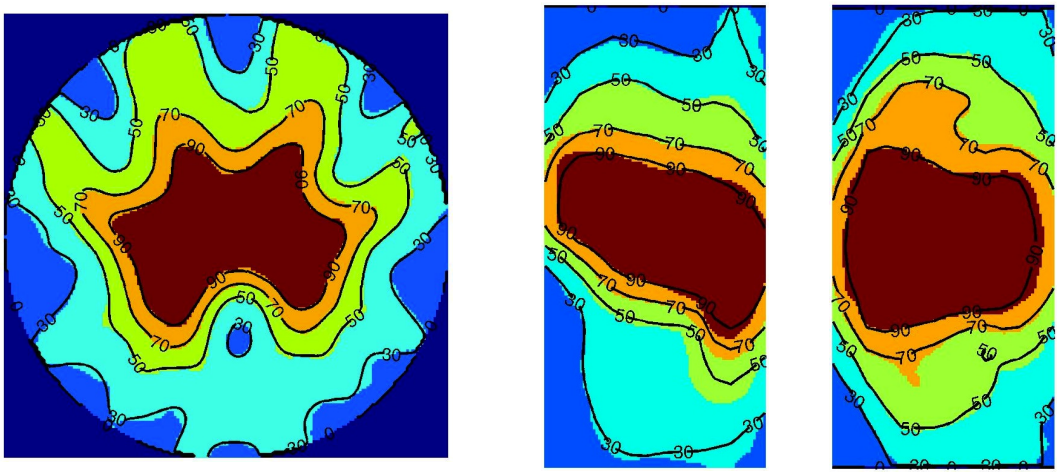

(a) (b) (c)

Figure 5.9: Calculated isodose lines (30, 50, 70 and 90%) computed by the TPS overlaid on gel measured doses binned to the corresponding isodose levels in the (a) axial, (b) sagittal and (c) coronal planes (isocentre slices shown).

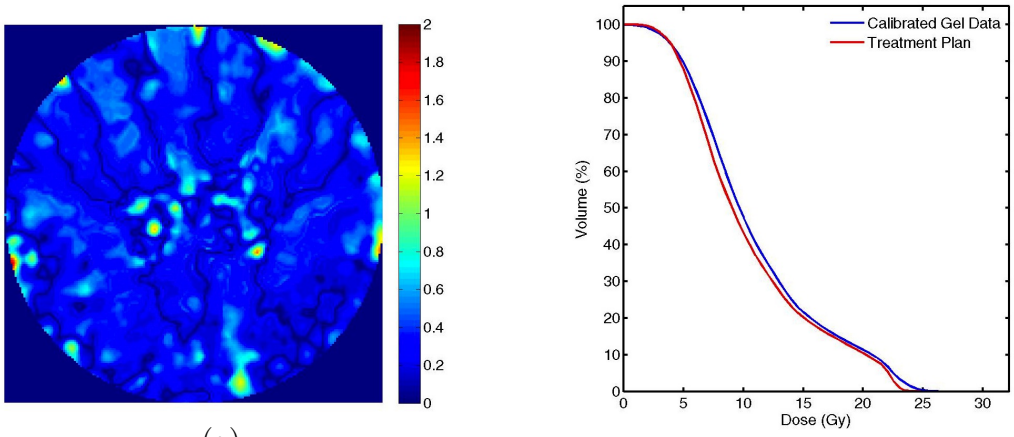

(a) (b)

Figure 5.10: Comparison of measured and calculated doses for the IMRT treatment validation using (a) gamma analysis (3 %, 3 mm) at the isocentre slice and (b) DVHs for the whole treatment volume.

rate remained constant throughout irradiation. This is clearly not equivalent to typical RT dose fractions (∼2 Gy), and for IMRT, means any effect of MLC leaf motion speeds is not recorded. Nevertheless, the high dose requirement is an asset for other clinical applications, such as stereotactic radiosurgery or stereotactic body radiation therapy, where high single fraction doses are delivered or when recording the cumulative dose due to multiple fractions is of interest. Overall, the proof of principle clinical application presented here has shown the promise of CT PGD for clinical 3D dosimetry.

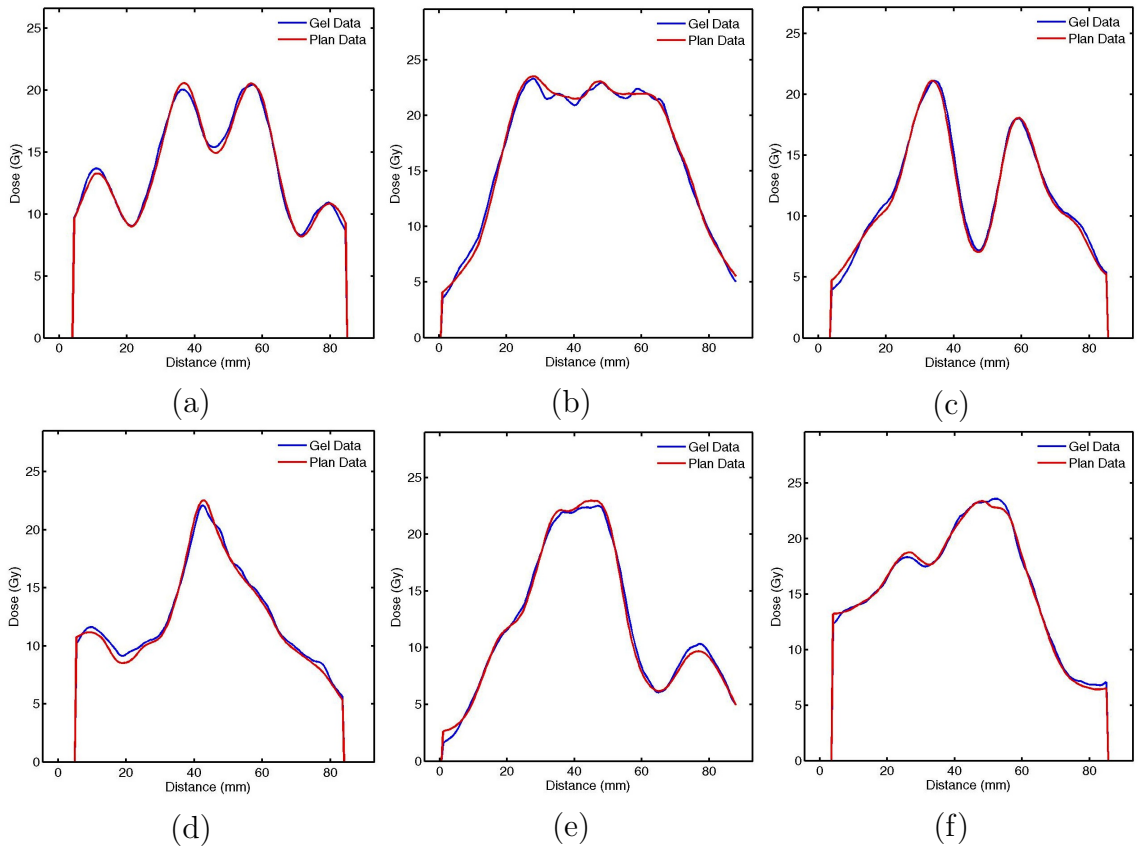

Figure 5.11: Profiles through the isocentre slice of the IMRT dose distribution. Row profiles are shown for the (a) top (b) middle and (c) bottom of the distribution and column profiles are shown for the (d) left, (e) middle and (c) right of the distribution.

5.4 Chapter Summary

The work presented in this chapter provides valuable information about the dosimetric properties of the new gel as well as the PGD process required when conducting RT

dosimetry experiments using the new formulation. The temporal and spatial stability studies demonstrate the gel response is stable between 15 - 36 hours after irradiation and it is therefore recommended that the new gel be imaged within this time-frame. Batch reproducibility was found to be excellent for doses between 0 - 28 Gy. This finding indicates calibration and test irradiations can be performed in the same gel dosimeter and ensures consistent results will be obtained for different gel batches. A significant dose rate dependence was found for gels irradiated with machine dose rates between 100 - 600 MU/min, indicating a consistent machine dose rate must be used for both calibration and test irradiations to ensure reliable dose measurements. The implications for dependencies on other types of dose rate are presented in chapter 7. Finally, a prototype clinical application for an IMRT irradiation was found to have excellent agreement with calculated doses and has demonstrated the promise of this second generation CT PGD system for 3D dose verification of spatially complex dose distributions. Overall, the results of this chapter indicate the new gel formulation shows great promise for use in an CT PGD system for complex RT dosimetry.

Chapter 6

Results & Discussion II: Commissioning a Multislice X-ray Computed Tomography Scanner for Polymer Gel Dosimetry

6.1 Introduction

This chapter presents a series of studies performed to commission a multislice CT scanner for CT PGD. A manuscript on this material is currently in preparation for submission to the peer-reviewed journal *Medical Physics*.

In the previous chapter, the new polymer gel formulation used throughout this work was demonstrated to have promising dosimetric characteristics for use in a CT PGD system. The new gel was specifically designed to have enhanced radiation sensitivity to improve the contrast of gel CT images and provide superior dose resolution compared to previous formulations. However, even with a high-sensitivity gel, CT PGD requires image averaging to reduce the stochastic noise in gel CT images, with upwards of 30 images required at each slice location to achieve optimal image quality. Depending on the imaging parameters used for the scan, this high number of images can place excessive load on the x-ray tube, particularly if images must be acquired at several slice locations in the gel. For example, a 12 cm long gel imaged using 3 mm slice thickness and 30 image averages per slice would required over 1000 CT images. This level of scanning would overheat the x-ray tube in most single slice CT

scanners, potentially generating significant variations in N_{CT} and initiating a tube cooling period to prevent x-ray tube damage. As such, a new technique for imaging large gel volumes is required for CT PGD that provides consistent measures of N_{CT} in a reasonable amount of time.

It is possible that the tube load effects observed for single slice CT scanners may not be present in multislice systems. As multiple image slices are acquired simultaneously at each couch position, the load placed on the x-ray tube during scanning with a multislice scanner will be substantially reduced [187]. This may in turn reduce or even eliminate the variations in N_{CT} seen on single slice machines as the number of images acquired increases. Another obvious benefit of using a multislice CT scanner for gel imaging is the reduction in the total time required for a scan due to the more efficient method of collecting slice data and the reduction in tube load which may negate the need for cooling periods during acquisition. Nevertheless, multislice systems present their own unique challenges when utilized for gel dosimetry. The use of a cone beam of x-rays may introduce significant variability in N_{CT} across image slices acquired simultaneously using the multislice detector array due to the anode heel effect discussed in section 2.2.1. Moreover, the increase in scattered radiation associated with a cone-beam of x-rays may result in significantly greater image noise [188] that may degrade the quality of gel CT images. For these reasons, it is imperative that multislice systems be thoroughly evaluated using a rigorous commissioning process to ensure gel CT images are reliable and of sufficient quality for RT dose measurements.

This chapter presents studies performed to commission a new multislice CT scanner for CT PGD. The variability in N_{CT} associated with the anode heel effect is evaluated and used to define a new background subtraction technique for gel imaging. Relationships between image noise and several imaging parameters are established and the uniformity of CT images is evaluated. The consistency of N_{CT} across image slices is also assessed for each detector configuration. Further analysis is performed to evaluate the variability in N_{CT} across a gel volume due to increasing x-ray tube load as well as the time required for volume scanning. Based on these results, images are collected throughout the volume of an active blank gel to establish a baseline assessment of noise and uniformity in a gel dosimeter before radiation is delivered. Details on the procedures used for each of these experiments are provided in section 6.2, while section 6.3 presents the results and discussion for each study. A summary of the work presented is given in section 6.4.

6.2 Experimental Details

6.2.1 X-ray Computed Tomography Imaging

Commissioning was performed for the Optima CT580 multislice CT scanner described in section 4.4.1. For this study, images were collected with the Optima CT580 system and the HiSpeed Fx/i machine (also described in section 4.4.1) in order to draw comparisons between single and multislice CT systems. All imaging for the active blank study was performed using the Optima CT580 scanner. The 1 L cylinders used throughout this chapter were positioned on the CT couch with the head and neck phantom as described in section 4.4.2 and images were collected using a 25 x 25 cm^2 FOV, 0.49 x 0.49 mm^2 pixel size and the standard reconstruction algorithm. These parameters were shown to provide optimal image quality for imaging large volumes [122] similar to the 1 L cylinders used throughout this work and are not expected to change in going from a single slice machine to a multislice CT scanner. Additional details on CT imaging for each experiment are provided below.

Commissioning Studies

All commissioning studies were performed using a 1 L cylinder filled with water at room temperature. A reference protocol was defined for imaging the cylinder on the multislice scanner that contained, as closely as possible, the same parameters used to image 1 L cylinders on the single slice machine. These parameters are indicated in table 6.1 in bold and were chosen based on recommendations for gel imaging using a single slice system [122]. The protocol differs between the two scanners in that 8 images are acquired simultaneously using 2.5 mm slice thickness on the multislice system, while on the single slice scanner 1 image is acquired using 3 mm slice thickness. All other imaging parameters were the same for both systems and images for all studies were collected using axial mode of acquisition unless otherwise indicated.

As a starting point for commissioning, the reference protocol was used to assess the impact of the anode heel effect, described in section 2.2.1, on the variability in N_{CT} between image slices acquired simultaneously. A set of 25 test images were collected through the centre of the 1 L cylinder at each of the 8 slice positions in the detector array. An additional set of 25 images were also collected using the same protocol to examine slice-by-slice background subtraction. This new background subtraction

technique is described in detail in section 6.2.2.

Further imaging was performed to establish relationships between image noise and several of the available imaging parameters, including the tube voltage and current, gantry rotation time and slice thickness. For this study, one test image was acquired through the centre of the 1 L cylinder at each slice location in the detector array using protocols that independently varied each scanning parameter summarized in table 6.1 from the reference protocol (indicated in bold). An additional set of background images were acquired using each protocol for slice-by-slice background subtraction. This data was also used to examine image uniformity and the consistency of N_{CT} across image slices for each slice thickness and its associated detector configurations. In addition, a set of 25 images were collected using the reference protocol on both the single and multislice systems to compare the image noise and uniformity associated with each machine during a typical CT PGD experiment.

Parameter	Values examined on the Optima CT580 Scanner
Tube voltage (kV)	80, 100, **120**, 140
Tube current (mA)	100 150 **200** 250 300 330
Gantry rotation time (s)	0.5, 0.6, 0.7, 0.8, 0.9, **1**, 2, 3, 4
Slice thickness (mm)	0.625, 1.25, **2.5**, 3.75, 5, 7.5, 10
Field of view (cm^2)	**25 x 25**
Reconstruction algorithm	**Standard**

Table 6.1: The imaging parameters independently varied from the reference protocol (shown in bold) to examine image noise for the Optima 580CT multislice scanner. Note that images were also acquired for the different detector configurations available for each slice thickness.

Following evaluation of image noise and uniformity, the reference protocol was used to examine the tube load characteristics of the new multislice system. For this study, a set of 25 images were collected for each of 48 adjacent image slices along the length of the 1 L cylinder ($\sim$12 cm long), resulting in 1200 test images in total. With data for 8 image slices collected simultaneously, this required 6 independent, 20 mm wide array acquisitions at 6 distinct couch positions to image the entire length of the cylinder. An additional set of 1200 images were collected using the same protocol for background subtraction. The experiment was then repeated using cine mode of acquisition (described in section 2.2.2). A set of 525 images were also acquired at 21 slice locations on the single slice scanner for comparison with the multislice machine.

Active Blank Study

For the active blank investigation, a polymer gel was manufactured and stored in a 1 L cylinder using the procedures outlined in section 4.1. The gel was not irradiated and remained in the refrigerator for the length of time typically required for the gel to become solid, radiation to be delivered and polymerization to stabilize (i.e. ∼27 hours in total). The gel was then imaged using the reference protocol described above with 25 images acquired at each slice location. A second set of 1200 images were acquired for background subtraction through a 1 L cylinder filled with inactive gel (0.5% NIPAM, 0.5% BIS, 5% gelatin, no THPC) that had been kept in the refrigerator with the active gel.

6.2.2 Image Processing & Data Analysis

All image processing and data analyses were performed using Matlab. Image averaging was performed prior to further image processing for all studies where more than 1 image was acquired for the test and background data sets. To examine the effects of the anode heel effect, a background subtraction was performed using a single slice and a new slice-by-slice technique. Using the single slice method, the averaged test image at the centre of the multislice detector array (slice 5 of 8) was subtracted from the remaining, averaged test images. This procedure was used on the single slice scanner where it was shown to be an effect method for removing artifacts in gel CT images [84]. The new slice-by-slice technique was introduced to account for variations in N_{CT} due to the heel effect and involves subtracting the averaged background image at each slice from the averaged test image at the corresponding slice in the detector array. The processed images for each subtraction method were analyzed by extracting the mean and standard deviation of N_{CT} within a square 50 x 50 pixel ROI at the centre of the 1 L cylinder. Mean N_{CT} were then plotted as a function of slice position (with respect to the CT room coordinate system) and the resulting curve was fit to a linear function to assess the consistency of N_{CT} across the detector array achieved using each background subtraction technique.

For the image noise and uniformity studies, slice-by-slice background subtraction was performed for each data set. The effects of varying tube voltage and current, gantry rotation time and slice thickness on image noise were investigated by computing the standard deviation of CT numbers, $\sigma_{N_{CT}}$, within a 50 x 50 pixel square ROI at the centre of the 1 L cylinder for each processed image. Relationships between

image noise and each parameter were established by plotting $\sigma_{N_{CT}}$ as a function of the parameter values and fitting the resulting curves to a quadratic function. Further analyses were performed to assess the uniformity of one representative CT image collected using the reference protocol by computing the mean and standard deviation of N_{CT} for 36 individual 20 x 20 pixel square ROIs at the centre of the 1 L cylinder and 15 concentric, 3 pixel wide, ring ROIs extending radially over the 1 L cylinder. The standard deviation of mean N_{CT} for each ROI was also computed for the grid and ring analyses for the 8 slices of the array to assess the consistency in uniformity for images acquired simultaneously. Noise and uniformity statistics were also computed for one slice acquired using the reference protocol and 25 images on both the single and multislice scanners to compare the performance of the two systems.

Additional analyses were performed to assess the consistency of N_{CT} across each slice of the multislice detector array for the different slice thicknesses and their associated detector configurations. The square ROI analysis used for the background subtraction study was used to compute the mean and standard deviation of N_{CT} for the same processed images used to evaluate the dependence of image noise on slice thickness. Mean N_{CT} were plotted as a function of slice position for each slice thickness to illustrate differences between individual slices in a given array acquisition and between arrays collected with different detector configurations. The range of N_{CT} and $\sigma_{N_{CT}}$ (maximum - minimum value) were also computed for each slice thickness and detector configuration where more than one slice is acquired simultaneously.

For the x-ray tube load study, slice-by-slice background subtraction was performed using a central array within the set of test images and an entire volume of background images. The square ROI analysis described above was employed to extract the mean and standard deviation of N_{CT} from the centre of the 1 L cylinder for each processed image. Mean N_{CT} were plotted as a function of slice position to assess the variability in N_{CT} associated with tube load when imaging the full length of a 1 L cylinder. Consistency data for each individual array (i.e. data from 8 slices) were fit to a linear function to evaluate the variability in N_{CT} due to changes in the anode heel effect caused by increasing x-ray tube load. At this stage, the mean N_{CT} values for the entire length of the 1 L cylinder were fit to a linear function for measurements made using both the single and multislice scanners to compare the tube load characteristics of each machine.

For the active blank study, slice-by-slice background subtraction was performed using a separate set of background images acquired over the volume of an inactive 1

L gel. The resulting images were then filtered using an adaptive mean filter (3 x 3, n = 1) and remnant artifact removal using a span = 5, degree = 3 and 2 iterations. Similar to the studies described above, the square ROI analysis was used to plot mean N_{CT} as a function of slice position to assess the consistency in N_{CT} over the entire volume of the active gel. The uniformity of gel CT images was assessed over the length of the 1 L cylinder using the grid and ring ROI analyses outlined for scanner commissioning. Uniformity was also evaluated using row and column profiles. Seven adjacent N_{CT} profiles were extracted through the diameter of the 1 L cylinder at 5 slice locations spaced 3.5 cm apart along the length of the cylinder. Each profile was 190 pixels long and 1 pixel wide. The mean and standard deviation of N_{CT} were then computed over the 7 pixels in the perpendicular direction of the profiles for both the row and column data.

6.3 Results & Discussion

6.3.1 Background Subtraction

The consistency of N_{CT} across 8 slices acquired simultaneously using the multislice scanner is illustrated in figure 6.1 for images processed using (a) no background subtraction, (b) background subtraction using a single slice and (c) background subtraction using the new slice-by-slice technique. Error bars represent the standard deviation of N_{CT} at the centre of the 1 L cylinder. It is readily seen that significant variability in N_{CT} is present due to the anode heel effect when no background subtraction is employed and that this variability remains after background subtraction using a single slice from the centre of the array. Using the new slice-by-slice background subtraction method, the variability in N_{CT} is effectively removed. This can also be seen from the linear fit parameters computed for each subtraction method summarized in Table 6.2 along with the corresponding 95% confidence bounds. No change in the slope of the consistency data is observed when going from no background subtraction to background subtraction performed using a single slice. However, using the new slice-by-slice technique, the slope is reduced by an order of magnitude and is consistent with a horizontal line.

Based on the results of figure 6.1 and the computed fit parameters summarized in table 6.2, it is recommended that background subtraction be performed using the slice-by-slice technique when acquiring gel images using a multislice CT scanner. This

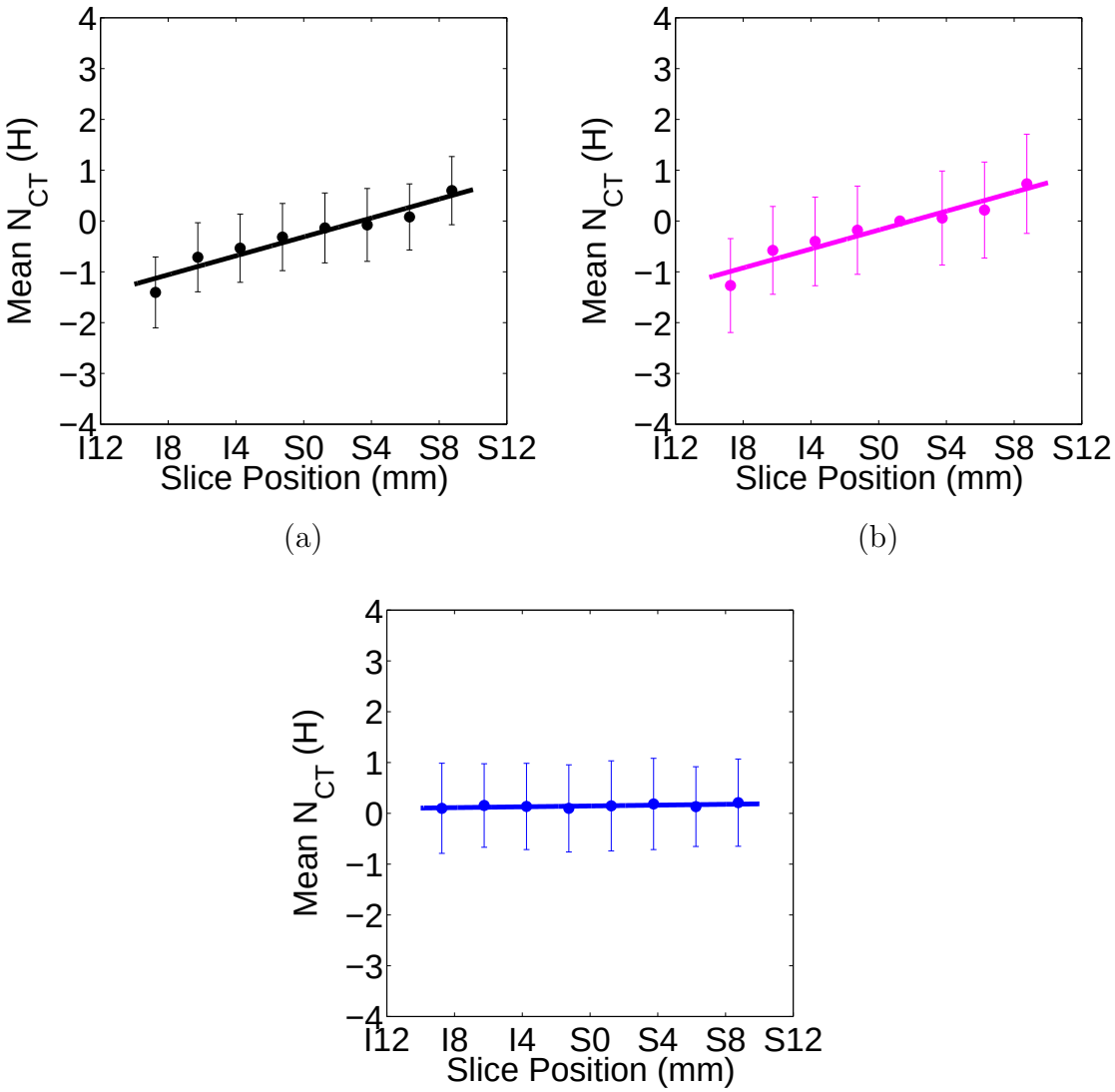

Figure 6.1: The consistency of N_{CT} across 8 slices acquired simultaneously using the multislice scanner for images processed using (a) no background subtraction, (b) single slice background subtraction and (c) background subtraction using the new slice-by-slice technique. Error bars represent the standard deviation of N_{CT} at the centre of the 1 L cylinder. The data are fit to a linear function for each background subtraction technique.

method of background subtraction effectively accounts for variations in N_{CT} that may otherwise introduce systematic variations in gel CT measurements. This finding also represents a major change in the CT PGD process as multiple background images must be acquired when using a multislice CT scanner but a single background image may be used when using a single slice scanner. It is not expected that the additional imaging required for slice-by-slice background subtraction will introduce an additional time burden on scanning as the time required to collect image data is significantly reduced using a multislice system. Further discussion on the time requirements for CT PGD using a multislice scanner is given in section 6.3.4.

Background Subtraction	Slope (H/mm)	Intercept (H)
None	0.09 ± 0.03	-0.3 ± 0.2
Single slice	0.09 ± 0.03	-0.2 ± 0.2
Slice-by-slice	0.004 ± 0.005	0.15 ± 0.03

Table 6.2: The linear fit parameters computed from the mean N_{CT} vs slice position data for each subtraction method.

6.3.2 Noise & Uniformity

Figure 6.2 illustrates the effects of varying the (a) x-ray tube voltage (kV), (b) tube current (mA), (c) gantry rotation time (Δt) and (d) slice thickness (Δx) on CT image noise for the multislice scanner. Relationships were established between image noise and the scanning parameters investigated by fitting each curve in figure 6.2 to a quadratic function. As tube voltage increases, CT image noise decreases by $\sim(\text{kV})^{-1.2}$ while as tube current increases the image noise decreases by $\sim(\text{mA})^{-0.5}$. Similarly, image noise was found to depend on the gantry rotation time and slice thickness as $\sim(\Delta\text{t})^{-0.5}$ and $\sim(\Delta\text{x})^{-0.5}$, respectively. These relationships agree with those reported for the single slice scanner [122] with the exception of tube voltage which has a smaller impact on image noise for the multislice system. However, as for the single slice machine, tube voltage has the greatest influence on CT image noise compared to the other available scanning parameters. As such, the recommendations proposed for reducing image noise for CT PGD using a single slice machine can be applied to the multislice system. Specifically, as the x-ray tube load depends on the tube voltage, current and gantry rotation time equally, the most efficient way to reducing noise in gel CT images is to increase the x-ray tube voltage.

In addition to noise, image uniformity was assessed for one representative slice in

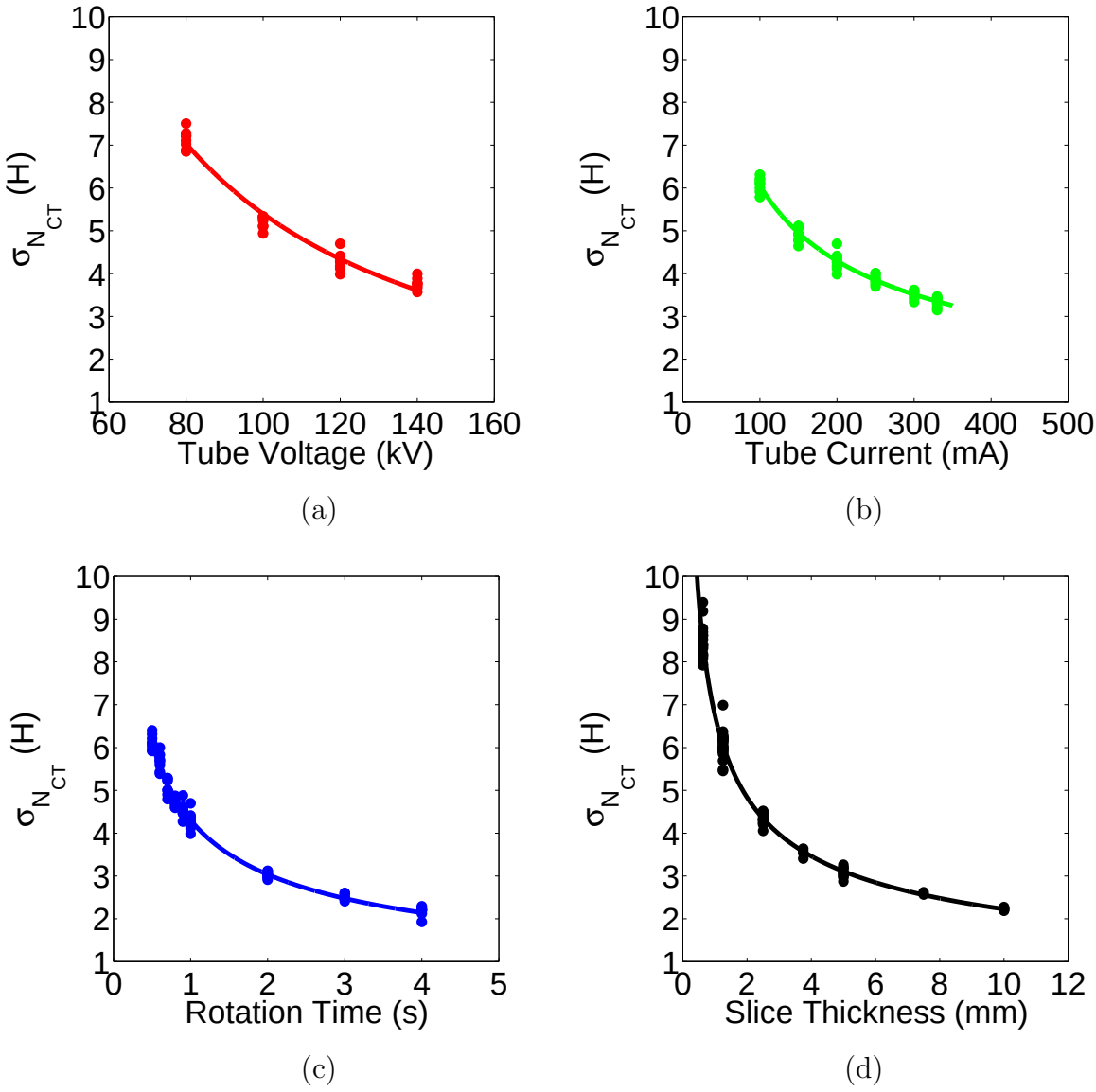

Figure 6.2: The effects of varying the (a) x-ray tube voltage, (b) tube current, (c) gantry rotation time and (d) slice thickness on CT image noise for the multislice scanner. The data are fit to a quadratic function for each parameter examined.

the multislice detector array. Figure 6.3 illustrates the mean and standard deviation of N_{CT} for (a) 36 individual square ROIs at the centre of the 1 L cylinder and (b) 15 concentric ring ROIs extending radially over the 1 L cylinder. It is clear from these plots that image uniformity is excellent as both the mean N_{CT} and $\sigma_{N_{CT}}$ are consistent throughout the 1 L cylinder. The uniformity across the multislice detector array was also evaluated by computing the standard deviation of mean N_{CT} from each ROI for 8 image slices using both the grid and ring ROI analysis techniques. It is readily seen that image uniformity is consistent throughout the detector array as both the grid and ring standard deviations agree to within 0.4 H. The excellent image uniformity found for the multislice scanner using both grid and ring ROI analyses indicates CT measurements using the new system are spatially uniform and reliable for CT PGD.

In addition to the experiments described above, noise and uniformity were compared between the single and multislice scanners. For this study, the reference protocol was used to collect 25 images for one slice on each machine. Table 6.4 summarizes the noise and uniformity metrics obtained from these measurements. The noise associated with the multislice machine is slightly higher than that obtained for the single slice machine. This may be due to the thinner slice thickness used by the multislice scanner (2.5 mm vs. 3 mm) or the additional scattered radiation associated with the cone beam x-ray system employed by the multislice machine. Similarly, no significant differences in image uniformity were found between the two systems. These results indicate the single and multislice scanners can be used interchangeably with respect to image noise and uniformity.

Image Quality	Single Slice	Multislice
Noise (H)	0.5	0.9
Grid Uniformity (H)	0.04	0.07
Ring Uniformity (H)	0.05	0.06

Table 6.3: Noise and uniformity for one image slice (25 averages) for the single and multislice CT scanners.

6.3.3 Multislice Detector Array

The variability in N_{CT} across the slices of the multislice detector array is illustrated in figure 6.4 for slice thicknesses ranging from 0.625 - 10 mm and their associated detector configurations. Error bars represent the standard deviation of N_{CT} at the centre of the 1 L cylinder. The 3.75 mm and 7.5 mm data were plotted together as

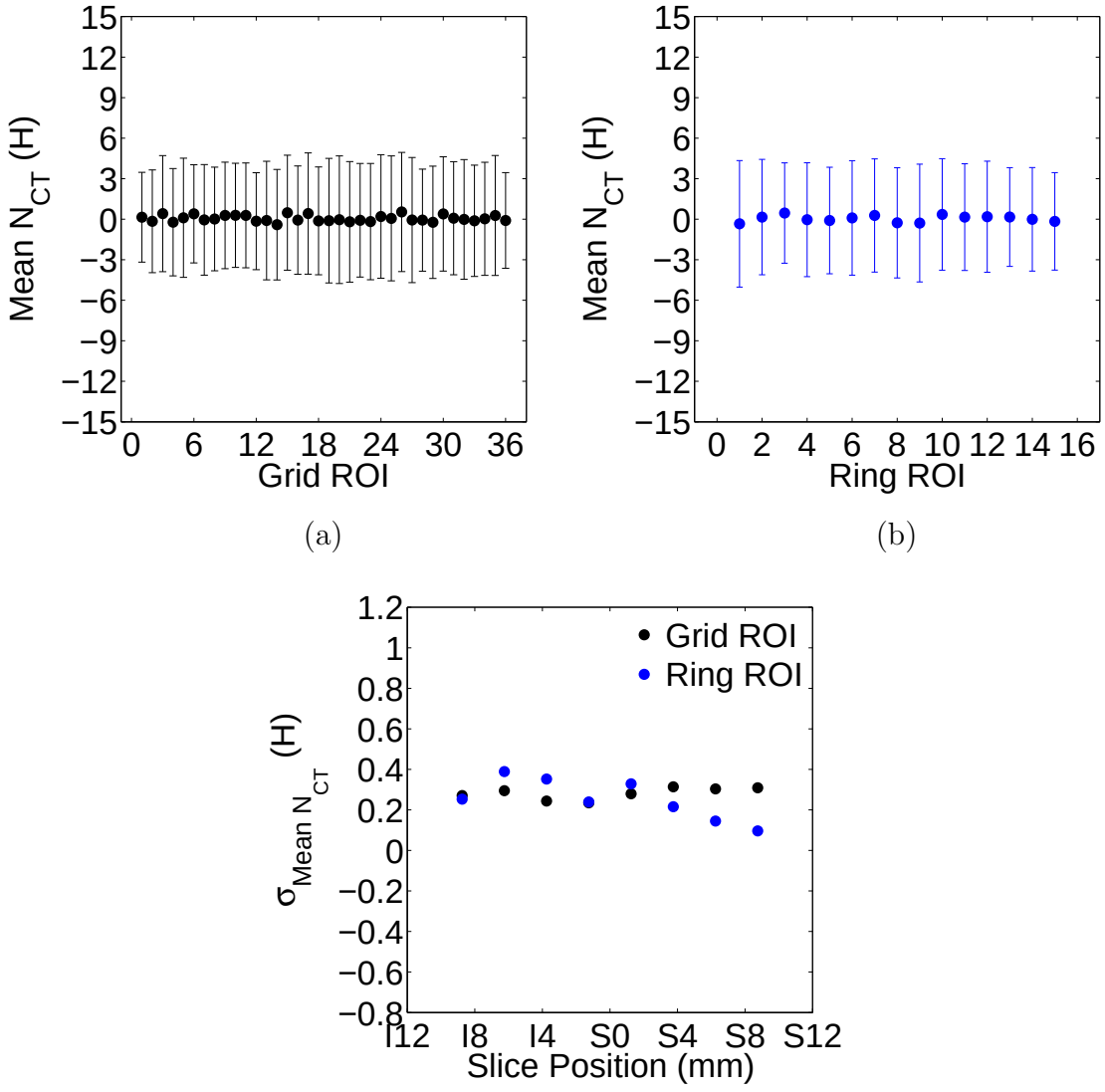

Figure 6.3: Image uniformity within a single CT image computed using (a) grid and (b) ring ROI analyses as well as (c) the uniformity across 8 image slices in the multislice detector array.

only one detector configuration is available for each slice thickness. It is clear from these plots that both the N_{CT} and noise ($\sigma_{N_{CT}}$) associated with each image slice collected using a given detector configuration are consistent across the array for all available slice thicknesses. Mean N_{CT} and $\sigma_{N_{CT}}$ are also consistent for image slices acquired using different detector configurations for the same slice thickness, with the exception of 0.625 mm, where a small offset in N_{CT} is observed between the 2i and 16i data. These results can also be seen by examining the range of N_{CT} and $\sigma_{N_{CT}}$ values for each detector configuration and slice thickness summarized in table 6.4. While the range of N_{CT} and $\sigma_{N_{CT}}$ increases as the number of images in the array increases, no significant differences in range values are observed when the same number of slices are acquired simultaneously using different detector configurations.

The wider range of N_{CT} and $\sigma_{N_{CT}}$ values observed as the number of images in the array increases is likely due to the increase in image noise that results from the additional scattered radiation associated with a larger cone beam of x-rays. As image noise also increases as slice thickness decreases, this effect is more pronounced for the 0.625 mm data. Nevertheless, the results presented here indicate excellent consistency across the detector array for all slice thicknesses, further supporting the removal of the anode heel effect using slice-by-slice background subtraction and indicating multiple images of a gel dosimeter can be reliably acquired simultaneously using various slice thicknesses. These results also indicate the detector configurations for slice thicknesses between 1.25 - 10 mm can be used interchangeably, allowing some flexibility in the number of images acquired simultaneously for a given experiment.

6.3.4 Tube Load

The consistency in N_{CT} over the volume of the 1 L cylinder is shown in figure 6.5 for images acquired using (a, b) axial and (c, d) cine mode of acquisition. Figures 6.5a and c illustrate the mean N_{CT} for images processed using slice-by-slice background subtraction with a central array, while for figures 6.5b and d, slice-by-slice background subtraction was performed using an additional volume of background images. Error bars represent the standard deviation of N_{CT} at the centre of the 1 L cylinder. It is readily seen that mean N_{CT} measured over the volume of the 1 L cylinder agree within uncertainty for all acquisition modes and background subtraction methods. Additional analyses were performed to assess the variability in N_{CT} due to changes in the anode heel effect caused by increasing x-ray tube load by fitting the consis-

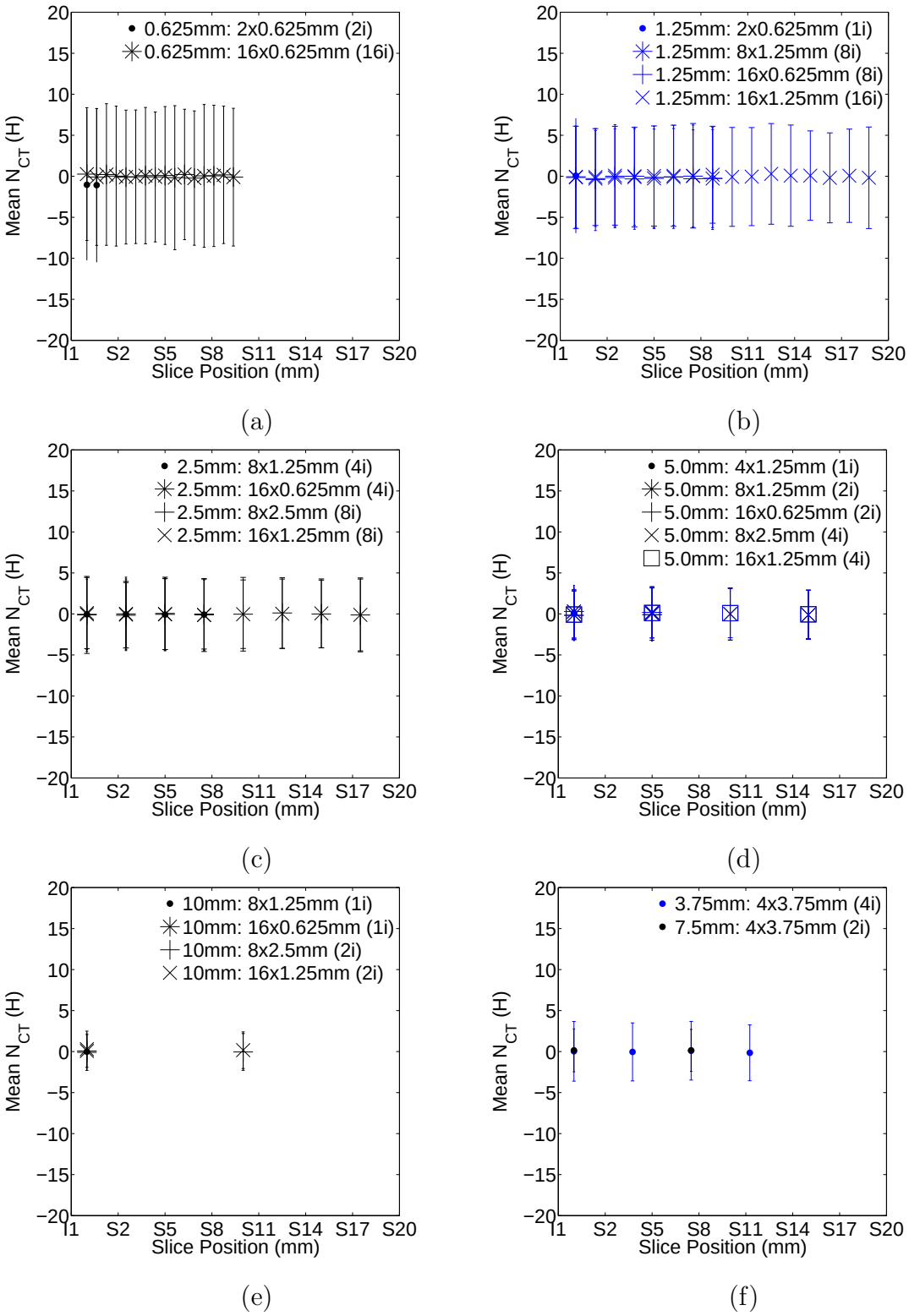

Figure 6.4: The mean N_{CT} measured across the multislice detector array for slice thicknesses of (a) 0.625 mm (b) 1.25 mm (c) 2.5 mm (d) 5.0 mm (e) 10.0 mm and (f) 3.5 mm and 7.5 mm and their associated detector configurations.

Slice Thickness (mm)	Images	Detector Configuration	N_{CT} Range (H)	$\sigma_{N_{CT}}$ Range (H)
0.625	2	2 x 0.625 mm	0.03	0.21
	16	16 x 0.625 mm	0.48	0.86
1.25	1	2 x 0.625 mm	0.00	0.00
	8	8 x 1.25 mm	0.30	0.37
	8	16 x 0.625 mm	0.40	0.35
	16	16 x 1.25 mm	0.48	0.92
2.5	4	8 x 1.25 mm	0.04	0.11
	4	16 x 0.625 mm	0.12	0.26
	8	8 x 2.5 mm	0.28	0.71
	8	16 x 1.25 mm	0.24	0.45
3.75	4	4 x 3.75 mm	0.26	0.23
5.0	1	4 x 1.25 mm	0.00	0.00
	2	8 x 1.25 mm	0.11	0.12
	2	16 x 0.625 mm	0.07	0.14
	4	8 x 2.5 mm	0.17	0.27
	4	16 x 1.25 mm	0.20	0.18
7.5	2	4 x 3.75 mm	0.01	0.05
10	1	8 x 1.25 mm	0.00	0.00
	1	16 x 0.625 mm	0.00	0.00
	2	8 x 2.5 mm	0.05	0.05
	2	16 x 1.25 mm	0.12	0.03

Table 6.4: The range of N_{CT} and $\sigma_{N_{CT}}$ across the slices of the multislice detector array for each slice thickness and its associated detector configurations.

tency data to a linear function for the individual arrays in each data set. Figure 6.6 illustrates the linear fit parameters computed for the individual arrays in each study. The slope of the linear fit for each array (shown in figure 6.6a) falls within ± 0.1 H and there is less than 0.5 H variability in the computed intercepts (figure 6.6b) across the arrays for all acquisition modes and background subtraction methods. Together, these findings reveal increasing x-ray tube load does not significantly influence N_{CT} when imaging large volumes with the multislice scanner.

The results of figures 6.5 and 6.6 indicate volume scanning can be performed with the multislice system using either axial or cine mode of acquisition. However, based on the tube cooling requirements of the scanner, it is clear that axial mode provides a more stable method of imaging. During each scanning session, CT images were collected over the volume of the 1 L cylinder twice. The scanner was then instructed to perform the same acquisition a third time to qualitatively assess the x-ray tube load by determining how soon tube cooling would be required after acquisition of 2 volumes. While no tube cooling period was required at any point during scanning of a third volume using axial mode of acquisition, the scanner indicated a cooling period would be needed after collecting 7 images in cine mode. Based on this information and the fact that the tube will suffer wear over its lifetime and therefore may require tube cooling earlier in a given scanning session, it is recommended that CT scanning of large volumes be performed using axial mode of acquisition.

The results found here also show that slice-by-slice background subtraction can be effectively applied using a single central array of test images or an additional volume of background images. Background subtraction using a central array is the preferred background subtraction procedure as it allows both test and background CT images to be acquired from the same gel dosimeter which can significantly reduce scan time. However, as both calibration and test dose distributions are delivered to the same cylinder, the central region of the gel is exposed to a low dose of scattered radiation that can vary significantly across the central region. This does not pose a problem when using a single slice scanner as one background slice is subtracted from each test slice and the scattered dose influences each slice in the same way. When using the multislice scanner, variations in the scatter dose across background slices from a central array could cause significant differences in N_{CT} between processed images. Differences in mean N_{CT} of up to 20% were found across the central array using a representative gel dosimeter irradiated with both calibration and test irradiations. As such, it is recommended that slice-by-slice background subtraction be performed

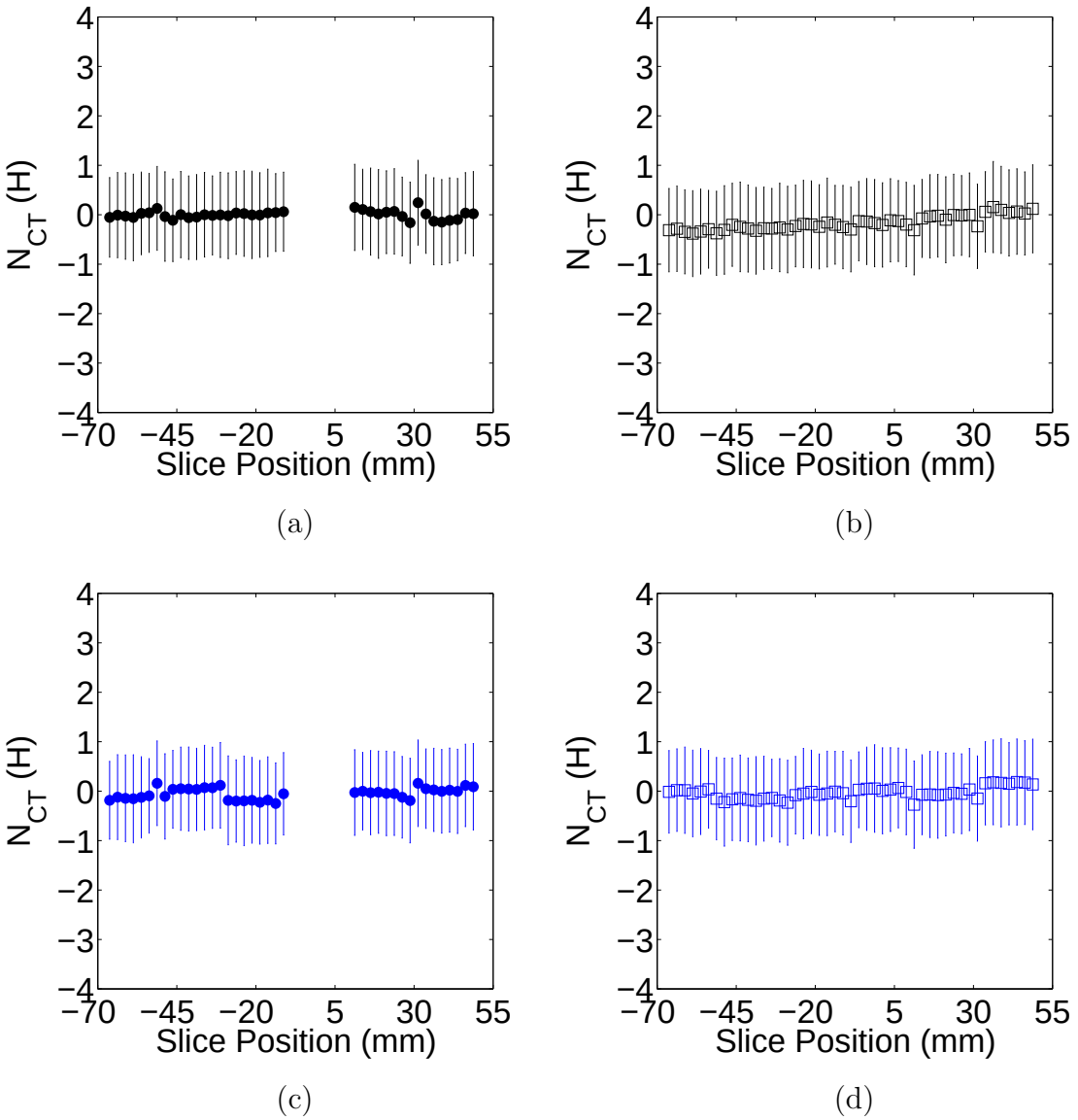

Figure 6.5: Tube load for images collected using axial (a, b) and cine (c, d) mode of acquisition. Slice-by-slice background subtraction was performed using a central array of test images in (a) and (c) and a separate volume of background images in (b) and (d).

using a separate set of images acquired over the volume of a blank gel.

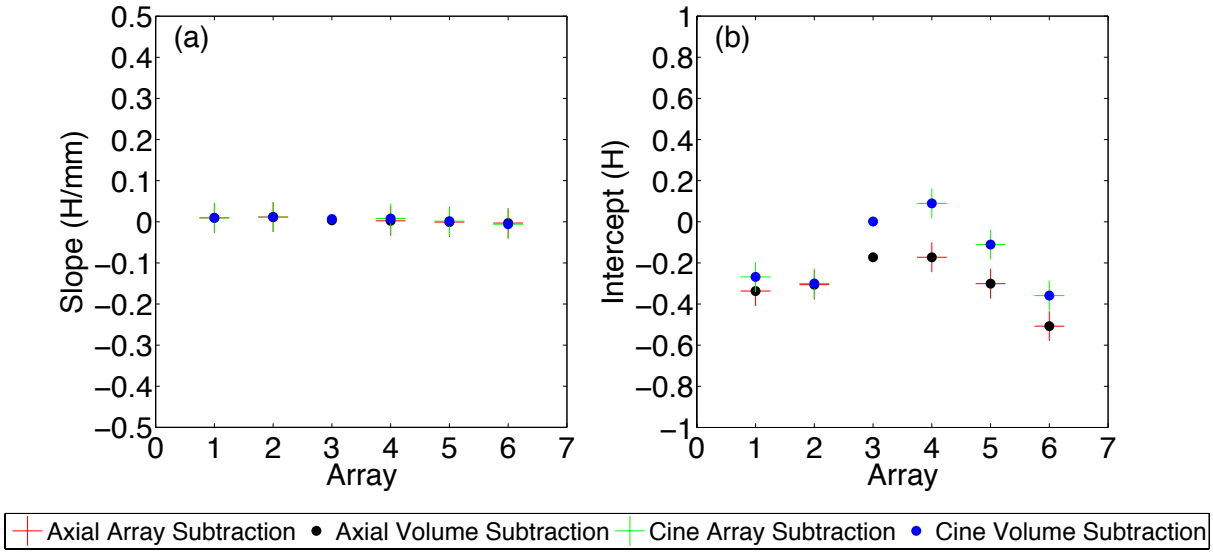

Figure 6.6: The (a) slope and (b) intercept computed for each individual array for the data shown in figure 6.5.

Based on the recommendations given here, a comparison was made between the tube load characteristics of the single and multislice scanners. Figure 6.7 shows mean N_{CT} plotted as a function of sequential slice number for both the (a) single slice and (b) multislice scanners. Data were collected using the reference protocol and 25 images were averaged at each slice location. The first set of averaged images was subtracted from the remaining averaged images for the single slice scanner and slice-by-slice background subtraction using an additional volume of images was used for the multislice data. Tube cooling for the single slice machine limited the number of slices that could be acquired using that system (21 slices or ∼6 cm of the cylinder were imaged). Each data set was fit to a linear function to assess the tube load over the entire scanned volume. For the single slice machine, the mean CT number varies as $N_{CT_1} = 0.2 \times slice + 0.2H$ while for the multislice machine, the CT number changes as $N_{CT_2} = -0.009 \times slice + 0.05H$ as the number of averaged slices increases. It is clear from the slope vales computed that the multislice system provides a superior imaging tool compared to the single slice machine in terms of the x-ray tube load characteristics. In addition, the scan time associated with the multislice system is significantly reduced compared to the single slice scanner. Using the single slice machine, imaging ∼6 cm of the 1 L cylinder with 25 images at each slice position re-

quires over 56 minutes while scanning the entire 12 cm length of the cylinder twice (to include volume background subtraction) using the multislice system requires only 10 minutes. As such, an approximately 4 fold increase in scanning efficiency is achieved in using the multislice system.

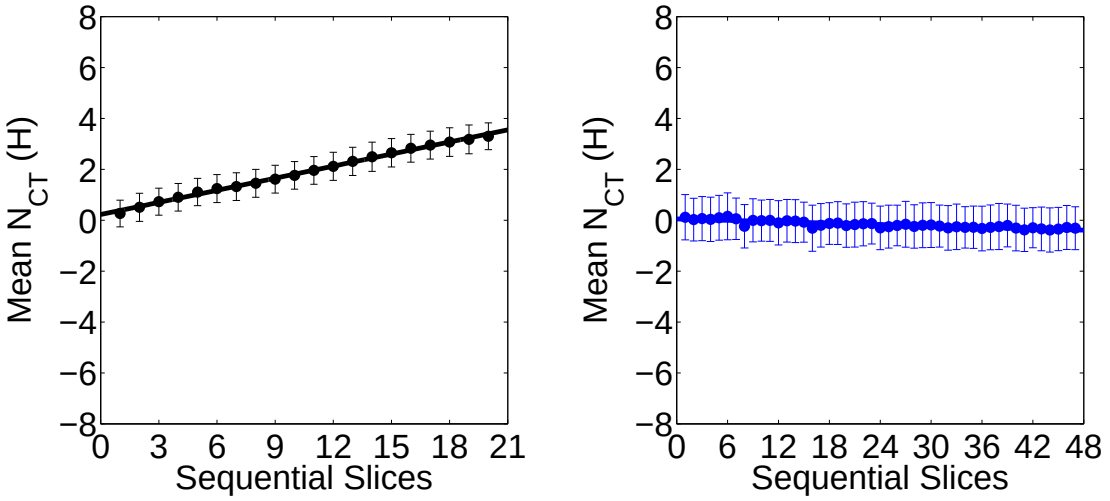

(a) (b)

Figure 6.7: The tube load associated with (a) the single slice scanner and (b) the multislice system when images are acquired using the reference protocol and 25 image averages.

6.3.5 Active Blank Gel

Figure 6.8 illustrates the consistency in (a) N_{CT}, (b) image uniformity computed using grid ROI analysis and (c) uniformity determined using ring ROIs over the length of the active gel. Slices acquired near I60 correspond to the top of the 1 L cylinder (i.e. the region closest to the lid) while slices collected near S60 are located near the bottom of the cylinder. It is clear from figure 6.8a that the consistency in N_{CT} is excellent over most of the active gel as mean N_{CT} agree within uncertainty (standard deviation of N_{CT}) for all image slices between I56.25 - S56.25. However, beyond S40, mean N_{CT} systematically decrease as the image slices approach the bottom of the cylinder and mean N_{CT} for the last 2 image slices no longer agree with the slices more inferior in the gel. Similar behaviour is observed in the image uniformity computed using both grid and ring ROIs (figure 6.8b and c, respectively). In both cases, the

standard deviation of mean N_{CT} computed for the corresponding ROIs vary by less than 0.2 H over the length of the gel, but image uniformity changes as the image slices approach the bottom of the cylinder. In the case of the grid ROI analysis, there is consistent variability in the standard deviations computed between I56.25 - S23.75, but beyond S23.75, the standard deviations become relatively constant. For the ring ROI analysis, a systematic decrease in the standard deviations is observed over the entire length of the cylinder, with a more rapid decrease seen beyond S40, similar to the mean N_{CT} data. These findings indicate the N_{CT} and image uniformity for an active, unirradiated gel are consistent across all image slices collected inferior of S40, or equivalently, $\sim$2 cm from the bottom of the cylinder. This is in contrast to the results found for a water-filled cylinder, where the mean N_{CT} are consistent over the entire cylinder indicating this effect is not due to increasing tube load.

Further investigation was performed to evaluate the image uniformity of the active gel using profiles extracted through the diameter of the 1 L cylinder. Figure 6.9 shows N_{CT} maps of the gel with corresponding row and column profiles for slices located at (a, b) I48.75, (c, d) I13.75, (e, f) S21.25 and (g, h) S56.25 along the length of the 1 L cylinder. Error bars represent the standard deviation of N_{CT} computed over 7 pixels in the perpendicular direction of each profile and mean N_{CT} values plotted at -50 mm correspond to the left and top of the 1 L cylinder. Each N_{CT} map shown on the left clearly illustrates N_{CT} decrease radially from the centre of the cylinder for all image slices and the effect is more pronounced for the column profiles extracted vertically through the gel. This is also illustrated in the row and column profiles shown on the right, with differences in N_{CT} between the centre and periphery of the cylinder of up to $\sim$2 H and $\sim$7 H for the row and column profiles, respectively. However, the effect is much less pronounced in the central region of the image collected at the bottom of the cylinder (S56.25). This difference in the image characteristics of the active gel is consistent with the results shown in figure 6.8.

The results of figure 6.8 and 6.9 show that while image uniformity varies across the diameter of the active gel, both N_{CT} and image uniformity (including the observed variability) are consistent for image slices located above $\sim$2 cm from the bottom of the cylinder. It is possible that this may be due to settling of gelatin molecules as the gel solidifies. As such, it may be possible to mitigate this effect by adjusting the fabrication procedure to include agitation of the gel during or immediately before cooling in the refrigerator. Nevertheless, the cause of the variability in N_{CT} over the diameter of the gel is presently unknown. The variation in N_{CT} resembles the well-known

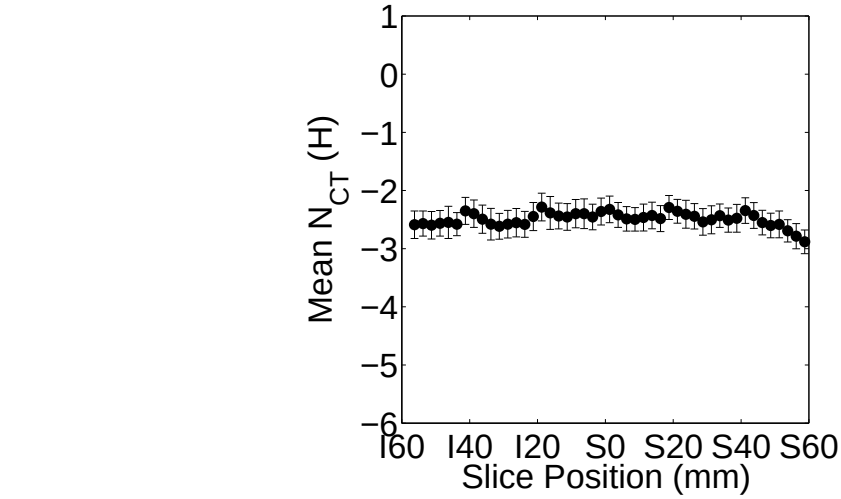

(a)

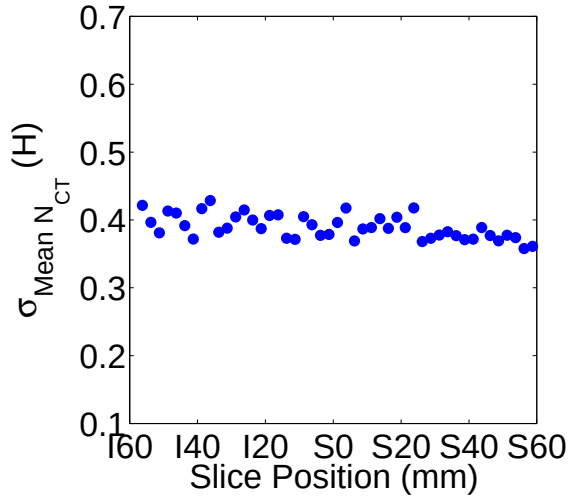

(b)

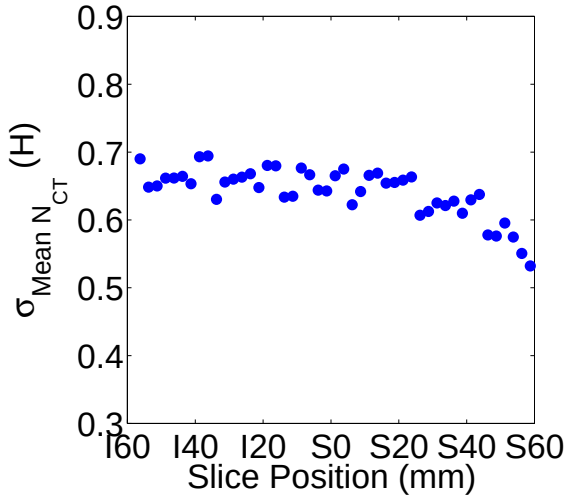

(c)

Figure 6.8: The consistency in (a) mean N_{CT} and uniformity determined using (b) grid ROI analysis and (c) ring ROIs across the volume of the active blank gel.

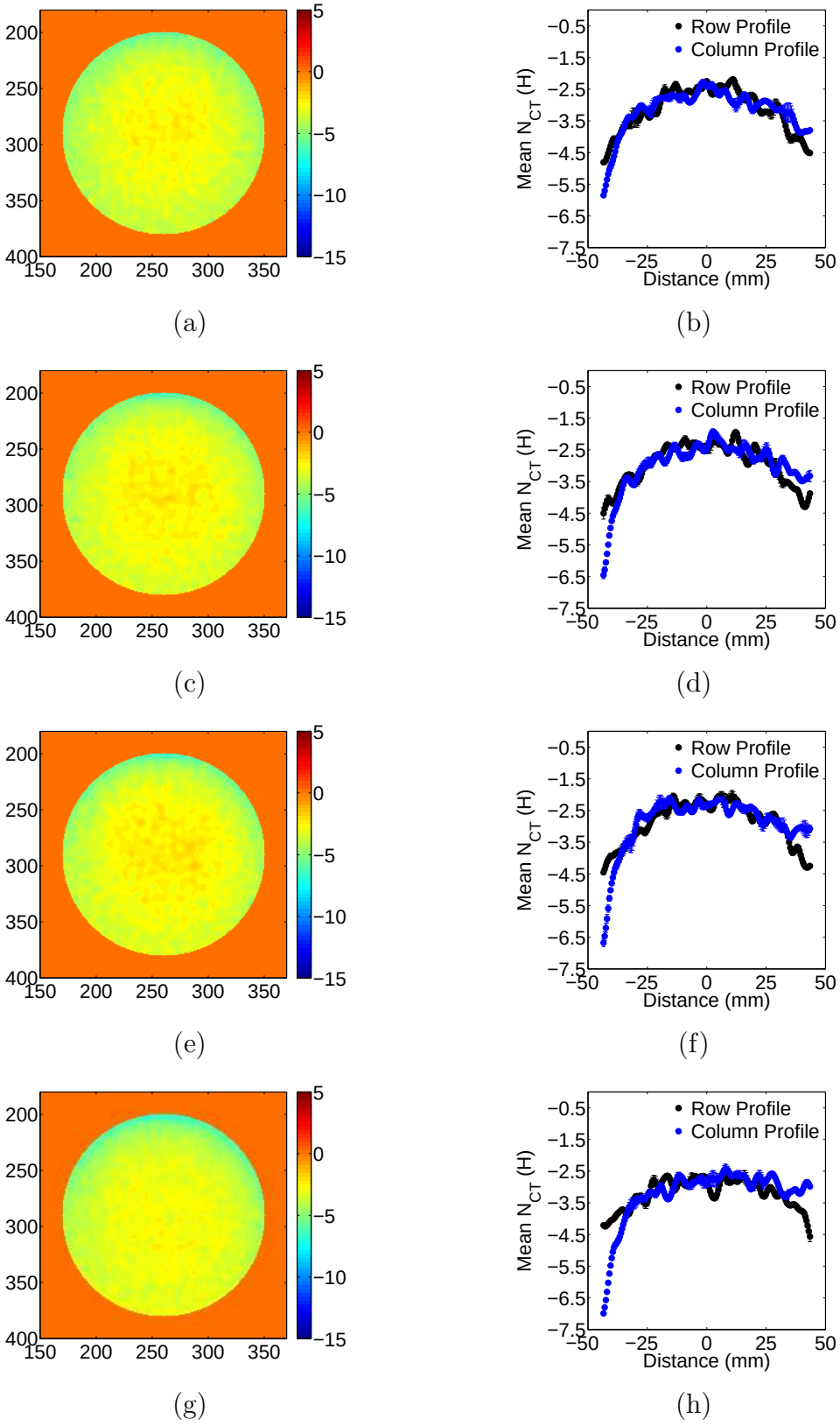

Figure 6.9: Maps of N_{CT} and row and column profiles through the diameter of the active blank gel for images acquired at (a, b) I48.75, (c, d) I13.75, (e, f) S21.25 and (g, h) S56.25

cupping artifact caused by beam-hardening often seen in CT images. However, the excellent image uniformity observed for one slice through a water phantom (section 6.3.2) suggests cupping is not the source of the variability. In addition, consistent with the results shown in figure 6.8, the effect is much less pronounced for the image slice located at the bottom of the cylinder (S56.25). For this reason, it is possible that the variations in N_{CT} seen here are not the result of cupping artifacts but instead may be due to inherent differences in gel density across the diameter of the 1 L cylinder. A recent study by Vandecasteele *et al.* suggests these differences may be due to a temperature gradient extending radially through the diameter of the gel as it sets in the refrigerator. In their study, a temperature gradient of $\sim$2.8°/cm was intentionally applied across an nPAG gel as it solidified. The gel was not irradiated and images collected using MRI showed differences of up to 10.9% in the R_2 map of the gel across where the gradient had been applied. The observed differences are attributed to an interaction between gelatin and the antioxidant in the gel system. As it has been shown that THPC can react with gelatin to increase the cross-linking of the gelatin matrix in unirradiated gels [176], thereby increasing the density of the gel, it is believed a similar phenomenon may be contributing to the discrepancies observed here.

6.4 Chapter Summary

This chapter presents work undertaken to commission a new multislice CT scanner for CT PGD and provides important information about imaging polymer gels using a multislice system. A new slice-by-slice background subtraction technique was developed to remove image artifacts that involves subtracting the background image at a given slice from the test image at the corresponding slice in the detector array. This technique was found to effectively remove variations in N_{CT} due to the anode heel effect and is the recommended method for performing background subtraction when images are acquired using a multislice scanner. Further study revealed the relationships between image noise and the x-ray tube voltage and current, gantry rotation time and slice thickness are consistent with those found for single slice machines with the exception of tube voltage which has less influence on noise for the multislice system. This finding, combined with the consistent noise and uniformity characteristics found between single and multslice systems, indicate these scanners can be used interchangeably and the recommendations for optimizing image quality for CT PGD

using a single slice machine also apply to multislice CT systems. In addition, N_{CT} and image noise were found to be consistent for image slices acquired simultaneously using the multislice detector array for all slice thicknesses and their associated detector configurations, indicating multiple images can be reliably collected at the same time. It was also found that the detector configurations for slice thicknesses between 1.25 - 10 mm can be used interchangeably, allowing some flexibility in the number of images acquired simultaneously for a given experiment. Additional work was performed to examine the effects of x-ray tube load which was determined to have a negligible influence on N_{CT} when imaging large gel volumes. Due to the tube load associated with cine scanning and the scattered radiation dose delivered to the centre of a gel in a typical CT PGD experiment, it is recommended that volume imaging be performed using axial mode of acquisition and slice-by-slice background subtraction with a separate set of background images. Using these recommendations, imaging a large gel volume with the multislice system reduces the scanning time by up to 4 times when compared to imaging using the single slice machine. Finally, images of an active blank gel that was not irradiated indicate deviations in N_{CT} occur at the bottom of the 1 L cylinder that may be due to settling of gelatin molecules and N_{CT} can vary across the diameter of the cylinder by up to 7 H. Possible strategies to reduce this variation include agitating the gel during setting and increasing the cooling period to reduce the temperature gradient present across the gel during setting.

Chapter 7

Results & Discussion III: Investigation of the Dose Rate Properties of the New Polymer Gel Dosimeter

7.1 Introduction

This chapter presents studies performed to further investigate the dose rate properties of the new polymer gel dosimeter used throughout this work. Given that a significant dependence on machine dose rate was found for the new formulation in chapter 5, the implication for variations in other types of dose rate must be examined. Compensation strategies can then be designed for the gel to avoid dosimetric errors caused by dose rate variations that may occur during clinical application. A manuscript on this material is currently in preparation for submission to the peer-reviewed journal *Physics in Medicine and Biology*.

There are 3 types of dose rate that occur in radiation treatments, namely the machine dose rate, deposited dose rate and mean dose rate. The machine dose rate is the rate at which radiation pulses are delivered by the LINAC and is expressed in MU/min. Modern LINACs are typically equipped with a range of machine dose rates between 100 - 600 MU/min for flattening filtered beams and 400 - 2400 MU/min for flattening filter free beams (see section 4.3.1 for a description of LINAC beam filtering). Each machine dose rate is associated with a radiation pulse repetition

frequency between 60 - 360 pulses per second (pps). For example, machine dose rates of 100 MU/min (filtered) and 400 MU/min (unfiltered) correspond to a pulse repetition frequency of 60 pps, while machine dose rates of 600 MU/min (filtered) and 2400 MU/min (unfiltered) correspond to a pulse repetition frequency of 360 pps. The increase in dose rate associated with the unfiltered beams is due to the presence of high energy photons in the treatment field (low energy photons are removed by the flattening filter for filtered beams delivered at 100 - 600 MU/min). Based on these pulse repetition frequencies, it is readily seen that variations in machine dose rate occur on the millisecond timescale, specifically, between 3 - 17 ms depending on the dose rate chosen.

Unlike the machine dose rate, the deposited dose rate must be referenced to a specific location in a material and is defined as the dose absorbed at that location per unit time. The deposited dose rate is expressed in cGy/min. Similarly, the mean dose rate is the total dose delivered to a specific location in a medium over the time it takes to deliver the entire treatment fraction. The mean dose rate is also expressed in cGy/min and typically varies over timescales on the order of seconds to minutes. The deposited and mean dose rates depend on several factors related to the radiation delivery equipment and technique as well as the phantom itself. The factors associated with radiation delivery, or machine factors, include the machine dose rate, the distance between the radiation source and the material, or source to surface distance (SSD), the number of radiation beams delivered during the treatment session, the beam-on and beam-off duration for each beam and beam modulation. Phantom factors include depth in the material, field size changes with depth and off-axis location in the medium. These factors vary with the shape and size of the object being irradiated and are not considered further.

As a starting point, the studies presented here examine the dependence of gel response on changes in mean dose rate due to variations in machine factors, with the exception of SSD, as this parameter does not vary significantly during a typical, controlled dosimetry experiment or source to axis patient set-up. Initial investigations are performed using gel vials to examine how varying the number of radiation beams and the beam-on and beam-off duration of each beam influence the dose response for gel irradiated to 12 Gy. The intra- and inter-batch reproducibility of the gel vial system is also assessed.

Additional studies are performed to evaluate the dependence of gel response on variations in mean dose rate for a range of doses between 0 - 20 Gy using 1 L gels

irradiated with the 3-field dose distribution described in section 4.3.2. Given that the machine dose rate dependence was found to be more pronounced at higher doses, it is possible that the dose rate dependence may be reduced if using a lower dose range. For this reason, the range of doses examined here is reduced from previous studies. The mean dose rate is varied by increasing the number of radiation beams used to deliver the distribution and by using a sliding window delivery technique. These experiments simulate the types of mean dose rate variations that occur in IMRT treatments due to multiple radiation fields and beam modulation.

Following the mean dose rate experiments, the machine dose rate study is revisited using a gel with increased THPC concentration to determine if additional antioxidant mitigates the observed dose rate effect. This experiment is performed based on the knowledge that THPC can form crosslinks with gelatin in a polymer gel system [176], which may lead to formation of a net or mesh like structure within the gel. This structure may act as a barrier to prevent radicals from coming together and being rendered neutral through termination reactions, a situation that is more probable at higher dose rates, as a greater number of radicals are produced in a given region of gel per unit time. By adding more THPC to the gel system, it is possible that a finer net will be produced and prevent termination reactions that can ultimately lead to a lower dose response at higher dose rates. The machine dose rate experiment is also repeated using a gel fabricated without BIS to determine if NIPAM self-crosslinking, discussed in section 5.3.4, may be contributing to the observed dose rate effect. The reader is referred to that section for a detailed description on the reactions associated with NIPAM self-crosslinking.

Details on the experimental procedures used for each study are given in section 7.2, while section 7.3 provides results and discussion for each experiment. A summary of the work presented in this chapter is given in section 7.4.

7.2 Experimental Details

7.2.1 Vial Studies

For each of the dose rate experiments performed using gel vials, one batch of gel was fabricated (as described in section 4.1.1) and distributed between 10 scintillation vials. The vials were subsequently sealed in acrylic pots and stored in the refrigerator until the gel solidified as outlined in section 4.1.2. Unless otherwise indicated, each vial

was then irradiated individually within its cylindrical pot using the acrylic phantom described in section 4.3.2 on a Truebeam LINAC. A total dose of 12 Gy was delivered to the centre of each vial using one anterior, 10 x 10 cm^2 field at 400 MU/min. A single field was used to minimize changes in mean dose rate between vials that can occur if multiple fields are delivered with varying times between each beam (e.g. parallel-opposed fields). The position of the cubic acrylic phantom was adjusted from isocentre prior to radiation delivery for all studies to ensure an SSD of 75.6 cm. This set-up was determined to provide 1 cGy/MU at the centre of the gel vial using ion chamber measurements described in appendix A. Following radiation delivery, gel vials for all experiments were returned to the refrigerator for a duration of 18 - 24 hours to allow the polymerization reactions to stabilize.

All imaging for the vial studies was performed using the Optima CT580 CT scanner described in section 4.4.1. For each experiment, gel vials were removed from their acrylic pots and placed in the styrofoam phantom described in section 4.4.2. As it was found that the noise and uniformity recommendations for the single slice scanner apply to the multislice machine, the same protocol for imaging vials on the single slice system was used on the multislice scanner (i.e. tube voltage of 120 kV, tube current of 200 mA, 1 second gantry rotation time, soft reconstruction algorithm, 10 mm slice thickness and 16 image averages). An additional set of 16 images were acquired through vials filled with blank gel using an identical protocol for background subtraction. The resulting images for each study were processed as described in section 4.5.1 (span = 4 deg = 3 and 2 iterations for RAR filtering). The mean and standard deviation of N_{CT} within an 8 pixel radius ROI were then computed for each vial and used to determine ΔN_{CT} for each gel. The radius of the ROI was reduced from previous studies to account for the dose gradient introduced by using a single anterior field. Details specific to the mean dose rate and batch reproducibility studies are given below.

Mean Dose Rate Experiments

A set of three experiments were performed using gel vials to investigate the effects of varying the mean dose rate on gel response. The number of radiation beams and/or the beam-on and beam-off duration were varied across the vials of each study to simulate changes in mean dose rate on the order of seconds to minutes that are associated with treatments where multiple fields are used to deliver the total prescribed

dose. For each investigation, one vial was irradiated with a single, unbroken field (i.e. the entire dose was delivered with one beam) to provide a reference measure of gel response.

Table 7.1 summarizes the number of radiation fields, beam-on and beam-off duration of each field and mean dose rate used to irradiate gel vials for the three experiments. For the first study, referred to as the constant mean dose rate (CMDR) experiment, the number of beams varied across the vials, but the mean dose rate was maintained at 200 cGy/min. This was achieved by keeping the beam-on and beam-off times the same for each gel. For example, one vial in the set was irradiated for 30 s, then left for 30 s and so on until a total dose of 12 Gy was delivered.

For the second experiment, referred to as the the variable mean dose rate study where the beam on time changes (VMDR-On), the number of beams varied between the gel vials, but the beam-off time was held at 30 s for all gels. To provide another example, in this situation, one vial was irradiated for 45 s, then left for 30 s, then irradiated for 45 s, and so on until it received 12 Gy. As a result, each vial for this study was irradiated with a different mean dose rate between 133-300 cGy/min.

Finally, for the third experiment, referred to as the variable mean dose rate study where the beam off time changes (VMDR-Off), gel vials were irradiated with 5 beams that were each 36 s in duration, but the beam-off time varied across vials from 12 to 72 s. In this case (to give another example), one vial was irradiated for 36 s then left for 12 s five times until it received 12 Gy. Similar to the VMDR-On experiment, this ensured each vial was irradiated with a different mean dose rate between 133-300 cGy/min.

	CMDR	VMDR-On	VMDR-Off
Number of beams	2, 3, 4, 5, 6, 8, 10, 12	2, 3, 4, 5, 6, 8, 10, 12	5
Beam-on time (s)	15 - 90	15 - 90	36
Beam-off time (s)	15 - 90	30	12 - 72
Mean dose rate (cGy/min)	200	133 - 300	133 - 300

Table 7.1: The number of radiation fields, beam-on and beam-off duration of each field and mean dose rate used to irradiate gel vials for the CMDR, VMDR-On and VMDR-Off studies.

Batch Reproducibility Experiments

Additional experiments were performed to assess the intra- and inter-batch reproducibility associated with the gel vial system. Intra-batch reproducibility was exam-

ined in irradiated gel using a set of vials exposed to 12 Gy using a single, continuous field delivered at 400 MU/min. Further work was performed to investigate the intra-batch reproducibility of unirradiated active gel using a set vials that were not exposed to radiation but remained in the refrigerator for the time typically required for radiation delivery and stabilization of polymerization. In addition to the intra-batch studies, inter-batch reproducibility was assessed for the vial system using 5 batches of gel. For each batch, one vial was irradiated to 12 Gy using a single, unbroken beam. Data for this study were taken from the mean dose rate studies described above, the intra-batch study where gels were irradiated to 12 Gy and an additional, preliminary experiment used to investigate the gel dose response in vials (not reported on here).

7.2.2 1L Gel Dose Response Studies

Experiments were performed using 1 L gels to examine the dependence of gel response on variations in mean dose rate for doses between 0 - 20 Gy. For each study, a polymer gel was manufactured as described in section 4.1.1 and the gel solution was transferred to a 1 L cylinder. Based on the results of chapter 6, each cylinder was flipped upside down in the fume hood for $\sim$15 s before being returned to its upright position to avoid gel settling. Following rotation, all gels were immediately placed in a water bath in the refrigerator and remained in cold storage for 6 - 8 h until solid as described in section 4.1.2. Note that an attempt was made to reduce variations in gel density across the diameter of unirradiated active gel (observed in chapter 6) by cooling the gel more slowly over a 24 h period using a larger water bath. However, this procedure resulted in unreacted monomer precipitating out of the gelatin matrix. As such, no measures were taken to avoid variations in gel density across the diameter of the 1 L gels used in this work.

Once solid, each 1 L gel was irradiated with 6 MV photons using a Truebeam LINAC at 400 MU/min. The 3-field dose distribution described in section 4.3.2 was delivered to the top and bottom of each 1 L gel as for the machine dose rate experiment presented in section 5.2.1. For all experiments, the two distributions were separated by at least 6.5 cm to minimize scattered radiation between neighbouring distributions and an interval of 1 minute was observed between delivery of each radiation field.

Table 7.2 summarizes the number of radiation fields, beam modulation, total dose, total delivery time and mean dose rate (at the reference point of LINAC calibration) associated with the 3-field distributions for each study. For the first experiment, the

3-field plan was delivered to the top and bottom of the cylinder using one beam per field (i.e. 3 fields in total for each distribution) to obtain a baseline measure of gel response at either end of the cylinder. The distributions were delivered with mean dose rates that were consistent to within 30 cGy/min. For the second experiment, the calibration distribution at the bottom of the gel was delivered using 9 beams (3 beams per field) but the irradiation at the top of the gel remained the same as for the baseline experiment. This produced a difference in mean dose rate of 60% between the distributions at top and bottom of the cylinder. A third experiment was then performed where the distribution at the bottom of the gel was delivered using 3 fields that were each modulated using a sliding window delivery technique. This was achieved using the MLC to block all but a 3 cm gap of the radiation field. The gap was translated across the field aperture to produce a uniform distribution that simulated, at the most basic level, changes in mean dose rate associated with IMRT. Similar to the 9-field experiment, the distribution at the top of the cylinder remained the same as for the baseline study. This resulted in the mean dose rate varying between the distributions at the top and bottom of the cylinder by 72%.

	Baseline		9-Field		Sliding Window	
	Top	Bottom	Top	Bottom	Top	Bottom
Number of beams	3	3	3	9	3	3
Beam modulation	No	No	No	No	No	Yes
Total dose (cGy)	2000	2000	2000	2000	2000	2000
Total delivery time (min)	7.9	8.7	7.9	14.7	8.4	18.0
Mean dose rate (cGy/min)	253.8	223.0	253.8	136.1	237.2	111.0

Table 7.2: The number of radiation fields, beam modulation, total dose, total delivery time and mean dose rate for each calibration dose distribution delivered to the top and bottom of the 1 L cylinders used for the baseline, 9-field and sliding window experiments.

Following radiation delivery, the 1 L gels for each study were returned to the refrigerator for 18 - 24 hours to allow the polymerization reactions to stabilize. Imaging was then performed using the Optima CT580 CT scanner described in section 4.4.1. Each gel was positioned on the CT couch using the head and neck phantom as described in section 4.4.2 and images were acquired through the isocentre of each distribution using the reference protocol discussed in chapter 6. As recommended in that chapter, slice-by-slice background subtraction was performed using an additional set of background images acquired at the same slice positions in a blank 1 L gel. The resulting images were processed as described in section 4.5.1 (span = 7, degree = 3

and 2 iterations for the RAR filter) and dose response curves were constructed using the procedures outlined in section 4.5.2 for each distribution.

Based on the results of the mean dose rate investigations described above, the machine dose rate experiment was repeated for two additional 1 L cylinders. Procedures for fabrication, irradiation and imaging of the 2 gels were the same as for the baseline study described above with the except that the machine dose rate was varied for the distributions at the top of each cylinder. For the first gel, the distribution at the top of the cylinder was delivered at 100 MU/min and for the second gel the corresponding distribution was delivered at 600 MU/min. These experiments differ from the original mean dose rate investigation in that the dose rate varies between two gels for the distributions delivered at the top of each cylinder (as opposed to varying within a single gel) and a reference distribution is delivered at 400 MU/min to the bottom of each cylinder (note the reference, or baseline, distribution was delivered to the top of each cylinder for the mean dose rate experiments).

7.2.3 Formulation Experiments

To investigate how changing the gel formulation affects the observed machine dose rate effect, two experiments were performed that attempted to mimic the mean dose rate study used for gel characterization, with the exception that the gel formulation was altered in each case. For the first experiment, the concentration of THPC in the gel system was increased to try to reduce the machine dose rate effect, while for the second experiment, the BIS was removed from the gel system to determine if NIPAM self-crosslinking may be contributing to the cause of the observed dependence.

For each study, a 1 L gel was manufactured using the procedures outlined in section 4.1.1 and stored in the refrigerator until solid as described in section 4.1.2. Table 7.3 summarizes the gel recipes used for each study. For the experiment examining the effects of increasing THPC concentration, the formulation differed from the original gel recipe introduced by Chain *et al.* in that the THPC was increased from 5 mM to 10 mM. The gel used to determine if NIPAM self-crosslinking may be contributing to the observed dose rate effect was similar to the original gel recipe but contained 20% NIPAM and no BIS. Note that while the maximum solubility of NIPAM in water at 34°C was previously reported to be ∼17.8% by weight [44], the NIPAM used in the present work fully dissolved in water at 40°C during gel manufacture.

After solidifying, each gel was irradiated with 6MV photons using the Clinac 21EX

LINAC described in section 4.3.1. Treatment planning, set-up and irradiation were identical to the previous machine dose rate experiment presented in section 5.2.1. Using the head and neck phantom, each gel was positioned at the treatment unit and the 3-field plan was delivered to two regions of gel at 600MU/min and 100MU/min, respectively. The dose distributions were spaced over 6.5 cm apart to minimize scattered radiation between neighbouring distributions. Following irradiation, gels for each study were returned to the refrigerator for 18 - 24 hours to allow the polymerization reactions to stabilize.

Component	THPC study	NIPAM study
Water	75.5%	75%
Gelatin	5%	5%
NIPAM	15%	20%
BIS	4.5%	0%
THPC	10mM	5mM

Table 7.3: Gel formulations used to examine the effects of increasing THPC and NIPAM self-crosslinking on the machine dose rate dependence.

Imaging for both formulation experiments was performed using the Highspeed Fx/i CT scanner described in section 4.4.1. For each study, the 1 L gel was positioned on the CT couch using the head and neck phantom as described in section 4.4.2 and images were acquired through the isocentre of each distribution using the same imaging parameters employed for the characterization mean dose rate experiment (i.e. 120 kV tube voltage, 200 mA tube current, 1 second gantry rotation time, 3 mm slice thickness, standard reconstruction algorithm and 25 image averages). An additional set of 25 images were acquired through the unirradiated region at the centre of the gel for background subtraction. The resulting images were processed as described in section 4.5.1 (span = 7, degree = 3 and 2 iterations for the RAR filter) and used to construct dose response curves as outlined in section 4.5.2.

7.3 Results & Discussion

7.3.1 Vial Studies

The effect of varying the mean dose rate on gel response for gel vials irradiated to 12 Gy is illustrated in figure 7.1. The ΔN_{CT} is plotted as a function of the number of beams used to irradiate each vial for the CMDR and VMDR-On studies in figure

7.1a, while figure 7.1b illustrates the ΔN_{CT} plotted as a function of the mean dose rate used to irradiate each vial for the VMDR-On and VMDR-Off experiments. Error bars represent the standard deviation of ΔN_{CT} measured at the centre of the ROI for each vial. Data plotted with square markers correspond to ΔN_{CT} measures for the reference vials irradiated using one continuous beam at 400 cGy/min. Both plots demonstrate no clear trend in ΔN_{CT} can be identified with respect to the number of beams or mean dose rate for each study. This suggests variations in mean dose rate on the order of seconds to minutes due to changes in the number of beams and the beam on and beam off time do not significantly influence gel response when irradiated to 12 Gy. However, significant variability in ΔN_{CT} is observed for each vial study. This is easily seen in figure 7.2a where ΔN_{CT} are plotted together for each experiment. With the exception of the CMDR investigation, data agree within experimental uncertainty, but ΔN_{CT} vary by 1.2 HU for the VMDR studies and 1.5 HU for the CMDR experiment.

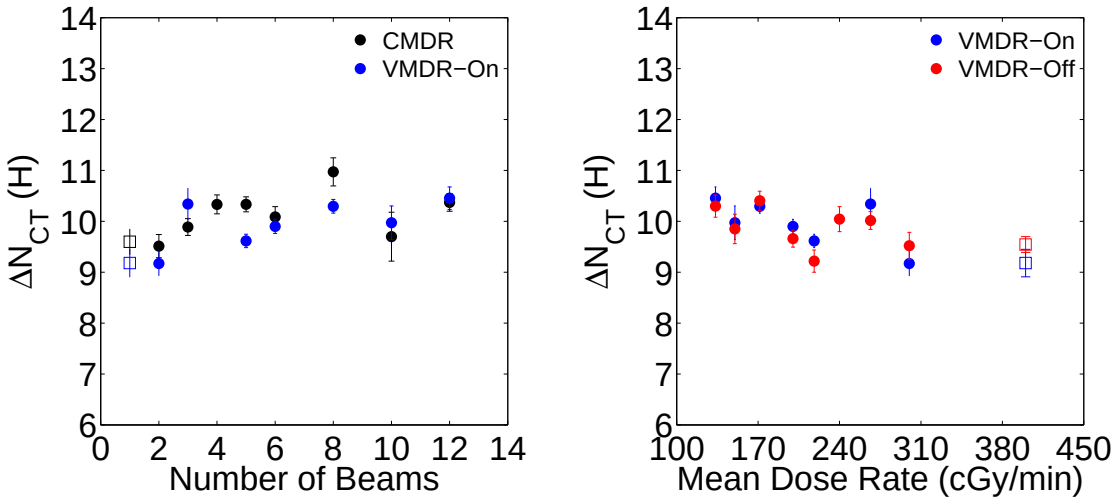

(a) (b)

Figure 7.1: ΔN_{CT} plotted as a function (a) the number of radiation beams used to deliver 12 Gy for the CMDR and VMDR-on experiments and (b) the mean dose rate for the VMDR-on and VMDR-off studies. Square markers correspond to ΔN_{CT} measured for the reference vials irradiated with one continuous beam.

The variability observed for the vial mean dose rate studies can be attributed to poor intra-batch reproducibility for the vial system. Figure 7.2b illustrates ΔN_{CT} plotted as a function of vial number for both unirradiated active gel and unirradiated

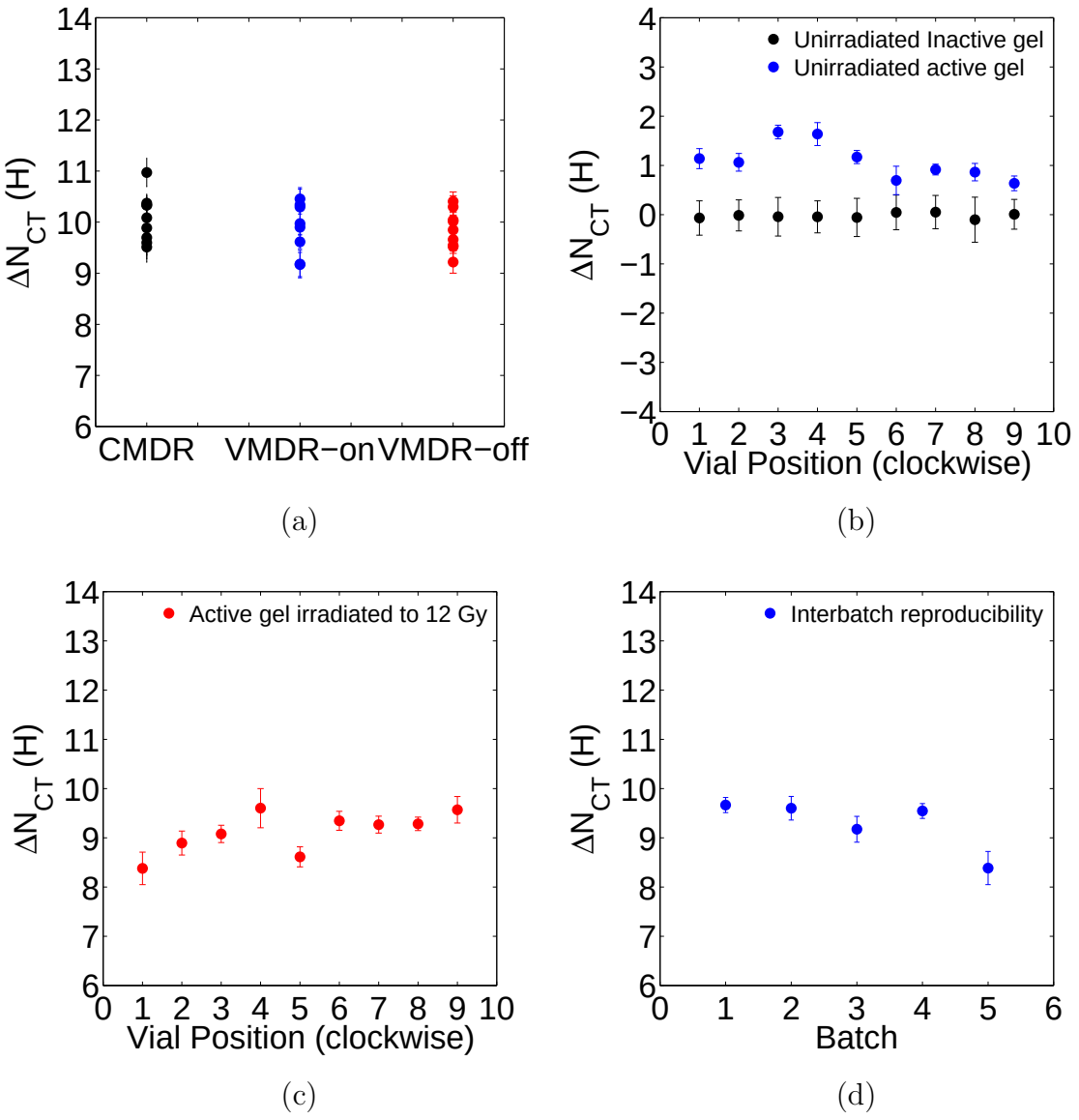

Figure 7.2: (a) ΔN_{CT} for the CMDR, VMDR-On and VMDR-Off studies. (b) Intra-batch reproducibility for unirradiated active and inactive gels. (c) Intra-batch reproducibility for gels irradiated to 12 Gy using one, unbroken field. (d) Inter-batch reproducibility for the vial system.

inactive (i.e. blank) gel vials. While ΔN_{CT} are consistent within experimental uncertainty (standard deviation of ΔN_{CT}) across the vials filled with inactive gel, ΔN_{CT} vary by 1.1 HU across the active vials. Similar variability ($\sim$1.2 HU) is observed across a set of active gel vials each irradiated to 12 Gy using a single continuous beam. The observed variability is also seen across different batches of gel where each vial was irradiated to 12 Gy using one, unbroken field. While every effort is made to maintain consistent conditions across the vials for each study, it is possible that the observed variability is due to small differences in the environmental conditions (e.g. temperature) of each gel vial within a given experiment and across different vial studies. Nevertheless, the results found here for the mean dose rate experiments provide evidence that the new gel formulation does not possess a mean dose rate dependence. Further study to investigate the mean dose rate dependence for 1 L gels is provided in section 7.3.2.

7.3.2 1L Gel Dose Response Studies

The effects of varying the mean dose rate on gel response by increasing the number of radiation beams and employing a sliding window irradiation technique are illustrated in figure 7.3 for gels irradiated using a range of doses between 0 - 20 Gy. Error bars represent the standard deviation of ΔN_{CT} measured at the centre of the 1 L cylinder.

Figure 7.3a shows baseline measures of dose response for the gel irradiated at the top and bottom of the 1 L cylinder with the calibration plan using 3 open fields for each distribution. It is readily seen that while ΔN_{CT} agree within experimental uncertainty between 0 - 16 Gy, the slope of the dose response curve is greater for the irradiation performed at the bottom of the gel compared to the distribution delivered to the top of the cylinder. This unexpected finding is in contrast to the agreement observed between dose response curves for the 1 L cylinder used to investigate global intra-batch reproducibility in section 5.3.3. It is possible that the discrepancy between studies is due to gel rotation during fabrication. This procedure may have changed the distribution of gelatin and unreacted monomer molecules in the gel, leading to differences in response at the top and bottom of the container.

Nevertheless, the same behaviour is observed when the experiment is repeated with the distribution at the bottom of the gel delivered using 9 beams (figure 7.3b) and the sliding window irradiation technique (figure 7.3c). This can also be seen in figure 7.3d where the dose response curves for all studies are plotted together.

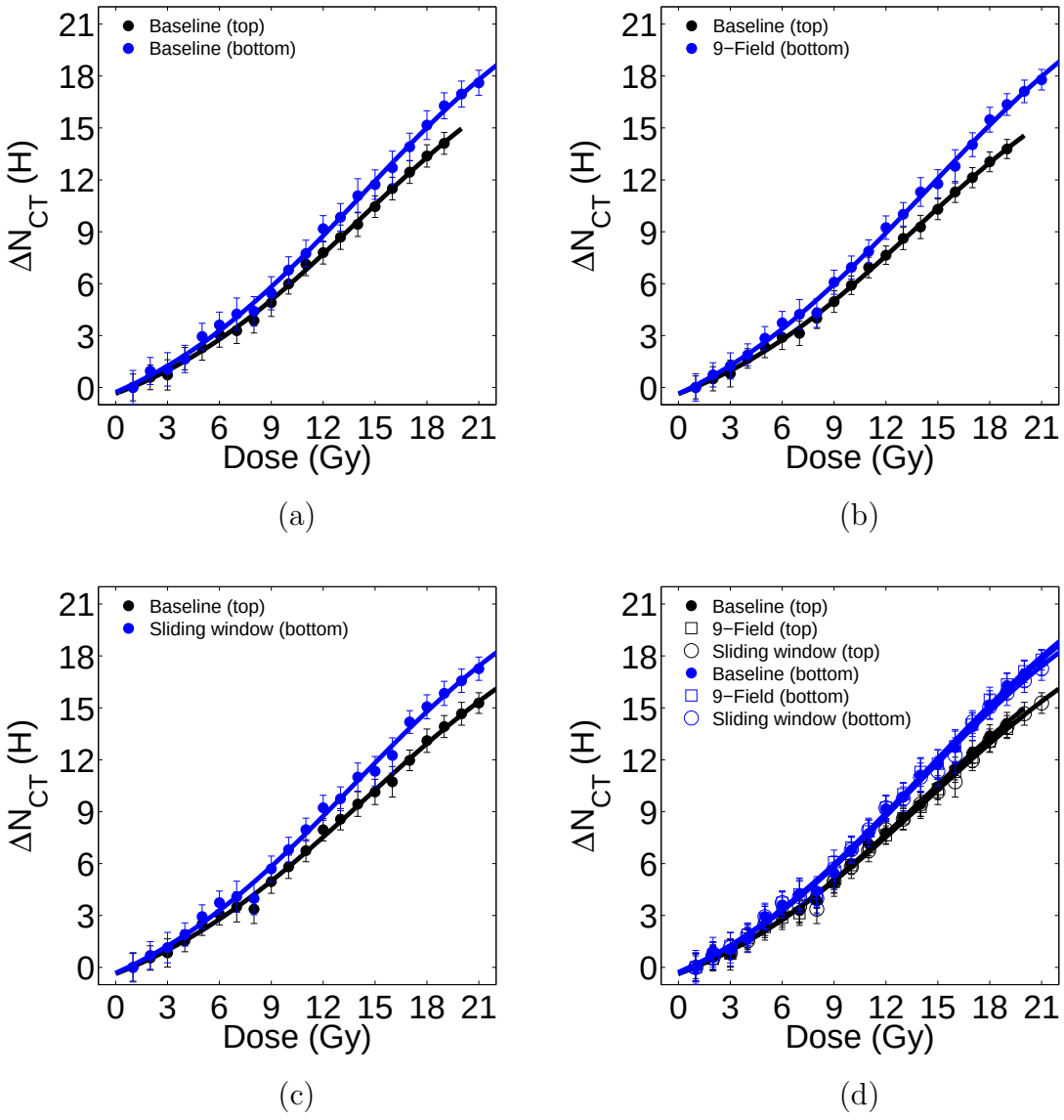

Figure 7.3: Dose response curves for gels irradiated with the 3-field distribution using (a) similar mean dose rates at the top and bottom of the cylinder, (b) different mean dose rates produced by increasing the number of radiation beams at the bottom of the gel and (c) difference mean dose rates produced by using a sliding window irradiation technique for the bottom distribution. The results for the experiments in (a-c) are plotted together in (d).

It is clear from this plot that ΔN_{CT} agree within uncertainty for all experiments when radiation is delivered to the same location in the gel along the length of the 1 L cylinder. This indicates that while the dose response varies between the top and bottom of the cylinder for doses greater than 16 Gy, changes in mean dose rate on the order of seconds to minutes that are produced by increasing the number of beams or using a sliding window irradiation do not significantly influence gel response. As such, mean dose rate variations associated with IMRT treatments due to multiple radiation fields and beam modulation can be ignored during clinical application using the CT PGD system.

Given the results of figure 7.3, additional experiments were performed to determine if the machine dose rate effect found during gel characterization is in fact due to differences in response between the top and bottom of the gel. For this work, the 3-field distribution was delivered to the bottom of two 1 L gels at 400 MU/min and to the top of each gel at 100 MU/min and 600 MU/min, respectively. Figure 7.4 shows ΔN_{CT} plotted as a function of dose for each study. It is readily seen that the dose response curves for the gel irradiated at 100 MU/min and 400 MU/min (figure 7.4a) agree within experimental uncertainty for the entire dose range studied. However, the dose response curves generated at the 600 MU/min and 400 MU/min (figure 7.4b) diverge, similar to the behaviour observed for the mean dose rate studies. In addition, the slope of the dose response curve generated at 600 MU/min is greater than that seen for the curve generated at the same location in the first gel using 100 MU/min. This is demonstrated explicitly in figure 7.4c where the dose response curves generated using machine dose rates between 100 - 600 MU/min at the top of each gel are plotted together. As was found in the original machine dose rate experiment, the response of the gel changes as a function of dose rate and the magnitude of the change varies with dose. In this case, for doses less than 13 Gy, the dose response curves agree within experimental uncertainty. However, beyond 13 Gy, the slope of the dose response decreases as dose rate increases, resulting in a lack of agreement between the 100 MU/min and 600 MU/min curves.

Based on the results of figure 7.4, it is clear that the variability in gel response that occurs when radiation is delivered at different machine dose rates is due to changes in the rate of radiation delivery and not caused by discrepancies in gel response between the top and bottom of the container. The cause of the difference in response at either end of the gel is presently unknown, but may be due to a redistribution of gel components resulting from gel rotation during fabrication. It is also possible

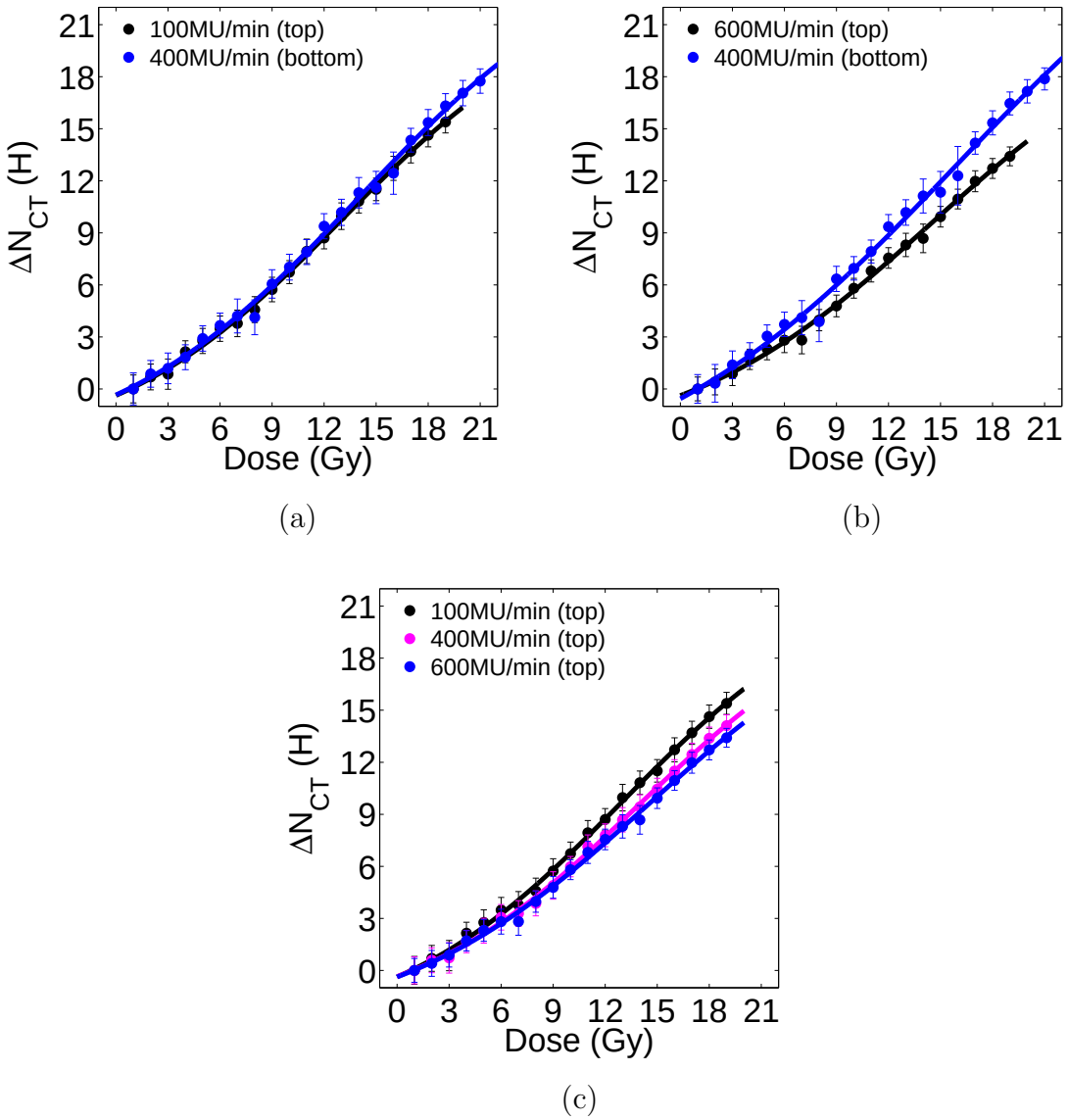

Figure 7.4: Dose response curves for gels irradiated with the 3-field distribution using (a) 100 MU/min at the top of the gel and 400 MU/min at the bottom of the cylinder, (b) 600 MU/min at the top of the cylinder and 400 MU/min at the bottom of the gel and (c) 100 - 600 MU/min at the top of the cylinder.

that this redistribution contributed to reducing the machine dose rate effect observed here compared to the dependence observed in the original study performed during gel characterization.

It is possible that the machine dose rate dependence observed here is due to a larger number of radicals being produced per unit time in a given region of gel at higher dose rates, leading to an increase in the likelihood of two radicals coming together and being rendered neutral through a termination reaction. This would reduce the number of radicals creating polymer in the gel, leading to a decrease in gel density and by extension, decrease in N_{CT} if the gel is irradiated at higher machine dose rates. As indicated above, this effect may be mitigated by increasing the concentration of THPC in the gel system to create a net that prevents radicals from reaching one another. An investigation into the effects of increasing the THPC in the gel to prevent these reactions is presented in section 7.3.4. In addition to increased radical concentration at higher machine dose rates, it was previously suggested in section 5.3.4 that self-crosslinking of NIPAM polymer chains may be responsible for the machine dose rate dependence observed for the new gel formulation investigated in this work. The reader is referred to that section for a detailed description of NIPAM self-crosslinking and section 7.3.4 for an investigation of this effect.

It is also interesting to note that only changes in machine dose rate, which correspond to differences in delivered dose on the order of milliseconds, have been observed to influence gel response. This suggests that certain processes that occur in the gel on the millisecond timescale are influenced by variations in machine dose rate and may be responsible for the observed dependence. One possible process that may be affected by changes in machine dose rate is the swelling of NIPAM polymer molecules. Studies that examine the response of microgels to changes in various environmental conditions have reported the temperature-induced swelling of NIPAM polymer occurs in the time regime from nanoseconds to milliseconds [189, 190]. It is possible that the heat produced by the polymerization reactions in the gel when exposed to radiation cause swelling of NIPAM polymer chains which in turn influences the amount of additional monomer that can be added to the existing polymer. As higher machine dose rates correspond to a larger amount of polymerization and therefore a larger amount of heat in a given region of gel per unit time, higher machine dose rates may cause a greater amount of NIPAM polymer swelling and result in reduced gel response. However, further study is required to determine the exact processes that are affected by millisecond dose rate changes. Nevertheless, it is strongly recommended that each

radiation beam be delivered with the same machine dose rate in order for reliable dose measurements to be obtained with the new CT PGD system for all clinical applications.

7.3.3 Effect of Increasing Antioxidant

In light of the persistent machine dose rate dependence observed for the gel formulation used throughout this work, an attempt was made to reduce the effect by increasing the concentration of THPC in the gel system. Figure 7.5a illustrates the measured dose response for the 10mM gel irradiated at machine dose rates of 100 MU/min and 600 MU/min at the bottom and top of the 1 L cylinder, respectively. Error bars represent the standard deviation of ΔN_{CT} measured at the centre of the 1 L cylinder. Similar to the original machine dose rate study, the dose response for the 10 mM gel changes as a function of dose rate and the magnitude of the change varies as a function of dose. For doses less than 5 Gy, the dose response curves agree within experimental uncertainty. However, between 5 - 20 Gy, the slope of the dose response decreases as dose rate increases, and beyond 20 Gy, differences in slope begin to stabilize as the dose response begins to saturate. This behaviour is identical to that observed in the original dose rate experiment, indicating that increasing the concentration of THPC in the gel system dose not reduce or remove the machine dose rate effect. In fact, the additional antioxidant reduces the overall response of the gel. This is clearly seen in figures 7.5b and c, where a comparison between the dose response curves for the 5 mM and 10 mM gels are shown for irradiations performed at 100 MU/min and 600 MU/min, respectively. At both machine dose rates, the response of the gel decreases by as much as 50% in going from 5 mM THPC concentration to 10 mM of antioxidant.

The results of figure 7.5 clearly indicate that increasing the concentration of THPC in the gel system is not an effective means for mitigating the observed machine dose rate dependence. In addition, increasing the concentration of THPC leads to a significant decrease in gel response which ultimately reduces the dose resolution of the gel dosimetry system. As such, the 5 mM gel is a superior formulation compared to the 10 mM recipe and is more suitable for CT PGD. These findings also suggest that the increase in antioxidant concentration does not produce sufficient additional crosslinking between gelatin and THPC to prevent monomer radicals from reaching each other and terminating at higher dose rates. However, it is possible that increased radical

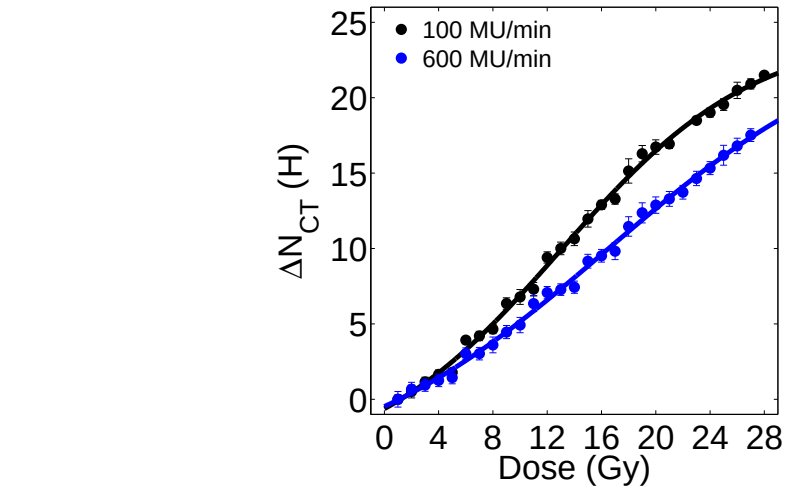

(a)

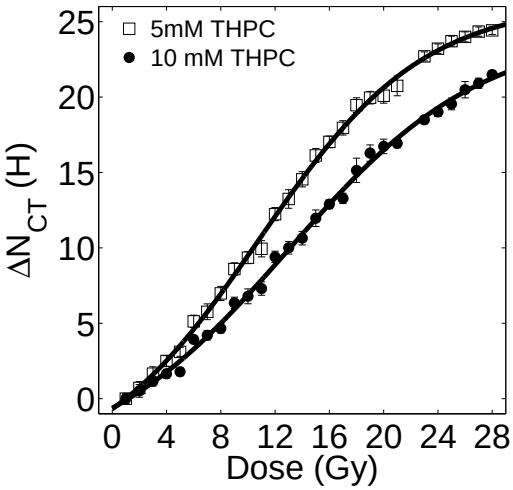

(b)

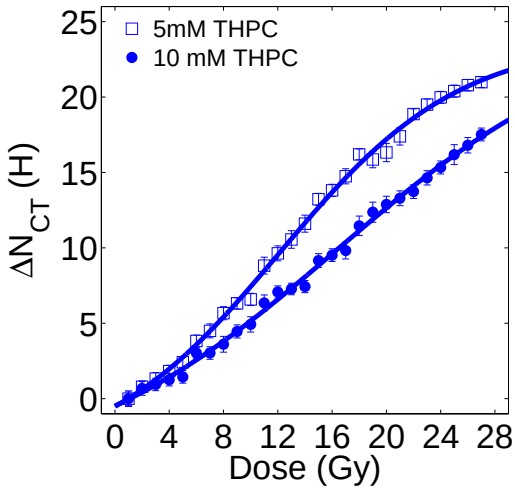

(c)

Figure 7.5: Dose response curves for (a) one gel made with 10 mM THPC that was irradiated at 100 MU/min and 600 MU/min, (b) one gel manufactured using 5 mM THPC and a second gel made with 10 mM antioxidant that were both irradiated at 100 MU/min and (c) gels fabricated using 5 mM and 10 mM THPC that were irradiated at 600 MU/min.

termination resulting from use of a higher dose rate does not explain the observed machine dose rate effect observed here. As indicated in the original mean dose rate experiment in section 5.3.4, it is possible that the effect may be due, at least in part, to self-crosslinking of NIPAM polymer chains. This possibility is explored in detail in the following section using a gel fabricated with no BIS.

7.3.4 Effect of Removing N, N'-Methylenebisacrylamide

Based on the results of the previous sections, an experiment was performed to determine if NIPAM self-crosslinking contributes to the observed machine dose rate effect associated with the new gel formulation. Figure 7.6a illustrates the measured dose response for the polymer gel manufactured with no BIS that was irradiated at machine dose rates of 100 MU/min and 600 MU/min at either end of the 1 L cylinder. Error bars represent the standard deviation of ΔN_{CT} measured at the centre of the gel. It is readily seen that the gel exhibits a significant dose response in spite of the absence of BIS as ΔN_{CT} change by more than 12 HU over the dose range studied for both machine dose rates. This suggests significant NIPAM self-crosslinking may be occurring in the gel system, resulting in the formation of polymer molecules with sufficient density to change the N_{CT} of the gel at the point of irradiation. Nevertheless, removing the BIS from the gel reduces its overall response. This is clearly seen in figures 7.5b and c, where a comparison between the dose response curves for the gel containing NIPAM and BIS and the BIS-free gel are shown for irradiations performed at 100 MU/min and 600 MU/min, respectively. At both machine dose rates, the response of the gel decreases by over 130% when the BIS is removed. This indicates that while NIPAM self-crosslinking may play an important role in the overall response of the gel, the presence of BIS provides significantly larger changes in N_{CT} and superior dose resolution.

It is also seen from figure 7.6a that a significant machine dose rate dependence is present for the BIS-free gel as the dose response changes as a function of dose rate and the magnitude of the change varies as a function of dose. For doses less than 7 Gy, the dose response curves generated at both dose rates agree within experimental uncertainty. However, the slope of the dose response decreases as dose rate increases for all doses beyond 7 Gy. In addition, the changes in slope seen here for the BIS-free gel are more pronounced than those observed for the previous machine dose rate studies. For example, ΔN_{CT} differ by 20.7% at 20 Gy for the gel composed of NIPAM

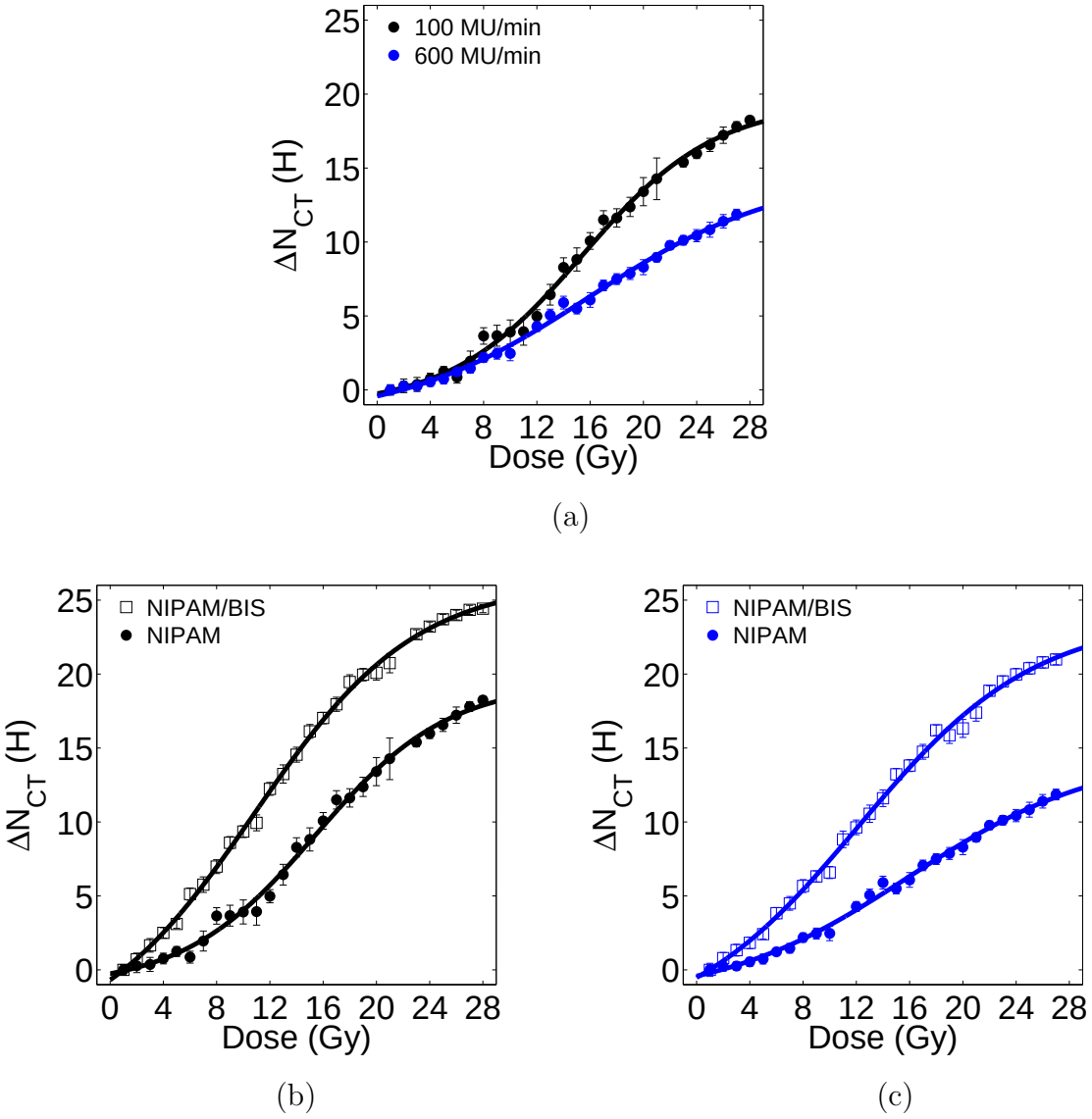

Figure 7.6: Dose response curves for (a) one gel made with no BIS and irradiated at 100 MU/min and 600 MU/min, (b) one gel manufactured using NIPAM and BIS and one made with only NIPAM that were irradiated at 100 MU/min and (c) gels fabricated using NIPAM and BIS and only NIPAM that were irradiated at 600 MU/min.

and BIS (5 mM THPC) but this number more than doubles for the BIS-free gel, with ΔN_{CT} differing by 47.1% at 20 Gy. These findings suggest NIPAM self-crosslinking may be contributing to the observed dose rate effect in the gel composed of NIPAM and BIS and that the presence of BIS may actually reduce the dose rate dependence for the original gel recipe. Further study on these processes is necessary to confirm this hypothesis and may be considered for future work.

7.4 Chapter Summary

This chapter presents work completed to investigate the dose rate properties of the new gel formulation used throughout this work and provides important information about the dose rate dependencies associated with the gel and how they can be mitigated. Initial studies examined the dependence of gel response on changes in mean dose rate on the order of seconds to minutes. An investigation performed using gel vials irradiated to 12 Gy suggested changes in mean dose rate due to variations in the number of radiation beams and the beam-on and beam-off duration do not influence gel response. However, the poor batch reproducibility found for the gel vial system make it difficult to draw concrete conclusions based on these findings. For this reason, additional mean dose rate experiments were performed that examined gel response for a range of doses between 0 - 20 Gy using 1 L cylinders. This work revealed that while the dose response varies between the top and bottom of each gel cylinder for doses greater than 16 Gy, changes in mean dose rate on the order of seconds to minutes produced by increasing the number of beams or using a sliding window irradiation do not significantly influence gel response. These findings indicate mean dose rate variations associated with IMRT treatments due to multiple radiation fields and beam modulation can be ignored during clinical application using the CT PGD system. Based on the results of the mean dose rate studies using 1 L gels, additional experiments were conducted to determine if the machine dose rate dependence observed during gel characterization is in fact due to differences in response between the top and bottom of the gel. This work revealed the machine dose rate dependence remains when irradiations are performed at the same location along the length of the 1 L cylinder but the magnitude of the effect is reduced compared to the original study, possibly because of a redistribution of gel components resulting from rotation of each gel during fabrication. Moreover, the machine dose rate dependence can be ignored for doses below 13 Gy as the dose response for irradiations performed

using 100 - 600 MU/min agree below this threshold. Nevertheless, it is recommended that irradiations be performed using the same machine dose rate to avoid dosimetric errors during clinical application of the system. Further study focused on examining how changing the gel formulation affects the observed machine dose rate dependence. These investigations revealed that increasing the concentration of THPC in the gel system does not mitigate the observed machine dose rate dependence and instead reduces the overall response of the gel. Additional work using gel fabricated without BIS showed significant NIPAM self-crosslinking may be occurring in the gel when exposed to ionizing radiation and that these reactions may be contributing to the machine dose rate effect.

Chapter 8

Conclusions

This dissertation presents work performed to develop an CT PGD system for 3D verification of complex RT dose distributions using a new polymer gel formulation. The new gel is optimized for use with CT readout and provides improved dose resolution over previous formulations. Development of the system was carried out in three stages: characterization of the essential dosimetric properties of the new gel recipe, commissioning of a multislice CT scanner for fast and reliable imaging of 3D gel volumes and investigation of a dose rate dependence found during gel characterization. The results for each study are summarized in section 8.1. Section 8.2 presents possible future directions for continued development of the system.

8.1 Summary of Results

The first stage of this work characterized the essential dosimetric properties of the new polymer gel formulation. Temporal stability was examined using gel vials irradiated to 10 Gy and imaged one at a time between 3 - 45 hours after irradiation. The resulting evolution of ΔN_{CT} showed the polymerization reactions stabilize 15 hours post-irradiation. Similarly, spatial stability was investigated in a 1 L gel irradiated to 10 Gy over half its volume and imaged at four locations along the length of the cylinder between 15 - 47 hours post-irradiation. Profiles through the diameter of the distribution at different time points revealed the response of the gel is stable up to 36 hours after irradiation. Based on the results of these experiments, it is recommended that all imaging of the new formulation be performed within 15 - 36 hours after irradiation to ensure a consistent gel response. Further experiments were per-

formed to investigate the intra- and inter-batch reproducibility of the gel for doses between 0 - 28 Gy. Intra-batch reproducibility was examined within a single region of gel and throughout a gel volume while inter-batch reproducibility was evaluated using three gels each fabricated on a different day. By all experiments, batch reproducibility for the new formulation was found to be excellent over the entire dose range studied. These findings indicate that not only can calibration and test irradiations be delivered to the same gel volume but also that consistent results will be obtained for different gel batches. An additional experiment was then performed to determine if variations in dose rate influence gel response. A simple treatment plan was used to deliver a range of doses up to 28 Gy to the top and bottom of a 1 L gel at 100 MU/min and 600 MU/min, respectively. Significant variations in response were observed between the two irradiations, indicating a machine dose rate dependence for the new gel formulation. Variations in gel response due to other types of dose rate were investigated in the last chapter of this work and are summarized below. Finally, an example clinical application of the new gel formulation was performed using an IMRT treatment validation. Comparison of gel measured and planned doses yielded excellent results, with a 2D gamma analysis showing 99.3% agreement at the isocentre slice of the distribution. Overall, the results of these studies provided valuable information about the processes required to perform accurate and reliable dose measurements and demonstrate the new gel formulation shows great promise for use in an CT PGD system for complex RT dosimetry.

The second part of this work focused on commissioning a multislice CT scanner for CT PGD. A new slice-by-slice background subtraction technique was introduced that involves subtracting the background image at a given slice from the test image at the corresponding position in the detector array. This method was found to effectively remove variations in N_{CT} due to the anode heel effect and is the recommended method for performing background subtraction when using a multislice scanner. Additional investigations showed the relationships between image noise and the x-ray tube voltage and current, gantry rotation time and slice thickness are consistent between the single and multislice scanners used in this work, with the exception of tube voltage, which has less of an impact on noise for the multislice system. In addition, direct comparison of the image quality associated with the two machines confirmed consistent noise and uniformity characteristics between single and multslice systems. Together, these findings show the scanners can be used interchangeably and the recommendations for optimizing image quality in CT PGD using a single slice machine

also apply to multislice scanners. Further study showed N_{CT} and noise are consistent across image slices acquired simultaneously using the multislice detector array for all slice thicknesses and also over the different detector configurations for slice thicknesses between 1.25 - 10 mm. These results show multiple images can be reliably collected at the same time using any slice thickness and that the detector configurations can be used interchangeably for images collected with slice thickness greater than 1.25 mm. Additional experiments were then conducted to investigate the effects of x-ray tube load. Based on this work, it is recommended that volume imaging be performed using axial mode of acquisition and slice-by-slice background subtraction with a separate set of background images. This reduces the scanning time by up to 4 times when compared to imaging a volume using the single slice machine. As such, multislice scanning is the recommended technique for dose readout in CT PGD. Finally, images through an active blank gel that was not irradiated indicate deviations in N_{CT} occur at the bottom of the 1 L cylinder that may be due to settling of gelatin molecules and N_{CT} can vary across the diameter of the cylinder by up to 7 H. While the variations across the diameter of the cylinder are relatively consistent over the length of the gel, possible mitigation strategies to account for gel settling include agitating the gel immediately before or during setting.

The final stage of this work examines the dose rate dependence of the new gel formulation found during gel characterization. Initial investigations focused on examining the dependence of gel response on changes in mean dose rate using gel vials irradiated to 12 Gy. Three studies were performed where the mean dose rate was varied across the vials of each experiment by changing the number of radiation beams and/or the beam on and beam off time of each field. The results of these studies suggest that variations in mean dose rate do not influence gel response, however, poor batch reproducibility was observed for the vial system, making it difficult to draw concrete conclusions based on these findings. For this reason, additional experiments were performed that examined changes in gel response with variations in mean dose rate using 1 L cylinders. Three experiments were performed where, similar to the original machine dose rate study, the mean dose rate was varied between dose distributions delivered at the top and bottom of the 1 L cylinder. Each distribution provided a range of doses between 0 - 20 Gy. For the first experiment, the mean dose rate was kept as close as possible between the two distributions to acquire a baseline comparison of gel response at either end of the cylinder. For the second and third experiments, the mean dose rate was varied from the baseline experiment for the dis-

tribution at the bottom of the gel by increasing the number of radiation beams and using a sliding window irradiation technique, respectively. These studies showed that while the dose response varies between the top and bottom of each 1 L gel for doses greater than 16 Gy, changes in mean dose rate on the order of seconds to minutes do not significantly influence gel response. Additional experiments were then conducted to determine if the machine dose rate effect is in fact due to differences in response between the top and bottom of the gel and it was revealed that the machine dose rate effect remains when irradiations are performed at the same location along the length of the 1 L cylinder. This study proves that variations in machine dose rate on the order of milliseconds have a significant impact on the amount of polymer that forms in the gel system for a given absorbed dose and by extension the resulting, measured ΔN_{CT}. This may be due to self-crosslinking of NIPAM polymer chains or swelling of NIPAM polymer. In light of these findings, further studies were performed to examine how changing the gel formulation affects the observed machine dose rate dependence. The machine dose rate study was repeated using a gel manufactured with increased THPC concentration to determine if the additional antioxidant in the gel system mitigated the observed effect. However, increasing the concentration of THPC was found to reduce the overall response of the gel. As such, a final experiment was performed where the machine dose rate study was repeated with a gel made with no BIS to determine if NIPAM self-crosslinking may be contributing to the machine dose rate effect. The results of this study show that while the response of the gel is reduced compared to the original recipe, a significant range of ΔN_{CT} values are produced upon exposure to ionizing radiation that may be due to NIPAM self-crosslinking. In addition, the machine dose rate effect for the BIS-free gel is more pronounced than that found for the original gel recipe. As such, these findings strongly suggest NIPAM self-crosslinking may be one cause of the dose rate effect observed for the new gel formulation used throughout this work. Further study is needed to confirm this hypothesis.

In summary, this dissertation has significantly advanced the field of gel dosimetry by providing a prototype CT PGD system with enhanced dose resolution for complex RT treatment verification. Valuable knowledge has been gained on the dose response characteristics of highly radiation sensitive polymer gels fabricated with NIPAM which are imperative for correct operation of the new dosimetry system. In particular, a machine dose rate dependence was found that can easily be accounted for by using the same machine dose rate for all gel irradiations. In additon, the in-

troduction of multislice CT scanning into CT PGD allows images to be collected for an entire dose distribution in a matter of minutes. Finally, an example IMRT treatment verification provides evidence of the remarkable ability of this new system to record the type of spatial variation seen in complex dose distributions and accurately represent steep dose gradients common in modern RT treatments. Together these developments, combined with the low cost and easy accessibility of CT scanners, provide compelling evidence that the CT PGD system introduced here shows great promise as a clinical tool for evaluating complex dose distributions in modern RT. However, further develop of the system is required before being implemented routinely in RT clinics and possible future directions are provided below.

8.2 Future Work

There are a number of avenues for further development of the CT PGD system introduced in this dissertation. As a starting point, a thorough examination of what is causing the variations in N_{CT} observed across the diameter of the unirradiated active gel investigated in section 6.3.5 would provide valuable information for advancement of the system. The magnitude of the variation is relatively constant over the length of the cylinder (with the exception of the bottom 2 cm of the gel), and as such, this variability has been largely ignored in this work. However, by rigorously characterizing the changes in N_{CT} throughout an active unirradiated gel, a 3D map of N_{CT} could be constructed and used to correct this variability. It is possible that this would provide more accurate and consistent dose measurements during clinical application. Similarly, an investigation into the source of the discrepancies observed between dose response curves measured at the top and bottom of the 1 L gels in section 7.3.2 would cast light on a potentially limiting feature of the dosimetry system. As a starting point, an active 1 L gel could be irradiated to a uniform dose over its entire volume and imaged over the full length of the cylinder using the multislice scanner. This could be done for gels that are rotated and those that remain unagitated before being placed in the refrigerator. Not only would this provide a 3D map showing gel response that could be used to correct variations in measured dose over the length of the cylinder, it may also give an indication of the distribution of monomers within the gel volume and provide insight into a compensation strategy for attaining a homogenous monomer distribution. Experiments could also be performed using Raman spectroscopy to determine the exact cause of the machine dose

rate dependence observed for the new gel and determine if NIPAM self-crosslinking is indeed a factor contributing to the effect. The inherent ability of the system to provide measures of dose in 3D with high spatial resolution suggest the next step for the system after these initial investigations is to commission it for evaluation of stereotactic procedures. This would require a more rigorous, image-based localization system that could be designed and tested for a number of specific treatment sites (e.g. brain, spinal cord). This exciting avenue for future work would provide a valuable tool in modern RT for highly complex treatments.

Appendix A

Ion Chamber Measurements

Ionization chamber measurements were performed for the vial mean dose rate studies conducted in chapter 7. These measurements were used to adjust the SSD of the acrylic phantom so the deposited dose rate at the centre of each vial was equal to 1 cGy/MU. This allowed computation of the mean dose rate for each vial over the treatment session. All charge measurements were acquired using a farmer chamber and Unidos E electrometer (PTW, Freiburg Germany) on a Truebeam LINAC. For each charge measurement, a total of 100 MU were delivered to the chamber using 6 MV photons and one anterior, 10 x 10 cm^2 field at 400 MU/min. A chamber warmup procedure was performed where a series of successive 100 MU beams were delivered until the response of the chamber stabilized.

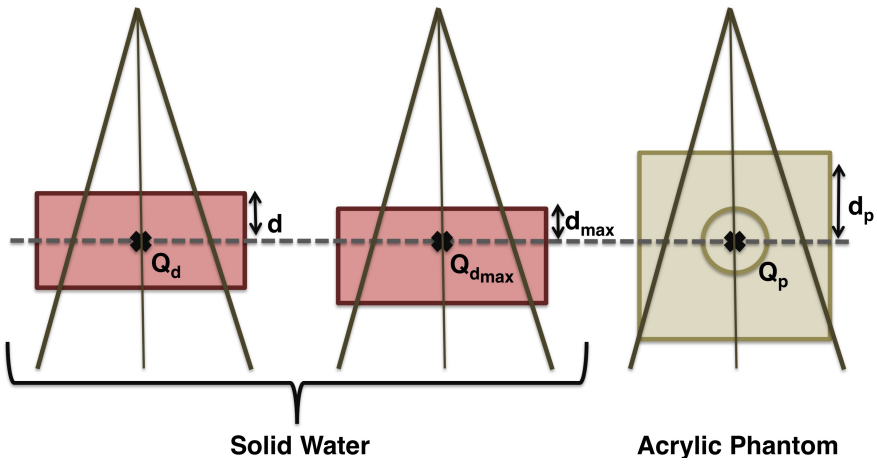

Figure A.1: The process used to determine the SSD where 1 cGy/MU is delivered to each gel vial using the acrylic phantom.

Figure A.1 illustrates the process used to determine the SSD for the acrylic phantom that gave 1 cGy/MU at the centre of the vial. To begin, charge measurements were made using the LINAC calibration set-up. The chamber was placed at a depth, d, of 10 cm in solid water resulting in an SSD of 90 cm. An additional 10 cm of solid water were placed below the chamber to account for backscattered radiation. Three charge measurements, Q_d, were then acquired and averaged. As the LINAC is calibrated to deliver 1 cGy/MU at the depth of maximum dose, d_m, the tissue maximum ratio (TMR) from LINAC commissioning was then used to compute the charge where the maximum dose occurs, $Q_{d_{max}}$, using equation A.1:

$$TMR = \frac{Q_d}{Q_{d_{max}}}. \tag{A.1}$$

For 6 MV photon beams, $d_m = 1.5$ cm. At this stage, the chamber was removed from the solid water and placed in a custom-built acrylic sleeve that fits snuggly into one of the acrylic pots used to irradiate the gel vials. The chamber and pot were then placed in the acrylic phantom which was subsequently positioned on the LINAC couch. Three charge measurements, Q_p, were acquired and averaged to obtained a baseline reading of the charge for the phantom at isocentre. The position of the phantom was then adjusted and additional charge measurements were acquired until $Q_p = Q_{d_{max}}$, which occurred at an SSD = 75.6 cm. At this SSD, the dose is delivered to the vial at 1 cGy/MU.

Bibliography

[1] Canadian Cancer Society's Steering Committee on Cancer Statistics. Canadian Cancer Statistics 2012. *Canadian Cancer Society*, 2012.

[2] J.S. Tobias. The role of radiotherapy in the management of cancer – an overview. *Ann. Acad. Med. Singapore*, 25(3):371–379, 1996.

[3] G. Delaney, S. Jacob, C. Featherstone, and M. Barton. The role of radiotherapy in cancer treatment. *Cancer*, 104:1129–1137, 2005.

[4] M. Joiner and A. van der Kogel. *Basic Clinical Radiobiology.* Hodder Arnold, London, 4^{th} edition, 2009.

[5] National Cancer Institute. Radiation Therapy and You. *National Institute of Health*, 2012.

[6] W. Bogdanich. Case studies: When medical radiation goes awry. *The New York Times*, 2010.

[7] E. J. Hall. *Radiobiology for the Radiologist.* LippinCott Williams & Wilkins, Philadelphia, 2012.

[8] J. Van Dyk. *The Modern Technology of Radiation Oncology*, volume 2. Medical Physics Publishing, Madison, 2005.

[9] F. M. Khan. *The Physics of Radiation Therapy.* Lippincott Williams and Wilkins, Baltimore, 4th edition, 2010.

[10] J. Van Dyk. *The Modern Technology of Radiation Oncology*, volume 1. Medical Physics Publishing, Madison, 1999.

[11] M. Guckenberger, A. Richter, T. Krieger, J. Wilbert, K. Baier, and M. Flentje. Is a single arc sufficient in volumetric-modulated arc therapy (VMAT) for complex-shaped target volumes? *Radiother. Oncol.*, 93:259–265, 2009.

[12] E. Wong, J. Z. Chen, and J. Greenland. Intensity-modulated arc therapy simplified. *Int. J. Radiat. Oncol. Biol. Phys.*, 53:222–235, 2002.

[13] K. Otto. Volumetric modulated arc therapy: IMRT in a single gantry arc. *Med. Phys.*, 35:310–317, 2008.

[14] N. Y. Lee and S. A. Terezakis. Intensity-modulated radiation therapy. *J. Surg. Oncol.*, 97:691–696, 2008.

[15] E. Huang, L. Dong, A. Chandra, D. A. Kuban, I. I. Rosen, A. Evans, and A. Pollack. Intrafraction prostate motion during IMRT for prostate cancer. *Int. J. Radiat. Oncol. Biol. Phys.*, 53:261–268, 2002.

[16] S. Poling. Critical error: The Lisa Norris story. *British Broadcasting Corporation News*, June 2007.

[17] E. Yorke, D. Gelblum, and E. Ford. Patient Safety in External Beam Radiation Therapy. *Am. J. Roentgenol.*, 196:768–772, 2011.

[18] ICRP. Preventing accidental exposures from new external beam radiation therapy technologies. *ICRP Publication 112. Ann.*, 39, 2009.

[19] J. Shafiq, M. Barton, D. Noble, C. Lemer, and L. J. Donaldson. An international review of patient safety measures in radiotherapy practice. *Radiother. Oncol.*, 92:15–21, 2009.

[20] The Royal College of Radiologists, Society and College of Radiographers, Institute of Physic and Engineering in Medicine, National Patient Safety Agency, and British Institute of Radiology. Towards Safer Radiotherapy. *The Royal College of Radiologists*, 2008.

[21] World Health Organization. Radiotherapy risk profile: technical manual. *World Health Organization*, 2008.

[22] G. Huang, G. Medlam, J. Lee, S. Billingsley, J. Bissonnette, J. Ringash, G. Kane, and D. Hodgson. Error in the delivery of radiation therapy: Results

of a quality assurance review. *Int. J. Radiat. Oncol. Biol. Phys.*, 61:1590–1595, 2005.

[23] H. Johnston, M. Hilts, W. Beckham, and E. Berthelet. 3D ultrasound for prostate localization in radiation therapy: a comparison with implanted fiducial markers. *Med. Phys.*, 35:2403–2413, 2008.

[24] L. A. DeWerd, G. S. Ibbott, A. S. Meigooni, M. G. Mitch, M. J. Rivard, K. E. Stump, B. R. Thomadsen, and J. L. M. Venselaar. A dosimetric uncertainty analysis for photon-emitting brachytherapy sources: Report of AAPM Task Group No. 138 and GEC-ESTRO. *Med. Phys.*, 38:782, 2011.

[25] F. H. Attix. *Introduction to Radiological Physics and Radiation Dosimetry.* Wiley-VCH, Weinheim, 2004.

[26] H. E. Johns and J. R. Cunningham. *The Physics of Radiology.* Charles C. Thomas, Springfield, 4^{th} edition, 1983.

[27] D. A. Low, J. M. Moran, J. F. Dempsey, L. Dong, and M. Oldham. Dosimetry tools and techniques for IMRT. *Med. Phys.*, 38:1313–1338, 2011.

[28] P. H. Halvorsen. Dosimetric evaluation of a new design MOSFET in vivo dosimeter. *Med. Phys.*, 32:110–117, 2005.

[29] A. B. Rosenfeld. MOSFET dosimetry on modern radiation oncology modalities. *Radiat. Prot. Dosim.*, 101:393–398, 2002.

[30] R. L. Stern, R. Heaton, M. W. Fraser, S. Murty Goddu, T. H. Kirby, K. L. Lam, A. Molineu, and T. C. Zhu. Verification of monitor unit calculations for non-IMRT clinical radiotherapy: Report of AAPM Task Group 114. *Med. Phys.*, 38:504, 2011.

[31] A. Niroomand-Rad, C. R. Blackwell, B. M. Coursey, K. P. Gall, J. M. Galvin, W. L. McLaughlin, A. S. Meigooni, R. Nath, J. E. Rodgers, and C. G. Soares. Radiochromic film dosimetry. *Med. Phys.*, 25:2093–2115, 1998.

[32] Petoukhova, A. L. and van Egmond, J. and Eenink, M. G. C. and Wiggenraad, R. G. .J and van Santvoort, J. P. C. The ArcCHECK diode array for dosimetric verification of HybridArc. *Phys. Med. Biol.*, 56:5411–5428, 2011.

[33] W. van Elmpt, L. McDermott, S. Nijsten, M. Wendling, P. Lambin, and B. Mijnheer. A literature review of electronic portal imaging for radiotherapy dosimetry. *Radiother. Oncol.*, 88:289–309, 2008.

[34] K. J. Roxby and J. C. Crosbie. Pre-treatment verification of intensity modulated radiation therapy plans using a commercial electronic portal dosimetry system. *Australas Phys. Eng. Sci. Med.*, 33:51–57, 2010.

[35] van Elmpt, W. and Petit, S. and De Ruysscher, D. and Lambin, P. and Dekker, A. 3D dose delivery verification using repeated cone-beam imaging and EPID dosimetry for stereotactic body radiotherapy of non-small cell lung cancer. *Radiother. Oncol.*, 94:188–194, 2010.

[36] W. Ansbacher. Three-dimensional portal image-based dose reconstruction in a virtual phantom for rapid evaluation of IMRT plans. *Med. Phys.*, 33:3369–3382, 2006.

[37] J. Adamovics and M. J. Maryanski. Characterisation of PRESAGE: A new 3-D radiochromic solid polymer dosemeter for ionising radiation. *Radiat. Prot. Dosim.*, 120:107–112, 2006.

[38] S. Brown, A. Venning, Y. De Deene, P. Vial, L. Oliver, J. Adamovics, and C. Baldock. Radiological properties of the PRESAGE and PAGAT polymer dosimeters. *Appl. Radiat. Isot.*, 66:1970–1974, 2008.

[39] C.-S. Wuu and Y. Xu. 3-D dosimetry with optical CT scanning of polymer gels and radiochromic plastic dosimeter (in press). *Radiat. Meas.*, pages 1–5, 2011.

[40] H. S. Sakhalkar, J. Adamovics, G. Ibbott, and M. Oldham. A comprehensive evaluation of the PRESAGE/optical-CT 3D dosimetry system. *Med. Phys.*, 36:71–82, 2009.

[41] C. Clift, A. Thomas, J. Adamovics, Z. Chang, I. Das, and M. Oldham. Toward acquiring comprehensive radiosurgery field commissioning data using the PRESAGE®/ optical-CT 3D dosimetry system. *Phys. Med. Biol.*, 55(5):1279–1293, 2010.

[42] H. Sakhalkar, D. Sterling, J. Adamovics, G. Ibbott, and M. Oldham. Investigation of the feasibility of relative 3D dosimetry in the Radiologic Physics

Center Head and Neck IMRT phantom using Presage/optical-CT. *Med. Phys.*, 36(7):3371–3377, 2009.

[43] C. Baldock, Y. De Deene, S. Doran, G. Ibbott, A. Jirasek, M. Lepage, K. B. McAuley, M. Oldham, and L. J. Schreiner. Polymer gel dosimetry. *Phys. Med. Biol.*, 55:R1–63, 2010.

[44] J. N. M. Chain, A. Jirasek, L. J. Schreiner, and K. B. McAuley. Cosolvent-free polymer gel dosimeters with improved dose sensitivity and resolution for x-ray CT dose response. *Phys. Med. Biol.*, 56:2091–2102, 2011.

[45] J. T. Bushberg and J. A. Seibert and E. M. Leidholdt, Jr. and J. M. Boone. *The Essential Physics of Medical Imaging.* Lippincott Williams and Wilkins, Philadelphia, 3^{rd} edition, 2012.

[46] J. Hsieh. *Computed Tomography Principles, Design, Artifacts, and Recent Advances.* Society of Photo-Optical Instrumentation and Engineers, Bellingham, 2^{nd} edition, 2009.

[47] L. W. Goldman. Principles of CT and CT Technology. *J. N. M. T.*, 35:115–128, 2007.

[48] W. A. Kalender. X-ray computed tomography. *Phys. Med. Biol.*, 51:R29–R43, 2006.

[49] C. R. Crawford and K. F. King. Computed tomography scanning with simultaneous patient translation. *Med. Phys.*, 17(6):967–982, 1990.

[50] K. Klingenbeck-Regn and S. Schaller and T. Flohr and B. Ohnesorge and A. F. Kopp and U. Baum. Subsecond multi-slice computed tomography: basics and applications. *Eur. J. Radiol.*, 31:110–124, 1999.

[51] S.S. Vedam, P.J. Keall, V. R. Kini, H. P. Shukia, and R. Mohan. Acquiring a four-dimensional computed tomography dataset using an external repiratory signal. *Phys. Med. Biol.*, 48:45–62, 2003.

[52] Pan, T. and Lee, T.-Y. and Rietzel, E. and Chen, G. T. Y. 4D-CT imaging of a volume influenced by respiratory motion on multi-slice CT. *Med. Phys.*, 31:333–340, 2004.

[53] K. K. L. Fung and W. B. Gilboy. "Anode heel effect" on patient dose in lumbar spine radiography. *BRIT. J. RADIOL.*, 73:531–536, 2000.

[54] T Pan. Comparison of helical and cine acquisitions for 4D-CT imaging with multislice CT. *Med. Phys.*, 32:627–634, 2005.

[55] E. Rietzel, T. Pan, and G. T. Y. Chen. Four-dimensional computed tomography: Image formation and clinical protocol. *Med. Phys.*, 32:874–889, 2005.

[56] D. M. Yildirim and D. H. Brinkmann. An investigation of temporal resolution parameters in cine-mode four-dimensional computed tomography acquisition. *J. Appl. Clin. Med. Phys.*, 9:172–180, 2008.

[57] L. W. Goldman. Principles of CT: Radiation Dose and Image Quality. *J. N. M. T.*, 35:213–225, 2007.

[58] G. Dougherty. *Digital Image Processing for Medical Applications*. Cambridge University Press, Cambridge, 2009.

[59] M. J. Day and G. Stein. Chemical effects of ionizing radiation in some gels. *Nature*, 166:146–147, 1950.

[60] H. L. Andrews, R. E. Murphy, and E. J. LeBrun. Gel dosimeter for depth dose measurements. *Rev. Sci. Instrum.*, 28:329–332, 1957.

[61] P. Alexander, A. Charlesby, and M. Ross. The degradation of solid polymethylmethacrylate by ionizing radiations. *Proc. R. Soc. Lond. A*, 223:3392–404, 1954.

[62] F. E. Hoecker and I. W. Watkins. Radiation polymerization dosimetry. *Int. J. Appl. Radiat. Isot.*, 3:31–35, 1958.

[63] A. L. Boni. A polyacrylamide gamma dosimeter. *Radiat. Res.*, 14:374–380, 1961.

[64] H. Fricke and S. Morse. The chemical action of Roentgen rays on dilute ferrous sulphate solutions as a measure of radiation dose. *Am. J. Roentgenol. Radium Ther. Nucl. Med.*, 18:430–432, 1927.

[65] J. C. Gore, Y. S. Kang, and R. J. Schulz. Measurement of radiation dose distributions by nuclear magnetic resonance (NMR) imaging. *Phys. Med. Biol.*, 29:1189–1197, 1984.

[66] A. Appleby, E. A. Christman, and A. Leghrouz. Imaging of spatial radiation dose distribution in agarose gels using magnetic resonance. *Med. Phys.*, 14:382–384, 1986.

[67] L. E. Olsson, B. A. Westrin, A. Fransson, and B. Nordell. Diffusion of ferric ions in agarose dosimeter gels. *Phys. Med. Biol.*, 37:2243–2252, 1992.

[68] C. Baldock, P. J. Harris, A. R. Piercy, and B. Healy. Experimental determination of the diffusion coefficient in two-dimensions in ferrous sulphate gels using the finite element method. *Australas. Phys. Eng. Sci. Med.*, 24:19–30, 2001.

[69] M. J. Maryanski, J. C. Gore, R. P. Kennan, and R. J. Schulz. NMR relaxation enhancement in gels polymerized and cross-linked by ionizing radiation: a new approach to 3D dosimetry by MRI. *Magn. Reson. Imaging*, 11:253–258, 1993.

[70] M. J. Maryanski, R. J. Schulz, G. S. Ibbott, J. C. Gatenby, J. Xie, D. Horton, and J. C. Gore. Magnetic resonance imaging of radiation dose distributions using a polymer-gel dosimeter. *Phys. Med. Biol.*, 39:1437–1455, 1994.

[71] De Deene, Y. and Hanselaer, P. and De Wagter, C. and Achten, E. and De Neve, W. An investigation of the chemical stability of a monomer/polymer gel dosimeter. *Phys. Med. Biol.*, 45:859–878, 2000.

[72] A. Jirasek and C. Duzenli. Effects of crosslinker fraction in polymer gel dosimeters using FT Raman spectroscopy. *Phys. Med. Biol.*, 46:1949–1961, 2001.

[73] A. I. Jirasek, C. Duzenli, C. Audet, and J. Eldridge. Characterization of monomer/crosslinker consumption and polymer formation observed in FT-Raman spectra of irradiated polyacrylamide gels. *Phys. Med. Biol.*, 46:151–165, 2001.

[74] De Deene, Y. and Venning, A. and Hurley, C. and Healy, B. J. and Baldock, C. Dose-response stability and integrity of the dose distribution of various polymer gel dosimeters. *Phys. Med. Biol.*, 47:2459–2470, 2002.

[75] De Deene, Y. and Hurley, C. and Venning, A. and Vergote, K. and Mather, M. and Healy, B. J. and Baldock, C. A basic study of some normoxic polymer gel dosimeters. *Phys. Med. Biol.*, 47:3441, 2002.

[76] G. J. Salomons, Y. S. Park, K. B. McAuley, and L. J. Schreiner. Temperature increases associated with polymerization of irradiated PAG dosimeters. *Phys. Med. Biol.*, 47:1435, 2002.

[77] E. Pappas, T. G. Maris, A. Angelopoulos, M. Paparigopoulou, L. Sakelliou, P. Sandilos, S. Voyiatzi, and L. Vlachos. A new polymer gel for magnetic resonance imaging (MRI) radiation dosimetry. *Phys. Med. Biol.*, 44:2677–2684, 1999.

[78] M. Lepage, P. M. Jayasakera, S. A. Back, and C. Baldock. Dose resolution optimization of polymer gel dosimeters using different monomers. *Phys. Med. Biol.*, 46:2665–2680, 2001.

[79] J. C. Gore, M. Ranade, M. J. Maryanski, and R. J. Schulz. Radiation dose distributions in three dimensions from tomographic optical density scanning of polymer gels: I. Development of an optical scanner. *Phys. Med. Biol.*, 41:2695–2704, 1996.

[80] M. J. Maryanski, Y. Z. Zastavker, and J. C. Gore. Radiation dose distributions in three dimensions from tomographic optical density scanning of polymer gels: II. Optical properties of the BANG polymer gel. *Phys. Med. Biol.*, 41:2705–2717, 1996.

[81] M. Oldham, J. H. Siewerdsen, A. Shetty, and D. A. Jaffray. High resolution gel-dosimetry by optical-CT and MR scanning. *Med. Phys.*, 28:1436–1445, 2001.

[82] M. Oldham, J. H. Siewerdsen, S. Kumar, J. Wong, and D. A. Jaffray. Optical-CT gel-dosimetry I: basic investigations. *Med. Phys.*, 30:623–634, 2003.

[83] M. Oldham and L. Kim. Optical-CT gel-dosimetry. II: Optical artifacts and geometrical distortion. *Med. Phys.*, 31:1093–1104, 2004.

[84] M. Hilts, C. Audet, C. Duzenli, and A. Jirasek. Polymer gel dosimetry using x-ray computed tomography: a feasibility study. *Phys. Med. Biol.*, 45:2559–2571, 2000.

[85] M. L. Mather, A. K. Whittaker, and C. Baldock. Ultrasound evaluation of polymer gel dosimeters. *Phys. Med. Biol.*, 47:1449–1458, 2002.

[86] L. Rintoul, M. Lepage, and C. Baldock. Radiation dose distribution in polymer gels by Raman spectroscopy. *Appl. Spectrosc.*, 57:51–57, 2003.

[87] P. M. Fong, D. C. Keil, M. D. Does, and J. C. Gore. Polymer gels for magnetic resonance imaging of radiation dose distributions at normal room atmosphere. *Phys. Med. Biol.*, 46:3105–3113, 2001.

[88] De Deene, Y. and Pittomvils, G. and Visalatchi, S. The influence of cooling rate on the accuracy of normoxic polymer gel dosimeters. *Phys. Med. Biol.*, 52:2719–2728, 2007.

[89] Dumas, E.-M. and Leclerc, G. and Lepage, M. Effect of container size on the accuracy of polymer gel dosimetry. *J. Phys. Conf. Ser.*, 56:239–241, 2007.

[90] Sedaghat, M. and Hubert-Tremblay, V. and Tremblay, L. and Bujold, R. and Lepage, M. Volume-dependent internal temperature increase within polymer gel dosimeters during irradiation. *J. Phys. Conf. Ser.*, 164:012009, 2009.

[91] M. Sedaghat, R. Bujold, and M. Lepage. Effect of the exothermal polymerization reaction on polymer gel dosimetric measurements. *J. Phys. Conf. Ser.*, 250:012018, 2010.

[92] M. Sedaghat, R. Bujold, and M. Lepage. Investigating potential physicochemical errors in polymer gel dosimeters. *Phys. Med. Biol.*, 56:6083–6107, 2011.

[93] M. Sedaghat, R. Bujold, and M. Lepage. Severe dose inaccuracies caused by an oxygen-antioxidant imbalance in normoxic polymer gel dosimeters. *Phys. Med. Biol.*, 56:601–625, 2011.

[94] Vandecasteele, J. and De Deene, Y. On the validity of 3D polymer gel dosimetry: II. Physico-chemical effects. *Phys. Med. Biol.*, 58:43–61, 2012.

[95] R. J. Senden, P. De Jean, K. B. McAuley, and L. J. Schreiner. Polymer gel dosimeters with reduced toxicity: a preliminary investigation of the NMR and optical dose-response using different monomers. *Phys. Med. Biol.*, 51:3301–3314, 2006.

[96] K. Jordan and N. Avvakumov. Radiochromic leuco dye micelle hydrogels: I. Initial investigation. *Phys. Med. Biol.*, 54:6773–6789, 2009.

[97] S. Babic, J. Battista, and K. Jordan. Radiochromic leuco dye micelle hydrogels: II. Low diffusion rate leuco crystal violet gel. *Phys. Med. Biol.*, 54:6791–6808, 2009.

[98] K. Jordan. Optical CT scanning of cross-linked radiochromic gel without cylinder wall. *J. Phys. Conf. Ser.*, 164:012029, 2009.

[99] Vandecasteele, J. and Ghysel, S. and Baete, S. H. and De Deene, Y. Radiophysical properties of micelle leucodye 3D integrating gel dosimeters. *Phys. Med. Biol.*, 56:627–651, 2011.

[100] G. Odian. *Principles of Polymerization.* John Wiley and Sons, Inc., New Jersey, 4^{th} edition, 2004.

[101] A. Jirasek, K. B. McAuley, and M. Lepage. How does the chemistry of polymer gel dosimeters affect their performance? *J. Phys. Conf. Ser.*, 164:012003, 2009.

[102] M. Hilts, A. Jirasek, and C. Duzenli. Effects of gel composition on the radiation induced density change in PAG polymer gel dosimeters: a model and experimental investigations. *Phys. Med. Biol.*, pages 2477–2490, 2004.

[103] K. B. McAuley. Fundamentals of Polymer Gel Dosimeters. *J. Phys. Conf. Ser.*, 56:35–44, 2007.

[104] De Deene, Y. and Baldock, C. Optimization of multiple spin–echo sequences for 3D polymer gel dosimetry. *Phys. Med. Biol.*, 47:3117, 2002.

[105] M. Lepage, A. K. Whittaker, L. Rintoul, S. A. Back, and C. Baldock. The relationship between radiation-induced chemical processes and transverse relaxation times in polymer gel dosimeters. *Phys. Med. Biol.*, 46:1061–1074, 2001.

[106] C. Baldock, R. P. Burford, N. Billingham, G. S. Wagner, S. Patval, R. D. Badawi, and S. F. Keevil. Experimental procedure for the manufacture and calibration of polyacrylamide gel (PAG) for magnetic resonance imaging (MRI) radiation dosimetry. *Phys. Med. Biol.*, 43:695, 1998.

[107] Lepage, M. and McMahon, K. and Galloway, G. J. and De Deene, Y. and Back, S. A. J. and Baldock, C. Magnetization transfer imaging for polymer gel dosimetry. *Phys. Med. Biol.*, 47:1881–1890, 2002.

[108] De Deene, Y. Review of quantitative MRI principles for gel dosimetry. *J. Phys. Conf. Ser.*, 164:012033, 2009.

[109] K. T. S. Islam, J. F. Dempsey, M. K. Ranade, M. J. Maryanski, and D. A. Low. Initial evaluation of commercial optical CT-based 3D gel dosimeter. *Med. Phys.*, 30:2159–2168, 2003.

[110] R. G. Kelly, K. J. Jordan, and J. J. Battista. Optical CT reconstruction of 3D dose distributions using the ferrous-benzoic-xylenol (FBX) gel dosimeter. *Med. Phys.*, 25:1741–1750, 1998.

[111] Xu, Y. and Wuu, C.-S. and Maryanski, M. J. Performance of a commercial optical CT scanner and polymer gel dosimeters for 3-D dose verification. *Med. Phys.*, 31:3024–3033, 2004.

[112] Lopatiuk-Tirpak, O. and Langen, K. M. and Meeks, S. L. and Kupelian, P. A. and Zeidan, O. A. and Maryanski, M. J. Performance evaluation of an improved optical computed tomography polymer gel dosimeter system for 3D dose verification of static and dynamic phantom deliveries. *Med. Phys.*, 35:3847–3859, 2008.

[113] S. J. Doran. The history and principles of optical computed tomography for scanning 3-D radiation dosimeters: 2008 update. *J. Phys. Conf. Ser.*, 164:012020, 2009.

[114] S. J. Doran, K. K. Koerkamp, M. A. Bero, P. Jenneson, E. J. Morton, and W. B. Gilboy. A CCD-based optical CT scanner for high-resolution 3D imaging of radiation dose distributions: equipment specifications, optical simulations and preliminary results. *Phys. Med. Biol.*, 46:3191–3213, 2001.

[115] N. Krstajic and S. J. Doran. Focusing optics of a parallel beam CCD optical tomography apparatus for 3D radiation gel dosimetry. *Phys. Med. Biol.*, 51:2055–2075, 2006.

[116] N. Krstajic and S. J. Doran. Characterization of a parallel-beam CCD optical-CT apparatus for 3D radiation dosimetry. *Phys. Med. Biol.*, 52:3693–3713, 2007.

[117] J. G. Wolodzko, C. Marsden, and A. Appleby. CCD imaging for optical tomography of gel radiation dosimeters. *Med. Phys.*, 26:2508–2513, 1999.

[118] K. Jordan and J. Battista. Small, medium and large optical cone beam CT. *J. Phys. Conf. Ser.*, 56:214–216, 2007.

[119] J. V. Trapp, S. A. J. Back, M. Lepage, G. Michael, and C. Baldock. An experimental study of the dose response of polymer gel dosimeters imaged with x-ray computed tomography. *Phys. Med. Biol.*, 46:2939–2951, 2001.

[120] S. Brindha, A. J. Venning, B. Hill, and C. Baldock. Experimental study of attenuation properties of normoxic polymer gel dosimeters. *Phys. Med. Biol.*, 49:N353–N361, 2004.

[121] J. V. Trapp, G. Michael, Y. Deene, and C. Baldock. Attenuation of diagnostic energy photons by polymer gel dosimeters. *Phys. Med. Biol.*, 47:4247–4258, 2002.

[122] M. Hilts, A. Jirasek, and C. Duzenli. Technical considerations for implementation of x-ray CT polymer gel dosimetry. *Phys. Med. Biol.*, 50:1727–1745, 2005.

[123] M. Hilts and C. Duzenli. Image filtering for improved dose resolution in CT polymer gel dosimetry. *Med. Phys.*, 31:39–49, 2004.

[124] M. Hilts and A. Jirasek. Adaptive mean filtering for noise reduction in CT polymer gel dosimetry. *Med. Phys.*, 35:344–355, 2008.

[125] A. Jirasek, Q. Matthews, M. Hilts, G. Schulze, M. W. Blades, and R. F. B. Turner. Investigation of a 2D two-point maximum entropy regularization method for signal-to-noise ratio enhancement: application to CT polymer gel dosimetry. *Phys. Med. Biol.*, 51:2599–2617, 2006.

[126] A. Jirasek, J. Carrick, and M. Hilts. An x-ray CT polymer gel dosimetry prototype: I. Remnant artefact removal. *Phys. Med. Biol.*, 57:3137–3153, 2012.

[127] V. I. Koeva, T. Olding, A. Jirasek, L. J. Schreiner, and K. B. McAuley. Preliminary investigation of the NMR, optical and x-ray CT dose-response of polymer gel dosimeters incorporating cosolvents to improve dose sensitivity. *Phys. Med. Biol.*, 54:2779–2790, 2009.

[128] A. Jirasek, M. Hilts, A. Berman, and K. B. McAuley. Effects of glycerol co-solvent on the rate and form of polymer gel dose response. *Phys. Med. Biol.*, 54:907–918, 2009.

[129] A. Jirasek, M. Hilts, and K. B. McAuley. Polymer gel dosimeters with enhanced sensitivity for use in x-ray CT polymer gel dosimetry. *Phys. Med. Biol.*, 55:5269–5281, 2010.

[130] H. Johnston, M. Hilts, J. Carrick, and A. Jirasek. An x-ray CT polymer gel dosimetry prototype: II. Gel characterization and clinical application. *Phys. Med. Biol.*, 57:3155–3175, 2012.

[131] De Deene, Y. On the accuracy and precision of gel dosimetry. *J. Phys. Conf. Ser.*, 56:72–85, 2007.

[132] C. Baldock, M. Lepage, S. A. J. Back, P. J. Murry, P. M. Jayasekera, D. Porter, and T. Kron. Dose resolution in radiotherapy polymer gel dosimetry: effect of echo spacing in MRI pulse sequence. *Phys. Med. Biol.*, 46:449–460, 2001.

[133] De Deene, Y. Essential characteristics of polymer gel dosimeters. *J. Phys. Conf. Ser.*, 3:34–57, 2004.

[134] G. S. Ibbott, M. J. Maryanski, P. Eastman, S. D. Holcomb, Y. Zhang, R. G. Avison, M. Sanders, and J. C. Gore. Three-dimensional visualization and measurement of conformal dose distributions using magnetic resonance imaging of BANG polymer gel dosimeters. *Int. J. Radiat. Oncol. Biol. Phys.*, 38:1097–1103, 1997.

[135] De Deene, Y. and De Wagter, C. and Van Duyse, B. and Derycke, S. and De Neve, W. and Achten, E. Three-dimensional dosimetry using polymer gel and magnetic resonance imaging applied to the verification of conformal radiation therapy in head-and-neck cancer. *Radiother. Oncol.*, 48:283–291, 1998.

[136] M. Oldham, I. Baustert, C. Lord, T. A. Smith, M. McJury, A. P. Warrington, M. O. Leach, and S. Webb. An investigation into the dosimetry of a nine-field tomotherapy irradiation using BANG-gel dosimetry. *Phys. Med. Biol.*, 43:1113–1132, 1998.

[137] Low, D. A. and Dempsey, J. F. and Venkatesan, R. and Mutic, S. and Markman, J. and Mark Haacke, E. and Purdy, J. A. Evaluation of polymer gels and MRI as a 3-D dosimeter for intensity-modulated radiation therapy. *Med. Phys.*, 26:1542–1551, 1999.

[138] V. P. Cosgrove, P. S. Murphy, M. McJury, E. J. Adams, A. P. Warrington, M. O. Leach, and S. Webb. The reproducibility of polyacrylamide gel dosimetry applied to stereotactic conformal radiotherapy. *Phys. Med. Biol.*, 45:1195–1210, 2000.

[139] De Deene, Y. and De Wagter, C. and Van Duyse, B. and Derycke, S. and Mersseman, B. and De Gersem, W. and Voet, T. and Achten, E. and De Neve, W. Validation of MR-based polymer gel dosimetry as a preclinical three-dimensional verification tool in conformal radiotherapy. *Magn. Reson. Med.*, 43:116–125, 2000.

[140] Vergote, K. and De Deene, Y. and Claus, F. and De Gersem, W. and Van Duyse, B. and Paelinck, L. and Achten, E. and De Neve, W. and De Wagter, C. Application of monomer/polymer gel dosimetry to study the effects of tissue inhomogeneities on intensity-modulated radiation therapy (IMRT) dose distributions. *Radiother. Oncol.*, 67:119–128, 2003.

[141] P. A. Love, P. M. Evans, M. O. Leach, and S. Webb. Polymer gel measurement of dose homogeneity in the breast: comparing MLC intensity modulation with standard wedged delivery. *Phys. Med. Biol.*, 48:1065–1074, 2003.

[142] P. Sandilos, A. Angelopoulos, P. Baras, K. Dardoufas, P. Karaiskos, P. Kipouros, M. Kozicki, J. M. Rosiak, L. Sakelliou, I. Seimenis, and L. Vlahos. Dose verification in clinical IMRT prostate incidents. *Int. J. Radiation Oncology Biol. Phys.*, 59:1540–1547, 2004.

[143] Duthoy, W. and De Gersem, W. and Vergote, K. and Coghe, M. and Boterberg, T. and De Deene, Y. and De Wagter, C. and Van Belle, S. and De Neve, W. Whole abdominopelvic radiotherapy (WAPRT) using intensity-modulated arc therapy (IMAT): first clinical experience. *Int. J. Radiat. Oncol. Biol. Phys.*, 57:1019–1032, 2003.

[144] Duthoy, W. and De Gersem, W. and Vergote, K. and Boterberg, T. and Derie, C. and Smeets, P. and De Wagter, C. and De Neve, W. Clinical implementation

of intensity-modulated arc therapy (IMAT) for rectal cancer. *Int. J. Radiat. Oncol. Biol. Phys.*, 60:794–806, 2004.

[145] Vergote, K. and De Deene, Y. and Duthoy, W. and De Gersem, W. and De Neve, W. and Achten, E. and De Wagter, C. Validation and application of polymer gel dosimetry for the dose verification of an intensity-modulated arc therapy (IMAT) treatment. *Phys. Med. Biol.*, 49:287–305, 2004.

[146] A. Ertl, A. Berg, M. Zehetmayer, and P. Frigo. High-resolution dose profile studies based on MR imaging with polymer BANG^{TM} gels in stereotactic radiation techniques. *Magn. Reson. Imaging*, 18:343–349, 2000.

[147] G. Grebe, M. Pfaender, M. Roll, L. Luedemann, and R. E. Wurm. Dynamic arc radiosurgery and radiotherapy: commissioning and verification of dose distributions. *Int. J. Radiat. Oncol. Biol. Phys.*, 49:1451–1460, 2001.

[148] Pappas, E. and Seimenis, I. and Angelopoulos, A. and Georgolopoulou, P. and Kamariotaki-Paparigopoulou, M. and Maris, T. and Sakelliou, L. and Sandilos, P. and Vlachos, L. Narrow stereotactic beam profile measurements using N-vinylpyrrolidone based polymer gels and magnetic resonance imaging. *Phys. Med. Biol.*, 46:783–797, 2001.

[149] J. Novotny, P. Dvorak, V. Spevacek, J. Tintera, J. Novotny, T. Cechak, and R. Liscak. Quality control of the stereotactic radiosurgery procedure with the polymer-gel dosimetry. *Radiother. Oncol.*, 63:223–230, 2002.

[150] S. G. Scheib and S. Gianolini. Three-dimensional dose verification using BANG gel: a clinical example. *J. Neurosurg.*, 97:582–587, 2002.

[151] Y. Watanabe, G. M. Perera, and R. B. Mooij. Image distortion in MRI-based polymer gel dosimetry of gamma knife stereotactic radiosurgery systems. *Med. Phys.*, 29:797–802, 2002.

[152] P. Karaiskos, L. Petrokokkinos, E. Tatsis, A. Angelopoulos, P. Baras, M. Kozicki, P. Papagiannis, J. M. Rosiak, L. Sakelliou, P. Sandilos, and L. Vlachos. Dose verification of single shot gamma knife applications using VIPAR polymer gel and MRI. *Phys. Med. Biol.*, 50:1235–1250, 2005.

[153] P. Papagiannis, P. Karaiskos, M. Kozicki, J. M. Rosiak, L. Sakelliou, P. Sandilos, I. Seimenis, and M. Torrens. Three-dimensional dose verification of the clinical application of gamma knife stereotactic radiosurgery using polymer gel and MRI. *Phys. Med. Biol.*, 50:1979–1990, 2005.

[154] A. R. Farajollahi, D. E. Bonnett, A. J. Ratcliffe, R. J. Aukett, and J. A. Mills. An investigation into the use of polymer gel dosimetry in low dose rate brachytherapy. *Br. J. Radiol.*, 72:1085–1092, 1999.

[155] Wuu, C.-S. and Schiff, P. and Maryanski, M. J. and Liu, T. and Borzillary, S. and Weinberger, J. Dosimetry study of Re-188 liquid balloon for intravascular brachytherapy using polymer gel dosimeters and laser-beam optical CT scanner. *Med. Phys.*, 30:132–137, 2003.

[156] H. Gustavsson, A. Karlsson, S. A. J. Back, L. E. Olsson, P. Haraldsson, P. Engstrom, and H. Nystrom. MAGIC-type polymer gel for three-dimensional dosimetry: intensity-modulated radiation therapy verification. *Med. Phys.*, 30:1264–1271, 2003.

[157] F. Nordstrom, S. Ceberg, S. Wetterstedt, P. Nilsson, C. Ceberg, and S. A. J. Back. 3D geometric gel dosimetry verification of intraprostatic fiducial guided hypofractionated radiotherapy of prostate cancer. *J. Phys. Conf. Ser.*, 250:012059, 2010.

[158] Ceberg, S. and Gagne, I. and Gustafsson, H. and Scherman, J. B. and Korreman, S. S. and Kjaer-Kristoffersen, F. and Hilts, M. and Back, S. A. J. RapidArc treatment verification in 3D using polymer gel dosimetry and Monte Carlo simulation. *Phys. Med. Biol.*, 55:4885–4898, 2010.

[159] Vandecasteele, J. and De Deene, Y. On the validity of 3D polymer gel dosimetry: III. MRI-related error sources. *Phys. Med. Biol.*, 58:63–85, 2012.

[160] C. H. Yao, W. T. Hsu, S. M. Hsu, P. Y. L. Ma, B. T. Hsieh, and Y. J. Chang. NIPAM polymer gel dosimetry for IMRT four-field box irradiation using optical-CT scanner. *J. Phys. Conf. Ser.*, 444:012030, 2013.

[161] T Olding, O Holmes, P. DeJean, K. B. McAuley, K. Nkongchu, G. Santyr, , and L. J. Schreiner. Small field dose delivery evaluations using cone beam optical

computed tomography-based polymer gel dosimetry. *J. Med. Phys.*, 36:3–14, 2011.

[162] C. Audet, M. Hilts, A. Jirasek, and C. Duzenli. CT gel dosimetry technique: comparison of a planned and measured 3D stereotactic dose volume. *J. Appl. Clin. Med. Phys.*, 3:110–118, 2002.

[163] B. Hill, A. J. Venning, and C. Baldock. A preliminary study of the novel application of normoxic polymer gel dosimeters for the measurement of CTDI on diagnostic x-ray CT scanners. *Med. Phys.*, 32:1589–1597, 2005.

[164] M. Hilts, J. Carrick, H. Johnston, and A. Jirasek. A CT Polymer Gel Dosimetry System for End-To-End Dosimetry. *Med. Phys.*, 38(6):3507–3507, 2011.

[165] M. Hilts, H. Johnston, J. Carrick, and A. Jirasek. Gel dosimetry for the clinic: a new system utilizing CT readout. *Radiother. Oncol.*, 103(S1):S86–S87, 2012.

[166] Kramme, R. and Hoffmann, K.-P. and Pozos, R. S. *Springer Handbook of Medical Technology*. Springer, Berlin, 4th edition, 2011.

[167] P. Baxter, A. Jirasek, and M. Hilts. X-ray CT dose in normoxic polyacrylamide gel dosimetry. *Med. Phys.*, 34:1934–1943, 2007.

[168] V. I. Koeva, E. S. Csaszar, R. J. Senden, K. B. McAuley, and L. J. Schreiner. Polymer Gel Dosimeters with Increased Solubility: A Preliminary Investigation of the NMR and Optical Dose-Response Using Different Crosslinkers and Co-Solvents. *Macromol. Symp.*, 261:157–166, 2008.

[169] T. Gorjiara, R. Hill, S. Bosi, Z. Kuncic, and C. Baldock. Water equivalence of NIPAM based polymer gel dosimeters with enhanced sensitivity for x-ray CT. *Radiat. Phys. Chem.*, pages 1–10, 2013.

[170] M. Hilts, C. Jirasek, A. Audet, and C. Duzenli. X-ray CT polymer gel dosimetry: applications to stereotactic radiosurgery and proton therapy. *Radiother. Oncol.*, 56:S80, 2000.

[171] Ghavami, S.-M. and Mesbahi, A. and Pesianian, I. and Shafaee, A. and Aliparasti, M.-R. Normoxic polymer gel dosimetry using less toxic monomer of N-isopropyl acrylamide and X-ray computed tomography for radiation therapy applications. *Rep. Pract. Oncol. Radiother.*, 15(6):172–175, 2010.

[172] D. Low, W. B. Harms, S. Mutic, and J. A. Purdy. A technique for the quantitative evaluation of dose distributions. *Med. Phys.*, pages 1–6, 1998.

[173] De Deene, Y. and Vergote, K. and Claeys, C. and De Wagter, C. The fundamental radiation properties of normoxic polymer gel dosimeters: a comparison between a methacrylic acid based gel and acrylamide based gels. *Phys. Med. Biol.*, 51:653–673, 2006.

[174] M. Lepage, A. K. Whittaker, L. Rintoul, S. A. J. Back, and C. Baldock. Modelling of post-irradiation events in polymer gel dosimeters. *Phys. Med. Biol.*, pages 1–14, 2001.

[175] A. J. Venning, B. Hill, S. Brindha, B. J. Healy, and C. Baldock. Investigation of the PAGAT polymer gel dosimeter using magnetic resonance imaging. *Phys. Med. Biol.*, 50:3875–3888, 2005.

[176] A. Jirasek, M. Hilts, C. Shaw, and P. Baxter. Investigation of tetrakis hydroxymethyl phosphonium chloride as an antioxidant for use in x-ray computed tomography polyacrylamide gel dosimetry. *Phys. Med. Biol.*, 51:1891–1906, 2006.

[177] B. T. Hsieh, Y. J. Chang, R. P. Han, J. Wu, L. L. Hsieh, and C. J. Chang. A study on dose response of NIPAM-based dosimeter used in radiotherapy. *J. Radioanal. Nucl. Chem.*, 290:141–148, 2011.

[178] Chang, K.-Y. and Shih, T.-Y. and Hsieh, B.-T. and Chang, S.-J. and Liu, Y.-L. and Wu, T.-H. and Wu, J. Investigation of the dose characteristics of an n-NIPAM gel dosimeter with computed tomography. *Nucl. Instrum. Methods Phys. Res., Sect. A*, 652:775–778, 2011.

[179] Chang, Y.-J. and Hsieh, B.-T. and Liang, J.-A. A systematic approach to determine optimal composition of gel used in radiation therapy. *Nucl. Instrum. Methods Phys. Res., Sect. A*, 652:783–785, 2011.

[180] Gelfi, C. and Righetti, P.G. Polymerization kinetics of polyacrylamide gels I. Effects of different crosslinkers. *Electrophoresis*, 2:213–219, 1981.

[181] Vergote, K. and De Deene, Y. and Vanden Bussche, E. and De Wagter, C. On the relation between the spatial dose integrity and the temporal instability of polymer gel dosimeters. *Phys. Med. Biol.*, 49:4507–4522, 2004.

[182] C. Hurley, A. Venning, and C. Baldock. A study of a normoxic polymer gel dosimeter comprising methacrylic acid, gelatin and tetrakis (hydroxymethyl) phosphonium chloride (MAGAT). *Appl. Radiat. Isot.*, 63:443–456, 2005.

[183] De Deene, Y. and Reynaert, N. and De Wagter, C. On the accuracy of monomer/polymer gel dosimetry in the proximity of a high-dose-rate 192Ir source. *Phys. Med. Biol.*, 46:2801–2825, 2001.

[184] A. Karlsson, H. Gustavsson, S. Maansson, K. B. McAuley, and S. A. J. Back. Dose integration characteristics in normoxic polymer gel dosimetry investigated using sequential beam irradiation. *Phys. Med. Biol.*, 52:4697–4706, 2007.

[185] J. Gao and B. J. Frisken. Cross-Linker-Free N-Isopropylacrylamide Gel Nanospheres. *Langmuir*, 19:5212–5216, 2003.

[186] X. Hu, Z. Tong, and L. A. Lyon. Control of Poly(N-isopropylacrylamide) Microgel Network Structure by Precipitation Polymerization near the Lower Critical Solution Temperature. *Langmuir*, 27:4142–4148, 2011.

[187] Mutic, S. and Palta, J. R. and Butker, E. K. and Das, I. J. and Huq, M. S. and Loo, L.-N. D. and Salter, B. J. and McCollough, C. H. and Van Dyk, J. Quality assurance for computed-tomography simulators and the computed-tomography-simulation process: Report of the AAPM Radiation Therapy Committee Task Group No. 66. *Med. Phys.*, 30:2762–2792, 2003.

[188] M. Endo, T. Tsunoo, N. Nakamori, and K. Yoshida. Effect of scattered radiation on image noise in cone beam CT. *Med. Phys.*, 28:469–474, 2001.

[189] S. Xing, Y. Guan, and Y. Zhang. Kinetics of Glucose-Induced Swelling of P(NIPAM-AAPBA) Microgels. *Macromolecules*, 44(11):4479–4486, 2011.

[190] Z. Wu and Z. Zhong. A theoretical model for thermal-sensitive microgel with pNIPAM core and elastic shell. *Acta. Mechanica Solida Sinica*, 25(5):520–529, 2012.